HABILITATION À DIRIGER DES RECHERCHES

Spécialité : Mécanique des fluides

Dynamique des fluides, instabilités, turbulence et fluides complexes

Fluid Dynamics, Instabilities, Turbulence and Complex Fluids

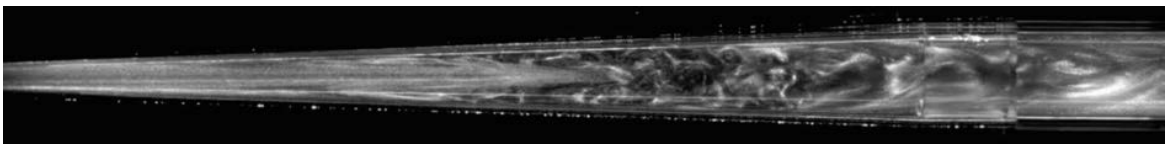

Présentée par

Jorge Peixinho
Chargé de Recherche à l'Unité Mixte de Recherche (UMR)
Laboratoire Ondes et Milieux Complexes (LOMC), CNRS et Université du Havre

Soutenue le 8 juillet 2015 devant un jury composé de :

Rapporteurs	Patrice Le Gal	Directeur de recherche CNRS, Marseille
	François Lusseyran	Directeur de recherche CNRS, Orsay
	Chérif Nouar	Directeur de recherche CNRS, Nancy
Président	Tom Mullin	Professor, University of Manchester
Examinateur	Innocent Mutabazi	Professeur, Université du Havre

Remerciements

Je remercie très chaleureusement les membres du jury qui ont accepté d'évaluer ce manuscrit malgré leurs emplois du temps chargés. Ma reconnaissance va aux rapporteurs : Chérif Nouar déjà présent depuis le début de ma thèse, François Lusseyran que j'ai retrouvé tout au long de mon parcours et Patrice Le Gal qui s'est toujours montré très enthousiaste lorsqu'il s'agissait de discuter de résultats d'expériences. Enfin, cette habilitation m'a également donné l'occasion d'approfondir nos liens transmanche avec l'université de Manchester représentée par Tom Mullin.

Merci à Innocent Mutabazi qui est le directeur du laboratoire (LOMC UMR CNRS 6294 et Université du Havre) et de l'équipe Instabilités Transition à la Turbulence (ITT). Je tiens à le remercier pour sa confiance et les encouragements généreusement prodigués depuis quatre ans. Innocent a encouragé mon recrutement comme chercheur CNRS au sein du LOMC et de l'Université du Havre. Je lui suis en particulier très reconnaissant pour son appui constant afin de développer l'activité *pipe flow* du laboratoire. Nous avons encadré la thèse de Borja Martínez-Arias sur la turbulence dans un écoulement de Taylor-Couette. J'ai énormément appris grâce à son expérience et beaucoup apprécié notre collaboration.

Un travail de recherche est avant tout un travail d'équipe. Ce manuscrit résume ainsi les efforts des jeunes membres de l'équipe que je tiens à remercier. En particulier, les très jeunes chercheurs sont bien souvent conduits à une impasse, leur travail d'exploration est néanmoins capital. Voici au moins leurs noms : Hélène Penissi, Angela Furrer, Kentaro Okamoto, Kenji Hasguchi, Coralie Carmouze, John Coulet, Lukas Schimmer, Abou Ba, Susan Tan, Khac Lan Nguyen, Matheus Peixoto de Oliveira, Norio Yonezawa, Jumpei Ohkudo, Natacha Macé et Juliette Lemaître.

Toute recherche est le résultat de discussions avec des collègues sur des idées. Il y a aussi le partage d'astuces expérimentales ou d'équipements. Présenter une liste exhaustive de toutes ces contributions serait impossible, car il faudrait mentionner tout le laboratoire ainsi que de nombreux collègues de l'Université du Havre et de bien d'autres institutions. Quelques noms sont incontournables : Arnaud Prigent, Olivier Crumeyrolle, Gaële Perret, Benoît Duchemin et Hugues Besnard. De nombreux visiteurs ont également apporté leurs contributions à notre laboratoire. J'ai enfin eu la chance de pouvoir visiter plusieurs groupes à travers le monde : le LAS (*Lehrstuhl für Aerodynamik und Strömungslehre*) chez Christoph Egbers à Cottbus, le groupe de Jeffrey Morris au *Levich Institute* à New York et le groupe de Takahiro Tsukahara à la *Tokyo University of Science*.

On l'oublie souvent, mais un laboratoire n'est pas seulement un groupe de chercheurs

perdus dans leurs pensées ou leurs expériences. L'épine dorsale du laboratoire est son personnel administratif et technique. Je suis toujours impressionné par l'efficacité de Carole Le Guen et Faroudja Hadjaj, secrétaires du laboratoire. Nous ne pourrions rien construire sans nos techniciens qui ont réalisé la plupart des montages expérimentaux que nous utilisons. On l'oublie encore plus souvent, mais si nos bureaux, laboratoires et ateliers sont propre le matin quand nous arrivons, c'est que quelques fées sont passées par là. La nôtre s'appelle Valérie Le Bris.

Enfin, je remercie mon épouse Audrey qui m'aide tous les jours à voir un peu plus loin que le bout de mon nez.

Contents

Chapter 1

Introduction

My first research experience was an internship during my *License de Mécanique* at the *Université Henri Poincaré* in Nancy at the LEMTA (*Laboratoire d'Energétique et de Mécanique Théorique et Appliquée*) with Christophe Baravian and Michel Gradeck. The subject dealt with a simple experiment about the hydraulic jump, where we had to measure the liquid films before and after the jump and compare with the theory of an old paper (1964) by Watson published in Journal of Fluid Mechanics. One year later, I did again an internship with the same people and the simple experiment turned into an much complicated experiment about a cold jet impacting on a hot plate. The experiment now consisted in measuring the velocity and the temperature fields using high speed cameras and highly complicated technical equipments. It also involved an industrial partner *Arcelor*, a steel producer, highly regarded in the region. One year later, I had the chance to make yet another internship in the same laboratory but with Chérif Nouar and Michel Lebouché on the flow of yield stress fluids in a pipe. This project was granted by *Schlumberger*, a oilfield services company and involved many aspect of my futur research career because it dealt with rheology, both laminar and turbulent pipe flow, pressure, velocity and heat transfer measurements. The internship went well, the engineers from the company (Jean Romero, Ian Frigaard and Gérard Daccord) offered to continue as a CIFRE (*Convention Industrielle de Formation par la Recherche*) as the pipe experiment was built during my master internship. During the *thèse de doctorat*, I had the chance to study experimentally the transition to turbulence for yield stress fluids, shear-thinning fluids and Newtonian fluids. The fluids properties was tested using rotational rheology and the flow was monitored using pressure measurement and laser Doppler velocimetry. By testing different fluids, we were able to quantify the velocity fluctuations during the transition to turbulence. In a second part of the *thèse de doctorat*, a annular pipe was mounted on the setup. Finally, heat transfer measurements were performed in circular and annular pipe flow, specifically with constant heat flux at the walls.

After the *thèse de doctorat*, the transition to turbulence was further studied in the context of nonlinear dynamics at the Manchester Centre for Nonlinear Dynamics of the Physics and Astronomy Department of the University of Manchester under the mentoring of Tom Mullin. At that time, travelling waves solutions of circular Poiseuille flow were

just discovered and a long pipe was up on running to measure some of its properties, specifically their lifetime and the critical finite amplitude perturbations that could sustain the puff. During the course of my stay in Manchester, I got interested in nonlinear dynamics and granular flow. The natural combination of pipe flow and multiphase flow was the study of bubbly flow in a pipe that I studied at the University of Tokyo (Japan) as Postdoctoral Research Fellow at the Fluid Engineering Laboratory of the Mechanical Engineering Department of the University of Tokyo under the supervision of Yoichiro Matsumoto. More complex fluids were studied during a stay at the City University of the City College of New York (United States of America) as Postdoctoral Research Associate at the Benjamin Levich Institute for Physico-Chemical Hydrodynamics and Chemical Engineering Department of the City College of New York under the supervision of Jeff Morris. The complex fluids were emulsions of water drops in oil that solidify when exposed to temperature gradients. This research, granted by *Chevron*, again dealt with rheology, laminar flow, interface flow and heat transfer.

After that, I returned to France in 2010, as a *chercheur contractuel* for CNRS at Chimie-ParisTech, under the supervision of Grégory Lefèvre and François-Xavier Coudert to investigate heat transfer of particulate deposits both through experiments and lattice models. Since 2011, I became a CNRS *chargé de recherche* at LOMC. My first topic is transition to turbulence in pipe flow. Specifically, the understanding of the condition and location of turbulence in diverging pipe flow, both through experiments and numerical approaches. In addition, the group headed by Innocent Mutabazi has several investigations on Taylor-Couette flow both considering viscoelastic fluids and heat transfer.

In the manuscript, I present a selection of research conducted in the past years and specifically since my arrival in Le Havre. I will not describe my work from the *thèse de doctorat* but mostly the late developments of our research. In each chapter, I will try to introduce the background and the main questions that should be answered. Also each chapter ends with a number of perspectives of the future research that I think are important and hope to undertake. Chapter 2 deals with the stability of pipe flow. Some results of uniform (constant diameter) pipe flow transition are recalled. A comparison with pipe flow in a slowly diverging pipe is presented. The dynamics of the recirculation cells and the conditions for onset of disordered motion are described. Chapter 3 reports a series of problems of fluid flow in Taylor-Couette geometry. First, the torque measurements for multiple states are presented and discussed. Results on the flow with viscoelastic fluids and the flow with heat transfer are presented. This geometry is simple, yet many interesting phenomena can be observed. The use of polymer solutions as fluid in our fluid experiments gave us the opportunity to study complex materials. Chapter 4 presents a study on the swelling and the drying of spherical gel. These hydrophilic super-absorbant polymers can exhibit mechanical instabilities. The large swelling implies nonlinear poroelastic models that need quantitative experiments to be validated.

The research presented here were conducted at LOMC and supported financially by the CNRS, the *Université du Havre*, the ANR (*Agence Nationale de la Recherche*) through the programme "*Investissement d'Avenir*" LabEx EMC^3 (Energy Materials and Clean Combustion Center) and the *région Haute-Normandie*.

Chapter 2

Pipe flow

The origin of turbulence in the flow along a pipe of circular cross-section has been the subject of many scientific investigations since the work of Hagen[1,2], Poiseuille[3], Darcy[4] and Reynolds[5] (see their portraits in figure 2.1). Following Reynolds[5], Ekman[6], Comolet[7], Rotta[8], Lindgren[9], Wygnanski[10] and many others[11] carried out extensive experimental investigations and produced many interesting results about the transition in pipes. Most of the early investigations were practical and dealt with the pressure drop. Reynolds made a major breakthrough with his elegant visual experiment that attracted a lot of interest. It is only in the end of the twentieth century that quantitative experiments were able to measure intermittency of puffs (patches of turbulence), finite amplitude stability curves, puff propagation speeds, puffs lengths, lifetimes, and velocities within puffs, etc. These new

[1]Hagen G. Über die bewegung des wassers in engen cylindrischen röhren. *Ann. Phys. Chem.* 46:423-42 (1839).

[2]Hagen G. On the influence of temperature on the movement of water through pipes. *Abh. Akad. Wiss.* 6:17-98 (1854)

[3]Poiseuille JLM. Recherches expérimentales sur le mouvement des liquides dans les tubes de très petit diamètres. *C. R. Acad. Sci.* 11:961–67 (1840)

[4]Darcy HPG. Recherches expérimentales relatives au mouvement de l'eau dans les Tuyaux. *Paris: Mallet-Bachelier* (1857)

[5]Reynolds O. An experimental investigation of the circumstances which determine whether the motion of water shall be direct or sinuous and of the law of resistance in parallel channels. *Philos. Trans. R. Soc. Lond. Ser. A* 174:935–82 (1883)

[6]Ekman VW. On the change from steady to turbulent motion of liquids. *Ark. Mat. Astron. Fys.* 6(12):1–16 (1911)

[7]Comolet R. Recherches sur la genèse de la turbulence dans les conduites en charge. *Magasin C. T. O., Paris* (1950)

[8]Rotta J. Experimenteller beitrag zur entstehung turbulenter strömung im rohr. *Ing. Arch.* 24:258–82 (1956)

[9]Lindgren ER. The transition process and other phenomena in viscous flow. *Ark. Fys.* 12:1–169 (1957)

[10]Wygnanski IJ and Champagne FH. On transition in a pipe. Part 1. The origin of puffs and slugs and the flow in a turbulent slug. *J. Fluid Mech.* 59:281–351 (1973)

[11]Mullin T. Experimental studies of transition to turbulence in a pipe. *Annu. Rev. Fluid Mech.* 43:1-24 (2011)

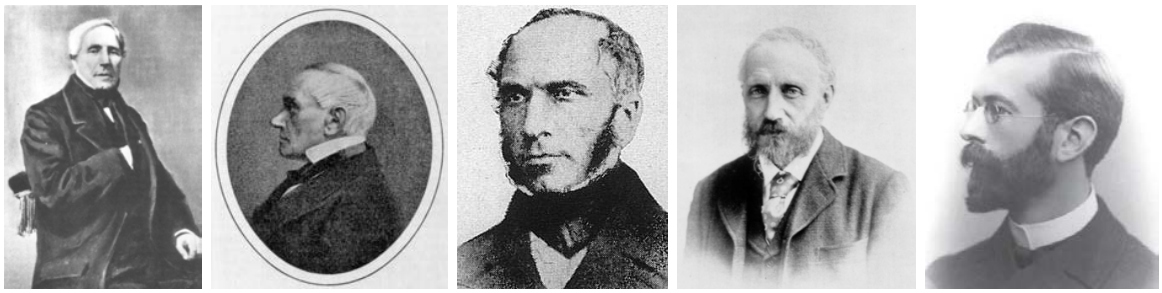

Figure 2.1: From left to right: Jean Léonard Marie Poiseuille (1797-1869), Gotthilf Heinrich Ludwig Hagen (1797-1884), Henry Philibert Gaspard Darcy (1803-1858), Osborne Reynolds (1842-1912) and Vagn Walfrid Ekman (1874-1954)

data stimulated theoretical and numerical simulations that again lead to new measurements. Furthermore, the discovery of nonlinear solutions of the Navier-Stokes equations, the travelling wave solutions by Faisst and Eckhardt[12], Wedin and Kerswell[13] and Hof, van Doorme *et al.*[14], allowed to explain the fluid motion patterns in turbulent puffs and made a connection between theoretical/numerical studies and quantitative experiments. Some of theses results are recalled and their significance to transition to turbulence in pipe flow and in gradual expansion pipe flow is discussed.

Publications associated with this chapter

- Jorge Peixinho and Tom Mulllin. Decay of turbulence in pipe flow. *Phys. Rev. Lett.* 96:094501 (2006)
- Jorge Peixinho and Hugues Besnard. Transition to turbulence in slowly divergent pipe flow. Phys. Fluids 25:111702 (2013)
- Kamal Selvam, Jorge Peixinho and Ashley P. Willis. Localised turbulence in a circular pipe flow with gradual expansion. *J. Fluid Mech.* 771:R2 (2015)

2.1 Review of previous works

Hagen[2] and Poiseuille[3] both observed that the relation between the flow rate and the pressure gradient is linear when the velocity is relatively small, that is when the flow is

[12]Faisst H and Eckhardt B. Travelling waves in pipe flow. *Phys. Rev. Lett.* 91:224502 (2003)

[13]Wedin H and Kerswell RR. Exact coherent structures in pipe flow: travelling wave solutions. *J. Fluid Mech.* 508:333–71 (2004)

[14]Hof B, van Doorne CWH, Westerweel J, Nieuwstadt FTM, Faisst H, Eckhardt B, Wedin H, Kerswell RR, Waleffe F. Experimental observation of nonlinear travelling waves in turbulent pipe flow. *Science* 305:1594–97 (2004)

laminar. It is now called the Hagen-Poiseuille law and may be written as:

$$Q = \frac{\pi \Delta p R^4}{8 \mu L} \tag{2.1}$$

where Q is the volume flux, Δp is the pressure between to points distant by L, R is the pipe radius and μ is the fluid dynamic viscosity.

Introducing the Reynolds number: $Re = UD/\nu$ (where U is the bulk flow velocity, $D = 2R$ the diameter and ν the kinematic viscosity), the friction factor $f = 2\tau_w/\rho U^2$ (where ρ is the density) and the wall shear stress $\tau_w = R\Delta p/2L$, the Hagen-Poiseuille law becomes: $f = 16/Re$. An example of pressure measurements over a range of flow rate is given in figure 2.2(a). The exact verification of the Hagen-Poiseuille law requires a experimental protocol where the pressure drop measurement are made in fully developed flow[15]. During the transition, the flow exhibits large variations due to the appearance of large scale structures, see figure 2.2(b). Yet pressure drop measurements are sometimes used to detect the transition from the Hagen-Poiseuille law (2.1) to the Blasius law: $f = 0.3164 Re^{-1/4}$ that predict the friction for fully developed turbulent pipe flow up to $Re \leq 100\,000$. This friction diagrams, also measured in various pipes by Nikuradse[16], are of an important practical information[17].

Velocity profiles can be measured using ultrasound anemometers, hot film anemometers or laser Doppler velocimeters[18,19,20] in pipe sections far from the inlet. Examples of velocity profiles are presented in figure 2.3. The mean velocity profiles obtained in laminar flows are in very good agreement with the well known parabolic velocity distribution:

$$\frac{u(r)}{U} = 2\left[1 - \left(\frac{r}{R}\right)^2\right] \tag{2.2}$$

where u is the mean axial velocity. The mean velocity profile in turbulent flow obtained at $Re = 5300$ is also in good agreement with previous measurements[21]. The large increase of the wall shear stress between the two profiles explains the large change in pressure drop (or friction).

---

[15]Durst F, Ray S, Ünsal B, Bayoumi OA. The development lengths of laminar pipe and channel flows. *J. Fluids Eng.* 127:1154 (2005)

[16]Nikuradse J. Strömungsgesetze in rauhen rohren. *Forsch. Ing. Arch.* 361 (1933)

[17]Rennels DC and Hudson HM. Pipe flow - A practical and comprehensive guide. *John Wiley & Sons, Inc.* (2012)

[18]Peixinho J. Contribution expérimentale à l'étude de la convection thermique en régime laminaire, transitoire et turbulent pour un fluide à seuil en écoulement dans une conduite. *Thèse de doctorat, Université Henri Poincaré* (2004)

[19]Peixinho J, Nouar C, Desaubry, Théron B. Laminar transitional and turbulent flow of yield stress fluid in pipe flow. *J. Non-Newton. Fluid Mech.* 128:172-184 (2005)

[20]Mullin T and Peixinho J. Transition to turbulence in pipe flow. *J. Low Temp. Phys.* 145:75-88 (2006)

[21]Eggels JGM, Unger F, Weiss MH, Westerweel J, Adrian RJ, Friedrich R, Nieuwstadt FTM. Fully developed turbulent pipe flow: a comparaison between direct numerical simulation and experiment, *J. Fluid Mech.* 268:175-209 (1994)

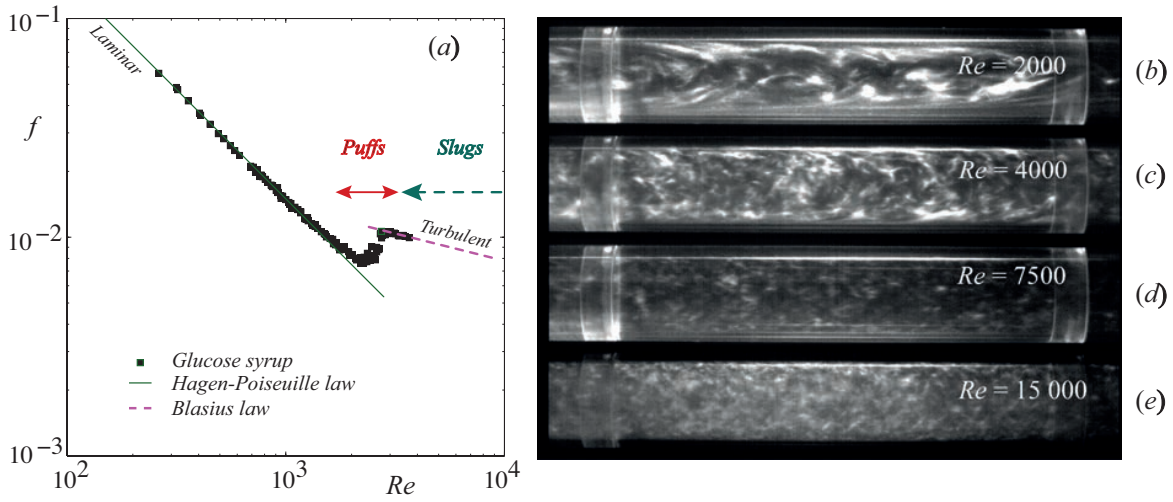

Figure 2.2: (*a*) Friction factor diagram, f versus Re, for a glucose syrup solution (newtonian fluid). The region of transition between the two laws is the region where puffs are found in the Re range from ~ 1760 to ~ 3000. (*b*-*e*) Flow visualisations of various turbulent states at Re from 2000 to 15 000 that highlight the large-scale structures in the disordered flow in this range of Re. Flow is from left to right and the fluid, water with a small amount of Mearlmaid®, is illuminated from top by a vertical light sheet.

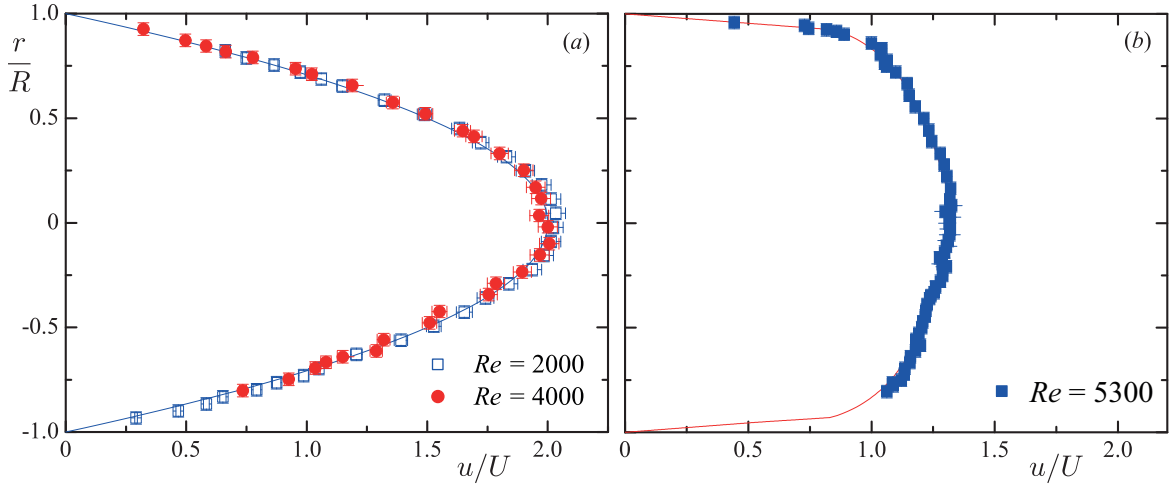

Figure 2.3: (*a*) Velocity profiles measured in laminar flows at $Re = 2000$ and 4000. The solid line corresponds a parabolic profile. (*b*) A mean axial velocity profile measured in turbulent flow at $Re = 5300$ (the red lines correspond to a linear and log fit). Reproduced from Mullin and Peixinho[19].

The stability of the Hagen-Poiseuille flow (HPF) can be investigated by adding infinitesimal perturbations or finite amplitude perturbation to the HPF. The results of all numerical and theoretical investigations into the stability of fully developed HPF suggest[22] that the fully developed flow is linearly stable to infinitesimal perturbations. Indeed, many experimental apparatuses were able to sustain laminar flow at large Re. These well prepared experiments can achieve large Reynolds number flow keeping their velocity profiles laminar[5,23,10]. Then, adding disturbances at the inlet or the fully developed flow in order to initiate transition will indicate the type and the amplitude of the disturbance that control the development of perturbations. Using an impulsive perturbation, several studies mapped out the finite amplitude stability curve. Experimentalists used the injection and/or subtraction of fluid through slits or holes[24,10,25,26,27,28,29] or a retractable iris[30]. Some investigations investigated periodic forcing[26,31,27], but the effect of the periodic forcing on the flow is expected to be complicated.

The forcing eventually leads to patches of disordered fluid motion (puffs) that have a constant length and are though as pulse solutions in the context of nonlinear dynamical system theory where $d\boldsymbol{v}/dt = f(\boldsymbol{v}, Re)$ represents the Navier-Stokes equations:

$$\nabla \cdot \boldsymbol{v} = 0 \tag{2.3}$$

$$\frac{\partial \boldsymbol{v}}{\partial t} + \boldsymbol{v} \cdot \nabla \boldsymbol{v} = -\nabla P + \frac{1}{Re}\nabla^2 \boldsymbol{v}, \tag{2.4}$$

where $\boldsymbol{v} = (u, v, w)$ and P denote the scaled velocity vector and pressure respectively. The system should be solved with the appropriate forcing and boundary conditions[32]. The main parameter of the problem is Re, which determines the state of the system, so

[22]Kerswell RR. Recent progress in understanding the transition to turbulence in a pipe. *Nonlinearity* 18:17–44 (2005)

[23]Pfenniger W. Transition in the inlet length of tubes at high Reynolds numbers. In *Boundary Layer and Flow Control* (ed. G. V. Lachman) 970-980 (1961)

[24]Fox JA, Lessen M and Bhat WV, Experimental investigation of the stability of Hagen-Poiseuille flow. *Phys. Fluids* 11:1 (1968)

[25]Darbyshire AG and Mullin T. Transition to turbulence in constant-mass-flux pipe flow. *J. Fluid Mech.* 289:83–114 (1995)

[26]Draad AA, Kuiken GDC and Nieuwstadt FTM. Laminar–turbulent transition in pipe flow for Newtonian and non-Newton. fluids. *J. Fluid Mech.* 377:267–312 (1998)

[27]Han G, Tumin A and Wygnanski IJ. Laminar–turbulent transition in Poiseuille pipe flow subjected to periodic perturbation emanating from the wall. *J. Fluid Mech.* 419:1–27 (2000)

[28]Hof B, Juel A and Mullin T. Scaling of the turbulence transition threshold in a pipe. *Phys. Rev. Lett.* 91:244502 (2003)

[29]Peixinho J and Mullin T. Finite-amplitude thresholds for transition in pipe flow. *J. Fluid Mech.* 582:169-178 (2007)

[30]Nishi M, Unsal B, Durst F and Biswas G. Laminar-to-turbulent transition of pipe flows through puffs and slugs. *J. Fluid Mech.* 614:425-46 (2008)

[31]Eliahou S, Tumin A, Wygnanski I. Laminar-turbulent transition in Poiseuille pipe flow subjected to periodic perturbation emanating from the wall. *J. Fluid Mech.* 361:333–49 (1998)

[32]Eckhardt B, Schneider, TM, Hof B and Westerweel J. Turbulence transition in pipe flow. *Annu. Rev. Fluid Mech.* 43:1-24 (2007)

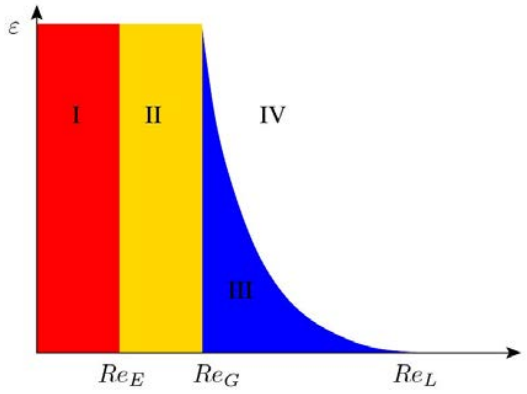

Figure 2.4: Sketch illustrating stability limits of basic flows. The average kinetic energy of a disturbance as a function the Reynolds numbers. Region I: monotonic stability; region II global stability, but not monotonic stability; between Re_G and Re_L: conditional stability; above Re_L: possible instability. Redrawn from Joseph[32].

that there is one linearly stable fixed point, the Hagen-Poiseuille flow (2.2), for all Re and another locally attracting state turbulence when $Re > Re_c$.

More precisely, it is possible to define several critical Reynolds numbers depending on the evolution of different type of perturbations. Joseph[33] introduced the average kinetic energy of a disturbance:

$$\mathcal{E}(t) = \frac{1}{2}\int_V u_i u_i dV \tag{2.5}$$

where u_i are the perturbation velocity components contained in a volume V. Figure 2.4 gives a schematic view of the different Reynolds number regimes depending on $\mathcal{E}$. In region I, that is, for $Re < Re_E$, all disturbances exhibit monotonic decay according to the evolution equation of the energy of disturbace. Region II is characterised by global, but not necessarily monotonic stability. In this region, disturbances may grow, but they will ultimately decay as time evolves. For $Re > Re_G$, we can encounter instabilities according to a perturbation evolution equation (*e.g.* the Reynolds-Orr equation). For Re between Re_G and Re_L we have a conditionally stable flow: for energies below the curve separating regions III and IV the disturbance will decay; for energies above this curve we observe instabilities. The intersection of this curve with the Re-axis defines the Reynolds number above which there exist instabilities of infinitesimal disturbances.

Joseph and Carmi[34,33] found that a disturbance of *any* amplitude added to the HPF would exponentially decay provided that $Re < 81.49$. Experiments[33] indicate that large amplitude disturbance in the form an injection through a single hole change from fast

[33]Joseph DD. Stability of fluid motions I. *Springer-Verlag* (1976)

[34]Joseph DD and Carmi S. Stability of Poiseuille flow in pipes, annuli and channels. *Quart. App. Math.* 26:575–599 (1969)

decay to slow decay for $Re \approx 200$[35,9].

A question which may be asked is, if $\mathcal{A}(Re)$ denotes the minimal amplitude of a finite perturbations that can trigger transition, and if $\mathcal{A}$ scales with Re according to:

$$\mathcal{A} \propto Re^{\gamma} \tag{2.6}$$

when $Re \to \infty$, then what is the exponent γ? This can be stated[36] as the minimal amplitude of all finite perturbations that can trigger transition.

Clearly, the type and injected mass-flux of the perturbation is an important parameter to define the perturbation amplitude. Assuming a single boxcar pulse of fluid, previous works[28,20] have found that the threshold amplitude curve for development of turbulence can be lowered over the range $2000 < Re < 10\ 000$ provided the perturbation is applied for long enough. An series of photographs of the evolution of a single jet injection for small and large amplitude is show in figure 2.5. As the holes diameter are large, the injected fluid is quickly disturbed and if the energy of the perturbation or the Re is large enough, the disordered fluid motion developes a self-sustained puff and travels downstream. Note that the disordered motion after the injection can have similar aspects but will not results in self-sustained long-lived turbulent patch. It seems that the disordered motion contains wavy patterns with wavelengths smaller than the pipe diameter. When the disordered motion decays, longer wavelengths seem to emerge prior to relaminarisation. The threshold for the critical amplitude scales as $1/Re$ for jets[28,29].

Using smaller holes, Peixinho and Mullin[29] and Tasaka *et al.*[37] found that the critical flux of the perturbation, Φ_{inj}, for sustained turbulence can be reduced as showed in figure 2.6(a) and there is a scaling that combines the diameter of the jet, the velocity of the jet, through the jet Reynolds number, $Re_{jet} = 4\Phi_{inj}/\nu\pi d$, and the ratio between the jet diameter, d, and the pipe diameter, D (see figure 2.6(b)). This type of scaling seems to be consistent with cross flow studies. More importantly, hairpin vortices are observed to develop before the onset of turbulence[29,37]. These were associated with a scaling of the critical amplitude, $A = \Phi_{inj}/\Phi_{pipe}$, with an exponent of -1.5 that is consistent with the possibility of transient growth in the initial steps of the transition process[38,39,40,41]. The type of the perturbation can induce many different patterns, including horshoe-like

[35]Davies SJ and White CM. An experimental study of the flow of water in pipes of rectangular section. *Proc. R. Soc. Lond. A* 119 (1928)

[36]Waleffe F. On a self-sustained process in shear flows. *Phys. Fluids* 9(4):883-900 (1997)

[37]Tasaka Y, Schneider TM, Mullin T. Folded edge of turbulence in a pipe. *Phys. Rev. Lett.* 105:174502 (2010)

[38]Trefethen LN, Trefethen AE, Reddy SC, Driscoll T.A. Hydrodynamic stability without eigenvalues. *Science* 261:578–583 (1993)

[39]Henningson DS and Kreiss G. Threshold amplitudes in subcritical shear flows. In *Proc. IUTAM Symposium Laminar–Turbulent Transition and Finite Amplitude Solutions* (ed. T. Mullin & R. Kerswell) 232–245. Springer (2005)

[40]Mellibvosky F and Meseguer A. The role of streamwise perturbations in pipe flow transition. *Phys. Fluids* 18:074104-9 (2006)

[41]Mellibvosky F and Meseguer A. Critical thresholds in pipe flow transition. *Phil. Trans. R. Soc.* A 367:545-560 (2008)

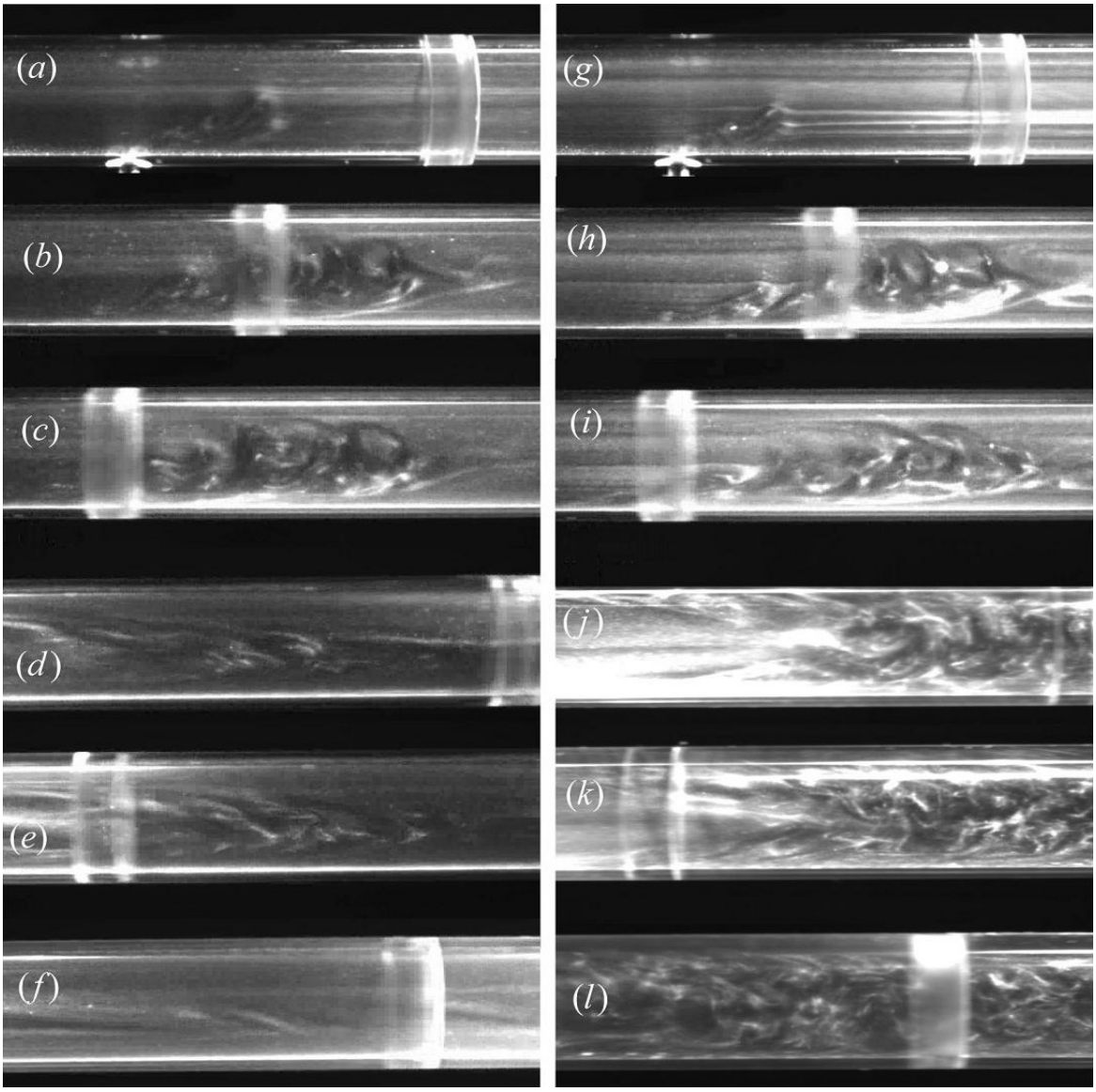

Figure 2.5: Development of a perturbation where a small amount of fluid was impulsively injected into the bulk flow through a 3 mm hole. The diameter of the pipe is 20 mm and the flow is from left to right. $Re = 2000$ and the perturbation decays in the sequence of photographs (a)-(f). Images taken at 1, 2, 3, 6, 14 and 30 diameters downstream from the injection point using a camera travelling with the flow. In the sequence (g)-(l) a slightly larger amount of fluid is injected and the disordered patch gets sustained. Reproduced from Mullin and Peixinho[19].

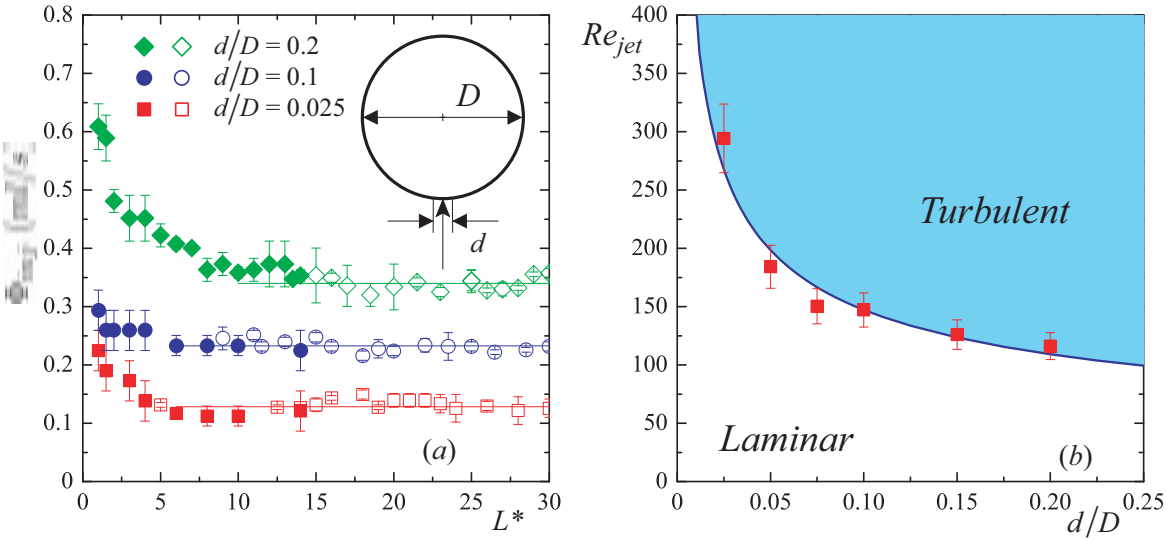

Figure 2.6: Effect of the size of the hole adapted from Peixinho and Mullin[28] (a) Φ_{inj} versus the injection time $L^* = Ut/d$ for different jet diameters d (diamonds: $d = 0.2D$; circles: $d = 0.1D$; squares: $d = 0.025D$) for different Re (filled symbols: $Re = 2500$; open symbols $Re = 5000$) and (b) the critical $Re_{jet} = 4\Phi_{inj}/\nu\pi d$ versus d/D. The line is a least-squares fit $Re_{jet} \propto (d/D)^{0.5}$. Replotted from Peixinho and Mullin[29].

structure[29,42,43].

However, a probabilistic treatment of the results are necessary as the boundary between laminar and disordered pipe flow can be quite complex. Figure 2.7 present an example on the finite amplitude diagram for a push-pull disturbance[29] and the probability of producing a wave, a puff or a slug[37]. Note the size of the error bars that represent the spread over several experimental runs. In some range of Re, the amplitude is clearly not monotonous. The finding of the exponent requires a large range of Re to minimise the error on the exponent. The search the exponent can help elucidate the route to turbulence associated to the development of spatially localised disturbances: Orr mechanism, oblique wave interaction, lift-up, streak bending, streak breakdown and spanwise spreading[44]. Other flows: plane Couette flow[45] or torsional Couette flow[46] have found such boundaries and amplitude stability curve.

[42] Asén P. Stability of plane Couette flow and pipe Poiseuille flow. *Ph.D. thesis, KTH Mechanics* (2007)

[43] Asén P, Kreiss G, Rempfer D. Direct numerical simulations of localized disturbances in pipe Poiseuille flow. *Computer & Fluids* 39:926-935 (2010)

[44] Duguet Y, Monokrousos A, Brandt L, Henningson DS. Minimal transition thresholds in plane Couette flow. *Phys. Fluids* 25(8):084103 (2013)

[45] Bottin S and Chaté H. Statistical analysis of the transition to turbulence in plane Couette flow. *Eur. Phys. J. B* 6:143-155 (1998)

[46] Le Gal P, Tasaka Y, Nagao J, Cros A, Yamaguchi. A statistical study of spots in torsional Couette flow. *J. Eng. Math.* 57:289-302 (2007)

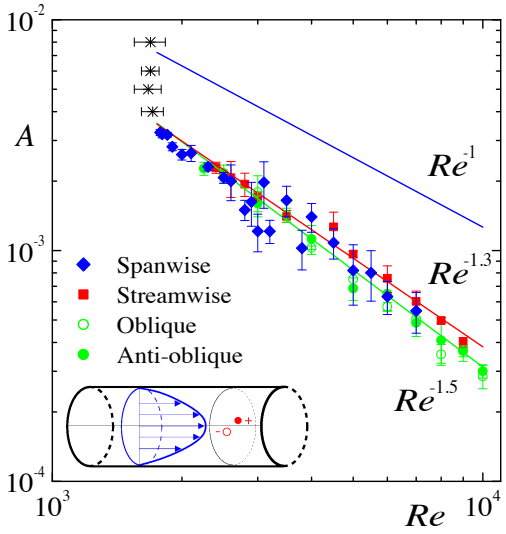

Figure 2.7: Finite-amplitude thresholds for the push-pull disturbance adapted from Peixinho and Mullin[29]. In the lower left-hand corner of the figure, the schematic represents the oblique disturbance which scale with $Re^{-1.5}$. Spanwise disturbance (alignment of the red holes perpendicular to the flow direction) and streamwise disturbance scale with a $Re^{-1.3}$ fit. Also shown is the Re^{-1} fit for the single jet data.

Reynolds[5] described the transition using the words "flashes" and "sinuous motion" as can be seen from the movies of the original experiment included in the supplemental materials of Eckhardt *et al.*[32]. Later detailed experimental studies[9,10,47,25,30] described this localised turbulence as puffs. In the range $1500 \lesssim Re \lesssim 2100$, the motion of fluid in the pipe is intermittent if the incoming flow is disturbed. The flow is made of several puffs along the pipe. These patches of disordered flow seem to have a constant length $\sim 20D$, a sharp trailing edge and a wave at their front.

The discovery of the nonlinear travelling solutions of the Navier-Stokes in pipe flow in a range of Re that was close to the puff regime lead to many discussions about the meaning and the significance of these solutions in regard to the turbulent puff state[22,48,49]. It has been suggested that these solutions calculated from symmetry reduced dynamics are now numerous and of different kinds (symmetric, asymmetric, mirror-symmetric, helical, etc.). These families of traveling waves have also periodic orbits and support the dynamical system interpretation of periodic orbits as "backbone" of turbulence in pipe.

[47]Wygnanski IJ, Sokolov M, Friedman D. On transition in a pipe. Part 2. The equilibrium puff. *J. Fluid Mech.* 69:283–304 (1975)

[48]Duguet Y, Willis AP and Kerswell RR. Transition in pipe flow: the saddle structure on the boundary of turbulence. *J. Fluid Mech.* 613:255–274 (2008)

[49]Pringle CCT, Duguet Y, Kerswell RR. Highly symmetric travelling waves in pipe flow. *Phil. Trans. Roy. Soc.* A 367:457-472 (2009)

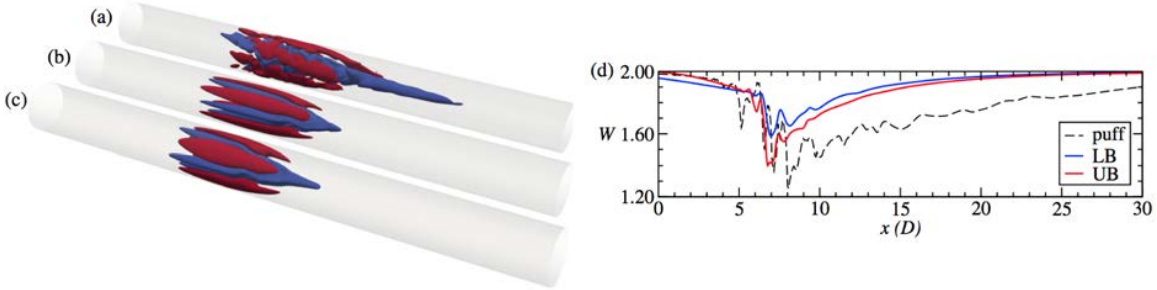

Figure 2.8: Localised relative periodic orbits solutions of the Naviers-Stokes equations from Avila *et al.*[54] for (a) a turbulent puff at $Re = 1900$ and reflection-symmetric relative periodic orbits with π-rotational-symmetry at: (b) the edge, lower branch (LB) of the solution, at $Re = 1900$ and (c) upper branch (UP) at $Re = 1500$. Iso-surfaces of stream-wise velocity at $0.2U$ (red) and $-0.2U$ (blue) are shown. The laminar profile has been subtracted in all cases to highlight the three-dimensional structure of the flow and the views have been shrank by a factor of 4 in the stream-wise direction. $40D$ are shown out of a simulation domain of $50D$. (d) Stream-wise velocity along the pipe centreline for the structures in (a)-(c).

Indeed, the cross-sections of the velocity of the travelling waves resemble at least qualitatively selected experimental slices of turbulence puff. Furthermore, the travelling speed of the travelling wave solutions are reasonably similar to the puff traveling speeds that is slightly lower than the mean flow velocity. Then, it has been made clear that the energy of the bulk flow passing through the puff and the deceleration of fluid particle is a mechanism[50] that leads to low-speed streaks, vortex layer, Kelvin-Helmholtz instability and turbulence.

Thanks to the development of high speed particle image velocimetry[51,14] and direct numerical simulations[52,53] applied to pipe flow, it is now possible to identify the domain of existence and the recurrence time of travelling waves. Yet, the travelling solutions are periodic along the whole pipe axis whereas the puff is localised with a long pipe with laminar flow at the front and at the rear. In the higher range of $Re \gtrsim 2\ 500$, when the turbulence grows and invade the surrounding fluid, the travelling solutions seem to be less recurrent/relevant and other models of spreading of turbulence are necessary.

Recently, numerical localised numerical solutions with a few number of modes is be-

[50] Shimizu M and Kida S. A driving mechanism of a turbulent puff in pipe flow. *Fluid Dyn. Res.* 41:045501 (2009)

[51] van Doorne CWH. Stereoscopic PIV on transition in pipe flow. *Ph.D. thesis, Technische Universiteit Delft* (2004)

[52] Willis AP and Kerswell RR. Critical behavior in the relaminarization of localized turbulence in pipe flow. *Phys. Rev. Lett.* 98:014501 (2007)

[53] Willis AP and Kerswell RR. Coherent structures in localised and global pipe turbulence. *Phys. Rev. Lett.* 100:0124501 (2008)

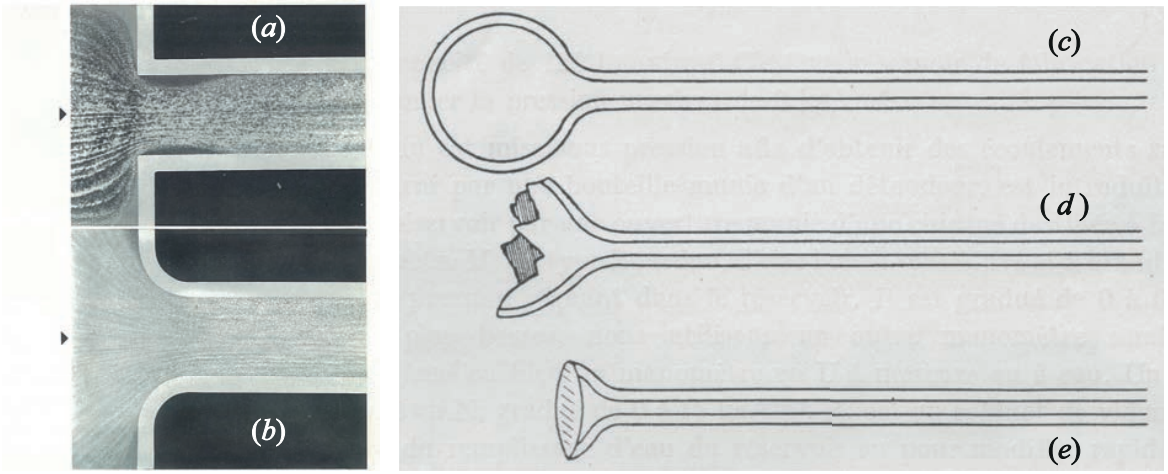

Figure 2.9: (*a-b*) Photographs of entrance flow experiments from the Japan Society of Mechanical Engineers[58] using the hydrogen flow method in a sudden contraction and a rounded contraction. The separation as well as the subsequent aceleration of the flow lead to instabilities and energy loss. (*c-e*) Schematic of the procedure used by Comolet[7] to manufacture smooth inlet pipes from blown glass.

lieved to have most of the fundamental ingredients for making a long lived puff[54,55], see figure 2.8.

The research of transition close to the transition point aims at well defined structures resembling the numerical travelling wave solutions. It was the hypothesis of the relaminarisation experiments of Peixinho and Mullin[56] that lead to wavy patches. Yet these wavy structures were not seen systematically. The half lifetime increases rapidly with Re. Later reports using direct perturbations, very long pipes and large statistic reported a super-exponential growth and a transition to puff splitting[57] at $Re = 2040$.

2.2 Entrance flow

Although most of the theoretical studies deal with the stability of the HPF, that is the fully developed flow. There are several experiments using controlled perturbations that indicate that the flow entering a pipe through a bell-shaped inlet becomes unstable to small-amplitude disturbances at values of Re much lower than those predicted by

[54]Mellibovsky F, Meseguer A, Schneider TM, Eckhardt B. Transition in localized pipe flow turbulence. *Phys. Rev. Lett.* 103(5):054502 (2009)

[55]Avila M, Mellibovsky F, Roland N, Hof B. Streamwise-localized solutions at the onset of turbulence in pipe flow. *Phys. Rev. Lett.* 110:224502 (2013)

[56]Peixinho J and Mullin T. Decay of turbulence in pipe flow. *Phys. Rev. Lett.* 96:094501 (2006)

[57]Avila K, Moxey D, De Lozar A, Avila M, Barkley D, Hof B. The onset of turbulence in pipe flow. *Science* 333, 192–196 (2011)

theory[58,59]. The entry flow does have a significant role in all experimental investigations of the transition to turbulence in a pipe. Disturbances can be minimised using honeycombs and screens[10,26,30,60]. Another potential source of disturbances originates from the shape of the inlet, at which a sharp-edged entry may induce separation and instability[9]. The example of the vena contracta effect is show in figure 2.9(a). Specially designed bell-mouth contractions[5,25] should be used to avoid inlet disturbances and produce the steady development of HPF over a wide range of Re. An elegant way to produce bell shaped inlet is reproduced in figure 2.9(c-e) as proposed by Comolet[7]. As many flows of engineering interest may have both disturbed flow and sharp entry conditions at the inlet, these aspects deserve attention in experimental investigations.

In attempting to control the inlet flow, most of the previous experimental investigations were concerned with the natural transition, in contrast to forced transition where a perturbation is added to the flow[58]. There are a large variety of perturbations such as wires, roughness elements, or partial blockages. Clearly, the type, the shape, the amplitude, the duration, the frequency and the position of the perturbation can have a significant effect[61,29]. Furthermore, there are several criteria to consider the development and establishment of fully developed turbulent flow. Measurements of the statistics of centreline velocity were used to assess the axial location for fully developed turbulence[10,19,62]. According to Zanoun *et al.*[62] and Zagarola and Smits [63], most of the transition to turbulence occurs in the entrance region up to 60 diameters from the inlet. Figure 2.10 presents the centreline velocity statistics at several position along the pipe, x/D, and the velocity statistics evolve until reaching a steady behaviour from $x/D \approx 60$. Yet the entrance length for perturbed and fully developed pipe flow (at relatively high Re) is not well understood.

EuHIT[64] is supporting our collaboration with Emir Öngüner, Christoph Egbers, BTU Cottbus, Germany and El-Sayed Zanoun, Cairo, American University Cairo, Egypt. The proposed research will contribute to the understanding of the flow development in turbulent pipe flow using a complementary analysis of the correlation of pressure and velocity measurement in the entrance region for controlled perturbations in the high Reynolds pipe flow facility at BTU Cottbus-Senftenberg, Cottbus, Germany[60]. Figure 2.11 is a schematic representation of the pipe flow experiment where pressure taps are available all

[58]Sarpkaya T. A note on the stability of developing pipe flow subject to axisymmetric and non-axisymmetric disturbances. *J. Fluid Mech.* 68:345–51 (1975)

[59]Williams SD. An investigation of the stability of developing pipe flow. *Ph.D. thesis, University of Manchester* (2001)

[60]König F, Zanoun ES, Öngüner, Egbers C. The CoLa pipe, the Cottbus large pipe test facility at Brandenburg University of Technology Cottbus-Senftenberg. *Rev. Sci. Instrum.* 84:075115 (2014)

[61]Fransson JHM, Talamelli, Brandt L, Cossu C. Delaying transition to turbulence by a passive mechanism. *Phys. Rev. Lett.* 96:064501 (2006)

[62]Zanoun ES, Kito M and Egbers C. A study on flow transition and development in circular and rectangular ducts. *J. Fluids Eng.* 131:061204 (2009)

[63]Zagarola MV and Smits AJ. Mean-flow scaling of turbulence pipe flow. *J. Fluid Mech.* 375:33-79 (1998)

[64]European High-Performance Infrastructure in Turbulence: www.euhit.org

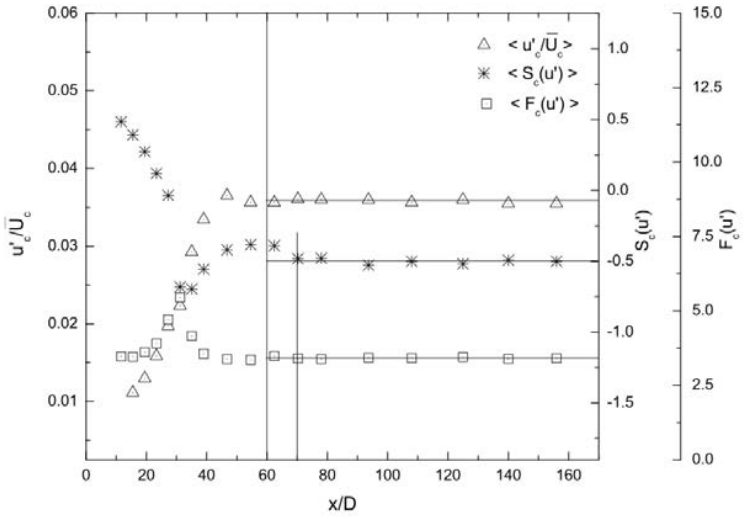

Figure 2.10: Centreline turbulence statistics of the axial velocity versus x/D reproduced from Zanoun *et al.*[62]. $u'_c/\overline{U}_c$, S and F are the second, third and fourth order statistic of the centreline velocity for 30 000 $< Re <$ 80 000 and no tripping.

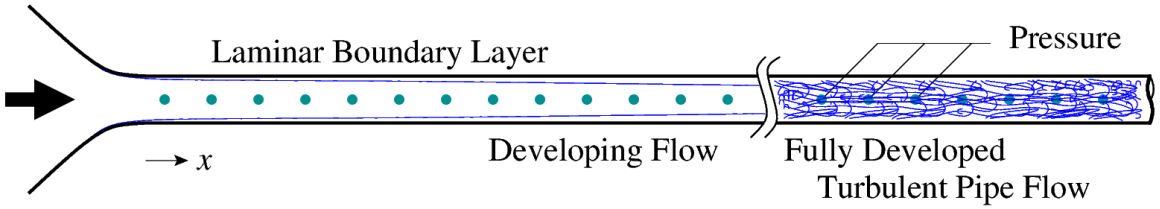

Figure 2.11: Schematic of the developing pipe flow transition. The flow is from left to right, the dots indicate the position of pressure taps and the blue line in the developing region represent the developing boundary layer.

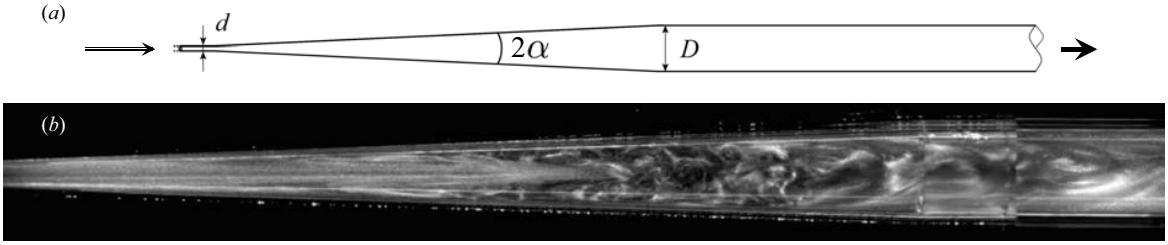

Figure 2.12: (a) Schematics of the diverging pipe experiment, and (b) a flow visualisation photograph for $Re = 1000$ ($\alpha = 2°$ and $D/d = 8.79$). The flow is from left to right.

along the pipe to monitor the pressure as the flow develops and for different perturbation at the inlet.

2.3 Gradual expansion pipe flow

A motivation in the study of transition to turbulence is to found the continuation or the connection between the transition scenario in uniform (constant diameter) pipe flow and in diverging pipe flow, schematised in figure 2.12(a). Here, the inlet pipe diameter is d, the outlet pipe diameter is D and the diverging section has an angle 2α, a length L and an aspect ratio $\beta = L/d$. Using axisymmetric numerical simulation, we first quantified the existence of the recirculation cells that are always observed in expansion flow. It was shown in a previous work[65] that it disappears when the angle is too small. Another result is that the existence of the recirculation is not due to an empirical rule about a critical angle, but a combination of parameters, that are the diverging angle, α, and the inlet Reynolds number, $Re = Ud/\nu$. Note Re is defined using the inlet diameter. As anticipated, for small angle it required larger flow rates to initiate the recirculation cell[66]. Eventually, for small α, a small change in the angle α will require a large change in the critical Re to sustain the long thin recirculation regions close to the diverging pipe wall.

Experiments were performed with the smallest tapered angle possible to obtain: 4°. We observed the thin recirculation cell prior to turbulence. However, flow visualisation did not allow to measure the linear growth of the recirculation cell. It is then assumed that this basic state is unstable in the experiment. The counter flow and the asymmetry of the flow can clearly be identified, corresponding to negative velocities. A large region of the pipe cross-section is moving against the bulk flow. There are analytical solutions for axisymmetric velocity profiles in diverging pipe flow, known as Jeffery-Hamel solutions, but their calculation require several adjustable parameters. At $Re = 600$, the velocity profile is asymmetric suggesting that the recirculation region also is asymmetric, although the

[65]Peixinho J and Besnard H. Transition to turbulence in slowly divergent pipe flow. *Phys. Fluids* 25:111702 (2013)

[66]Swaminathan G, Sahu KC, Sameen A, Govindarajan R. Global instabilities in diverging channel flows. *Theor. Comput. Fluid. Dyn.* 25:53–64 (2011)

flow seems to be steady (no time dependence). The asymmetric velocity profile contains inflection points and these as know to cause the onset of Kelvin-Helmholtz instabilities.

As the Reynolds number is increased, shear layer instability lead to bursts of turbulence to appear and a surprising feature of the flow is the formation of a stationary turbulent patch that remains localised in space. A flow visualisation photograph is presented in figure 2.12(b). This patch of disordered flow resembles the turbulent puff of uniform pipe flow. Yet there are a number of differences: (i) the disordered patch contains counter rotating cells in the trailing edge, (ii) its length varies with the Re and (iii) relaminarisation experiment suggest a linear decay time with Re.

In order to complete our experimental data, a series of numerical simulations taking advantage of open-access availability of parallel numerical codes. We performed a number of simulations[67] in a circular pipe expansion flow with a radius ration $E = D/d = 2$ and $\alpha = 26.57°$ at various Re. The high resolution three-dimensional simulation ($\sim 1.8 \times 10^6$ grid points on a $150d$ long domain) with a small amplitude perturbation ($\delta = 0.001$) found a symmetry breaking bifurcation at $Re_c = 912$, then periodic velocity oscillations in a small range of Re prior the breakup to localised turbulence. The oscillation suggests Kelvin-Helmholtz instability. The localised turbulence was analysed using spacial correlation on the streamwise velocity at $r = 0.5$ and $0.8d$. It identified the fast and slow streaks which dominate the disordered turbulent patch. The main finding is that the localised turbulence is controlled by core modes contrary to the turbulent puffs of uniform turbulent pipe that are dominated by wall modes with three-fold symmetry[53].

The fluctuations or unsteady character of the localised turbulent patch is investigated using the method of Proper Orthogonal Decomposition (POD). This method is applied to a sequence of 5000 images from the previous simulations in a cross-section slice at $z = 22.5d$ from the diverging section. POD is a popular tool and has been extensively used for the identification of coherent structures in turbulent flows[68]. POD basically ranks the most significant structures in the flow field. Using only the most energetic of those features, it is possible to reconstruct and obtain an optimal representation of the initial data. Here, POD is used in order to identify and study the large-scale vortices in the turbulent flow. The first step is to calculate the mean velocity field, which can be considered the zeroth mode of the POD. The rest of the analysis concerns the fluctuating parts of the velocity components. Figure 2.13 presents the first three most energetic modes of the localised turbulence for $Re = 2000$ that represent more than 99% of the energy of the flow. It suggests again that most of the energy is localised in the shear region between the core flow and the recirculating region.

Taking advantage of this geometrical configuration, one have the possibility to study localised turbulence as the inlet is laminar HPF. Downstream, the outlet section has a larger diameter and relaminarisation is likely to occur if the pipe is long enough. Moreover this patch of disordered flow is localised in space. It is then relatively easy to measure

[67]Selvam K, Peixinho J, Willis AP. Localised turbulence in a circular pipe flow with gradual expansion *J. Fluid Mech.* 771:R2 (2015)

[68]Meyer KE, Pedersen JM, Özcan O. A turbulent jet in crossflow analysed with proper orthogonal decomposition. *J. Fluid Mech.* 583:199-227 (2007)

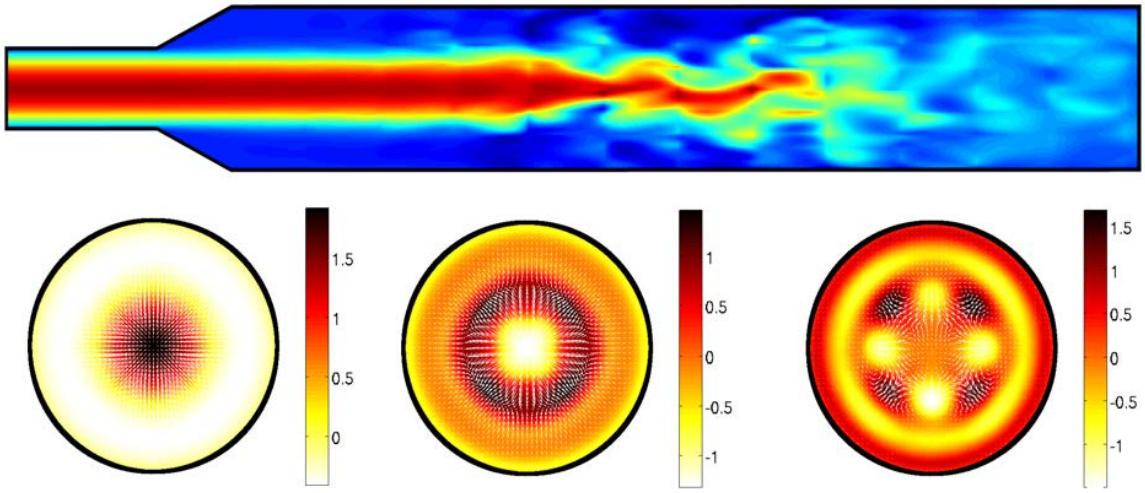

Figure 2.13: (Top) Velocity magnitude of the localised turbulence at $Re = 2000$ ($20d$ are shown out of a simulation domain of $150d$). (Bottom) Contour of the first, second and third most energetic POD modes of the localised turbulent puff in a diverging pipe flow ($\alpha = 25.57°$, $E = D/d = 2$) at $z = 12.5d$ from the inlet of the diverging section.

fluctuation quantities and perform statistical analysis to qualify the type of turbulence.

At higher Re, it is expected that the localised turbulent patch will split and another turbulent patch will emerge and will advected downstream the expansion pipe. This splitting phenomena has some similarities to the splitting with the vortex shedding behind a cylinder and the puff splitting in uniform pipe. It is conjectured that these phenomena: break up of turbulent from recirculation regions and vortex shedding are dependent on the angles and aspect ratio of the expansion pipe. In a collaboration with Ashley Willis of the University of Sheffield, UK, tools and analysis of numerical simulations are in development through the thesis of Kamal Selvam (October 2013 - October 2016) to explore the various mechanism possible in expansion pipe flow. Testing experimentally all possible geometries is not possible, but simulating a definite number of cases and testing several in experiments will allow for a more precise estimate of the pressure loss in such geometries.

2.4 Non-Newtonian expansion pipe flow

In experiments, it is also relatively simple to change the nature of the fluid and study turbulence in complex fluids (viscoelastic or viscoplatic fluids). From a numerical point of view, it introduces a constitutive equation for the behaviour of the fluid. This equation

couples with the Navier-Stokes equations (2.4). There has been many 2D calculations[69,70] and few experimental studies on expansion flows, because most of the studies on non-Newtonian fluid flow are concerned with die swell or extrudate swell (contractions). It is a common phenomenon in polymer processing occuring when a polymer stream is compressed into a die, and is followed by a partial recovery or "swell" back to the former shape and volume of the polymer after exiting the die.

There are many model that claim to represent homogeneous polymer solution, hence having the properties of both viscosity and elasticity. One of the most popular model, the Oldroyd-B model, is an extension of the Upper Convected Maxwell model and is equivalent to a fluid filled with elastic bead and spring dumbbells[71]. Although it introduced several new parameters: the Weissenberg number and the polymer viscosity ratio, defined below, it assumes constant shear viscosity and a single relaxation time, λ. It should be validated against experiments depending on the type and concentration of polymer dissolved.

Hence, polymer solutions can be simulated using initially 2D simulations of the Oldroyd-B model for an expansion flow of expansion ratio $E = D/d = 6$ and angle $\alpha = 45°$. The nondimentional equation system is:

$$\nabla \cdot \boldsymbol{v} = 0 \tag{2.7}$$

$$Re\,(\boldsymbol{v}\cdot\nabla)\,\boldsymbol{v} = \nabla\cdot\left\{-P\underline{\underline{\mathbf{I}}} + \mu_s\left[\nabla\boldsymbol{v} + (\nabla\boldsymbol{v})^T\right] + \underline{\underline{\mathbf{T}}}\right\}, \quad \text{where} \tag{2.8}$$

$$\underline{\underline{\mathbf{T}}} = We\left\{\left[(\nabla\boldsymbol{v})\,\underline{\underline{\mathbf{T}}} + \underline{\underline{\mathbf{T}}}\,(\nabla\boldsymbol{v})^T\right] - (\boldsymbol{v}\cdot\nabla)\,\underline{\underline{\mathbf{T}}}\right\} + \mu_p\left[\nabla\boldsymbol{v} + (\nabla\boldsymbol{v})^T\right]. \tag{2.9}$$

$We = \lambda U/d$ is the Weissenberg number and $\mu_p = \mu_p/(\mu_s + \mu_p) = \mu_p/\mu = 1 - \mu_s$ is the relative viscosity of the polymer and the solvant. There are a number of boundary conditions: zero normal velocity at the centreline, zero total stress at the centreline, zero total tangential stress at the centreline, no slip velocity at the wall and no normal stress at the wall. At the inlet, the velocity is considered laminar and parabolic.

Figure 2.14 presents some of the results for the laminar stationary solutions. It seems that the onset for the appearance of the recirculation cell is not affected by the non-Newtonian properties of the flow. However, once the recirculation cells are present, their characteristic length grows slowly compared to the Newtonian counterpart. Note that the current simulation are considering creeping flow (no inertia).

There are a number of open questions regarding the effect of viscoelasticity on the expansion flow. How will the viscoelastic properties affect the flow pattern? More specifically, the length of the recirculation, the onset of shear flow instabilities, the onset of viscoelastic instabilities. What will happen if the recirculation time and the relaxation time resonate? It seems possible to develop predicting tools and validate them through experiments.

[69] Poole RJ, Alves MA, Pinho FT. Plane sudden expansion flows of viscoelastic liquids. *J. Non-Newton. Fluid Mech.* 146:79-91 (2007)

[70] Poole RJ, Pinho FT, Alves MA, Oliveira PJ. The effect of expansion ratio for creeping expansion flows of UCM fluids. *J. Non-Newton. Fluid Mech.* 163:35-44 (2009)

[71] Tanner RI, Engineering rheology. *Oxford University Press, New York* (2000)

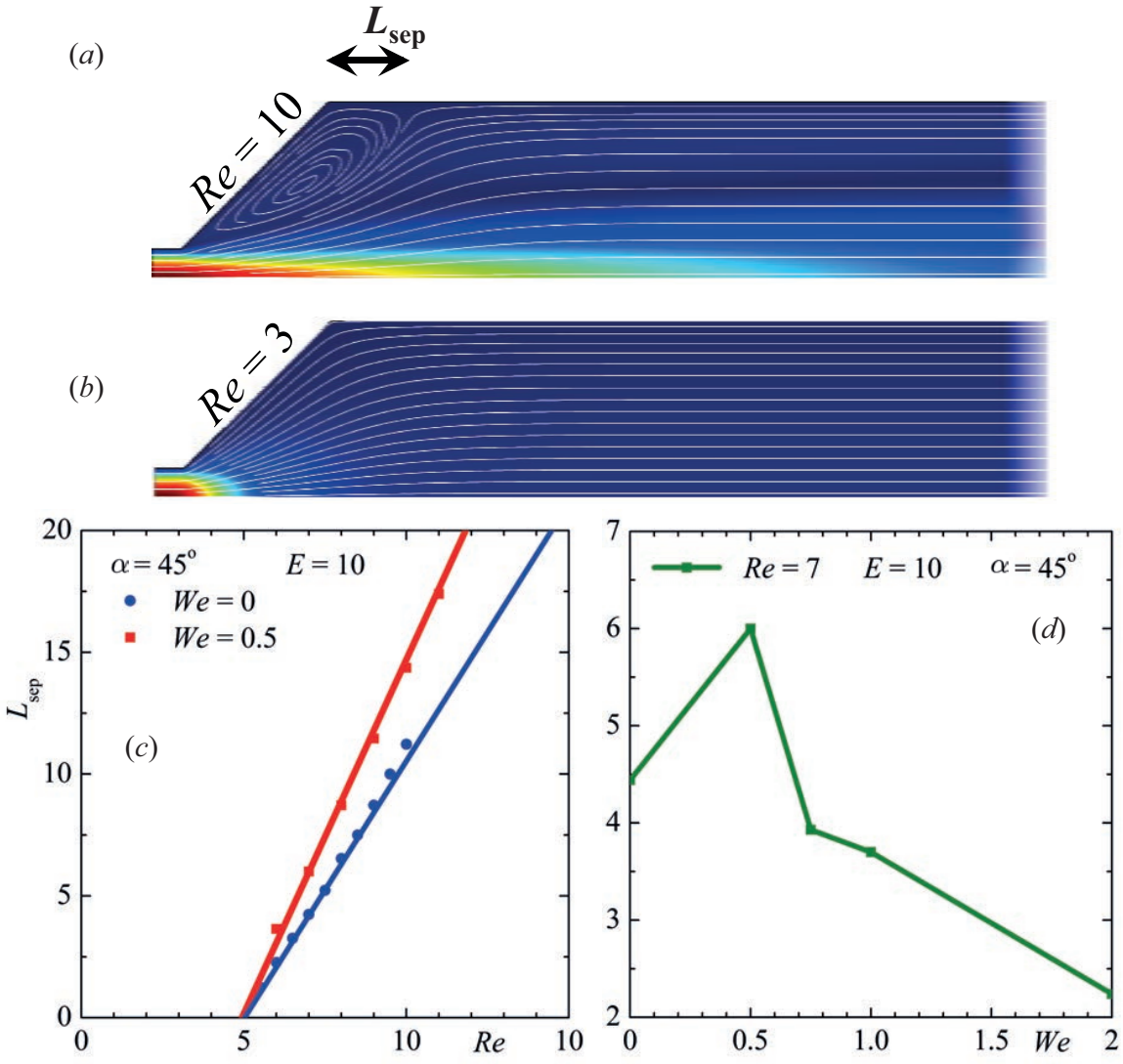

Figure 2.14: 2D numerical simulation of Oldroyd-B flow in an expansion flow ($E = D/d = 6$ and $\alpha = 45°$). (a) Velocity map and velocity streamlines at $Re = 3$, (b) $Re = 10$. (c) The length of the recirculation cell as a function of Re for $We = 0$ and 0.5. (d) L_{sep} as a function of We.

2.5 Future perspectives

Although the transition phenomena for expansion pipe flows seem well understood, there are still many open questions. How does the sequence of bifurcations identified in uniform pipe flow and diverging pipe flow depend on the perturbation imposed at the inlet? Can an optimal defect be identified, such as done in pipe flow by Gavarini *et al.*[72], that would reveal the lowest value of Re for which turbulence can arise, if not sustain? As in straight pipes, the system is shown to admit a multiplicity of solutions for the same parameter range since both axisymmetric laminar (with low drag) and turbulent (with high drag) can coexist. This multiplicity makes flow control strategies interesting, provided a method is found to reduce the basin of attraction of the non-turbulent solutions. Can exact finite-amplitude solutions be identified for a better description of the dynamics inside the turbulent patch (Duguet *et al.*[48])? Can one unfold a full bifurcation sequence from a dynamical systems point of view, as in Avila *et al.*[57]? Turning our attention to the spatiotemporal properties of the turbulent patches, the analogy with straight pipe flow can be pushed further. The novel evidence for an asymmetric mode closer to the centreline of the pipe calls for future investigation as it suggests a clear difference with usual puffs. How crucial is this difference and how does it affects the dynamics or the potential to control it? Other geometric parameters (angle, expansion ratio, etc.), as well as other geometries could also be considered and varied. This can be particularly interesting from an industrial perspective, again as a way to passively control or delay the emergence of the turbulent patches.

2.5.1 Entrance flow

Concerning entrance pipe flow, which seems the most convenient location for control, the Cottbus pipe has a smooth inlet 8:1 contraction and a settling chamber with screens to damps disturbances. In a previous investigation, laminar pipe flow could be obtained up to $Re = 12\,300$ at 70 diameters from the inlet. At higher Re, all the reports indicate fully developed turbulence at 40 diameters from the inlet. The goal of the EuHIT proposal is to clarify the effect of controlled perturbations in this region using experiments. The most common perturbations are annular ring obstacles of different heights. Previous experiments dealt with jets and push/pull disturbances. Yet all previous perturbations take place at a fixed narrow location and the effects are monitored downstream. What would happen if one can exert a constant blow/section over a relatively long axial distance? Is it possible to prevent entrance transition and turbulence in high Reynolds pipe flow?

2.5.2 Experiments

From the experimental point of view, we plan to modify the Le Havre experimental setup[65] to drive the flow both in pressure driven and constant mass flux. At the moment, the

[72] Gavarini MI, Bottaro A, Nieuwstadt FTM. The initial stage of transition in pipe flow: role of optimal base-flow distortions. *J. Fluid Mech.* 517:131–165 (2004)

driving is using a series of glass seringues and a seringue pump. It is not clear if the change in driving can alter the critical Reynolds numbers in the transition scenario. Another important control parameter is the perturbation and its development into localised turbulence in diverging pipe expansion. We already collaborate with Yuji Tasaka (University of Hokkaido) in building a pipe flow facility in Sapporo and developing a synthetic jet actuator.

In the range of large Re, we would like to test if the localised turbulence can split just as in uniform pipe flow or in the flow behind a sphere (vortex shedding). Our previous measurements indicate that the puff grows in size as Re increases. This will also require to extend the pipe setup.

Another interesting problem is the effect of complex fluids on transition sometimes called viscoelastic turbulence or elasto-inertial turbulence[73]. Our preliminary investigation indicates that viscoelastic turbulence will lead to short elongated disordered flow structures. Besides, the study of viscoplastic turbulence is also challenging as it requires a very accurate visualisation system to detect the presence of yielded regions.

2.5.3 Numerical simulations

From a numerical point of view, our current tools, developed in collaboration with Ashley Willis, University of Sheffield, UK, within the thesis of Kamal Selvam (September 2013 - September 2016), allow us to reproduce disordered turbulent patches in a divergent pipe flow. The effect of various perturbations is been tested and the effects on the resulting turbulent patches is been analysed. How does it depend on the perturbation parameters, the pipe geometrical parameters and the Reynolds number? Although it is possible to reproduce turbulent patches in relatively long computational domains, the direct comparison is not straightforward as the wall geometry is not exactly the same (geometrical imperfections).

Results have been presented on preliminary 2D simulation of viscoelastic expansion flow. The effect of complex fluids polymer solutions (viscoelastic and viscoplastic models) will be first investigated using numerical simulations for the basic states (small but finite Re). Then the results will be compared to experiments.

Our numerical reproduction of disordered flow in a diverging pipe can provide us with many flow velocity snapshots of the turbulent flow. Statistical analysis of these data is in progress through the use of correlation functions[67] and POD analysis[74]. These methods are applied first in our simulation results. It is then planned to use theses techniques on experimental data.

Although the transition Re, in pipe flow, are relatively large, theses pipes lengths can now be simulated in computer clusters using open source codes. The strategy adopted here is to avoid using periodic boundary conditions and try to simulate relatively long

[73] Samanta D, Dubief Y, Holzner M, Schäfer C, Morozov AN, Wagner C, Hof B. Elasto-inertial turbulence. *PNAS* 110(26) 10557–10562 (2013)

[74] Basley J, Pastur LR, Lusseyran F, Soria J, Delprat N. On the modulating effect of three-dimensional instabilities in open cavity flows. *J. Fluid Mech.* 759:546-578 (2014)

domains and the development of perturbations at the inlet. This is shown to produce a large variety of flow structure, including helicoidal vortices, hairpin vortices. Here again, there are many questions about the validity of the resolution of the simulation results. How well and efficient are the imperfections/disturbance reproduced in simulations?

Chapter 3

Recent observations in Taylor-Couette flow

Although Taylor-Couette is a well studied flow, it has recently gain attention due to the search for scaling laws in turbulent flow (Eckhardt *et al.*[1]). The proposed scalings aims to unify the formalism for momentum, heat and mass transfer. These arguments have been successful in turbulent Rayleigh-Bénard flow.

Another feature of Taylor-Couette flow is its remarkably varied patterns and its chaotic behaviour. It has been intriguing physicists for over 300 years[2]. This system is a place where many non-linear phenomena can be studied quantitatively in experiments and in simulations. There is now a number of numerical codes that can reproduce various types of Taylor-Couette flow transition, both single phase and multiphase flow. Yet many phenomena remain unexplained and the example of particle suspension flow in a partially filled cell is described below where unexpected banded phenomena can be observed.

This chapter is divided into three parts. In a first part, our recent experiments on turbulent Taylor-Couette flow and the observation of multiple states related to different torque levels are recalled. The effect of different radius ratio is also highlighted. In a second part, several issues about the heat transfer in turbulent Taylor-Couette flow are described. In the third part, a number of Taylor-Couette experiments with complex fluids are presented, these look at two fluids and polymer fluids at relatively small velocities.

Publications associated with this chapter

- Jorge Peixinho, Parisa Mirbod and Jeffrey F. Morris. Free surface flow between two horizontal concentric cylinders. *Eur. Phys. J. E* 35:19 (2012) (Cover)
- Borja Martínez-Arias, Jorge Peixinho, Olivier Crumeyrolle and Innocent Mutabazi. Effect of the number of vortices on the torque scaling in Taylor-Couette flow. *J. Fluid Mech.* 748:756-767 (2015)

[1]Eckhardt B, Grossmann S, Lohse D. Torque scaling in turbulent Taylor-Couette flow between independently rotating cylinders. *J. Fluid Mech.* 581:221-250 (2007)

[2]Newton considered the circular motion of fluids in Book II, Section IX, of the *Principia* (1687)

3.1 Turbulent Taylor-Couette flow

The first reported torque measurements in turbulent Taylor-Couette flow were performed by Wendt[3] and Taylor[4] in systems with different radius ratios. They found that the torque is a good indicator of the different flow regimes. Later, many studies tried to model this measurements using theoretical analysis of the Navier-Stokes equations. Recently, several numerical simulations[5,6,7,8] were carried out to found the influence of the radius ratio on the torque scaling and the transition to the ultimate regime of turbulence (turbulent boundary layer regime).

In our experimental investigations, a Taylor-Couette geometry is fitted on a rheometer (Anton Paar MCR 501). It controls the cylinder rotating velocity accurately though a direct current motor and measures the angular position down to 50 nanoradians. The inner cylinder has a radius $r_i = 50 \pm 0.01$ mm and the outer cylinder $r_o = 55 \pm 0.01$ mm. Hence, the gap between both cylinders is $d = r_o - r_i = 5 \pm 0.01$ mm. The length of the inner cylinder is $L = 150 \pm 0.5$ mm. The dimensionless parameters that describe the geometry are the radius ratio $\eta = r_i/r_o = 0.909$ and the aspect ratio $\Gamma = L/d = 30$.

The object of the experiments was to examine the relationship between the angular speed of the inner cylinder, Ω, and the torque that it exerts on the fluid, T. The Reynolds number, Re, is based on the angular velocity of the inner cylinder, the inner cylinder radius, the gap between cylinders and the properties of the fluid: $Re = \Omega r_i d/\nu$, where ν is the kinematic viscosity of the working fluid. The dimensionless torque, G, is based on the torque exerted by the fluid in the walls of the inner cylinder, the height of the inner cylinder and the properties of the fluid. G is defined as $G = T/\rho\nu^2 L$, where ρ is the density of the working fluid. In addition to G, the so-called ω-Nusselt number, Nu_ω defined according to Eckhardt *et al.*[1], is also used:

$$Nu_\omega = \frac{G}{G_{lam}}, \quad \text{where} \quad G_{lam} = \frac{2\pi\eta Re}{(1-\eta)^2}. \tag{3.1}$$

In our previous investigation, Martínez-Arias *et al.*[9], the effect of the number of vortices in a Taylor-Couette flow up to $Re = 24\,000$ has been quantified. An example of

[3]Wendt F. Turbulente strömungen zwischen zwei rotierenden konaxialen zylindern. *Ing.-Arch.* 4(6):577–595 (1933)

[4]Taylor GI. Fluid fraction between rotating cylinders. I. Torque measurements. *Proc. R. Soc. Lond. A* 157:546-564 (1936)

[5]Ostilla R, Stevens RJAM, Grossmann S, Verzicco R, Lohse D. Optimal Taylor-Couette flow: direct numerical simulation. *J. Fluid Mech.* 719:14-46 (2013).

[6]Ostilla-Mónico R, Huisman S, Jannick TJG, van Gils DPM, Verzicco R, Grossmann S, Sun C, Lohse D. Optimal Taylor-Couette flow: radius ratio dependence. *J. Fluid Mech.* 747:1-29 (2014).

[7]Ostilla-Mónico R, van der Peol EP, Verzicco R, Grossmann S, Lohse D. Exploring the phase diagram of fully turbulent Taylor-Couette flow. *J. Fluid Mech.* 761:1-26 (2014)

[8]Ostilla-Mónico R, van der Poel EP, Verzicco R, Grossmann S, Lohse D. Boundary layer dynamics at the transition between the classical and the ultimate regime of Taylor-Couette flow. *Phys. Fluids* 26:015114 (2014)

[9]Martínez-Arias B, Peixinho J, Crumeyrolle O, Mutabazi I. Effect of the number of vortices on the torque scaling in Taylor-Couette flow. *J. Fluid Mech.* 748:756-767 (2014)

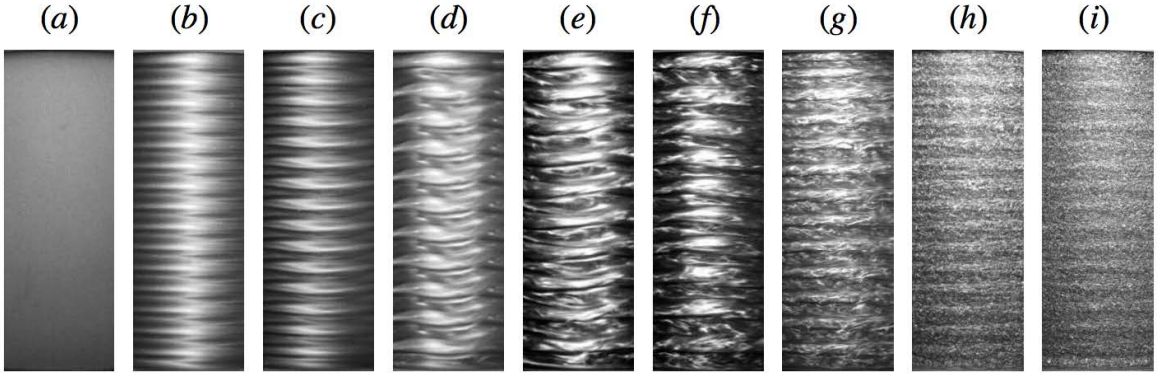

Figure 3.1: Flow visualisation photograph of Couette-Taylor flows using Kalliroscope® at different Reynolds numbers. (a) Laminar Couette flow, $Re = 20$. (b) Taylor vortex flow, $Re = 146$. (c) Wavy vortex flow, $Re = 178$. (d) Modulated wavy vortex flow, $Re = 324$. (e) Chaotic wavy vortex flow, $Re = 1172$. (f) Wavy turbulent vortex flow, $Re = 1513$. (g), (h) and (i) Turbulent Taylor vortex flow, $Re = 6000$, 10 000 and 16 000, respectively.

photographs is the different states in our system is presented in figure 3.1. A specific protocol (based on the acceleration of the inner cylinder) was used to obtain different states with 34, 32, 30, 28, 26, 24, 22, 20 and 18 cells in the gap. Using a combination of flow visualisation and torque measurements, the evolution of Nu_ω versus Re for different number of cells is obtained. The results are in agreement with previous measurement[10,11] and, moreover, the curves superpose self-consistently for different number of cells. The torque is larger for large number of cells for $Re < Re_T$ and smaller when $Re > Re_T$. In addition, these new observations confirm the transition from centrifugal instability to shear turbulence observed before by Lathrop *et al.*[12] and Lewis and Swinney[13]. They showed evidence of a transition point where the torque becomes independent of the number of vortices at $Re_T = 13\ 000$. The scaling exponent of the torque increases with the number of vortices, meaning the turbulent dissipation increases as the number of vortices increases. It is also found that the exponent collapsed when scaled with a Reynolds number based on the aspect ratio of the vortices. This clearly indicate the effect of the number of vortices on the dissipation.

[10]Lim TT and Tan KS. A note on power-law scaling in a Taylor–Couette flow. *Phys. Fluids* 16:140-144 (2004)

[11]Ravelet F, Delfos R, Westerweel J. Influence of global rotation and Reynolds number on the large-scale features of a Taylor-Couette flow. *Phys. Fluids* 22:55103 (2010)

[12]Lathrop DP, Fineberg J, Swinney HL. Transition to shear-driven turbulence in Couette–Taylor flow. *Phys. Rev. A* 46:6390-6405 (1992)

[13]Lewis GS and Swinney HL. Velocity structure functions, scaling and transitions in high-Reynolds-number Couette-Taylor flow. *Phys. Rev. E* 59:5457–5467 (1999)

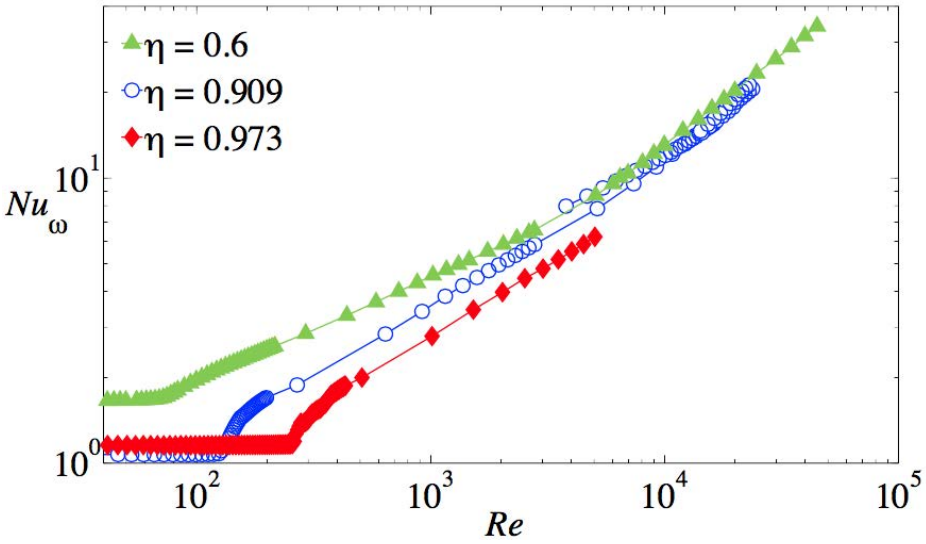

Figure 3.2: Evolution of Nu_ω as a function of Re for different radius ratio η

3.1.1 Effect of the radius ratio

In order to expand our hypothesis about the effect of different number of cells and the torque scaling in turbulent Taylor-Couette flow, additional measurements were performed on new cylinders with inner radius 33 and 53.5 mm. The measurement are presented in figure 3.2 for three radius ratios: $\eta = 0.6$, 0.909 and 0.973 for Re up to 45 000. Clearly, the aspect ratios are also modified as the inner cylinder is changed. The three radius ration $\eta = 0.6$, 0.909 and 0.973 correspond to: $\Gamma = 6.85$, 30 and 100, respectively.

Again, using the acceleration of the inner cylindre it is possible to obtain different number of cells for the same final velocity of the inner cylinder. For example, it is possible to observe 4, 6 and 8 cells (3 states) in the system with $\eta = 0.6$ and $\Gamma = 6.85$. For the system with $\eta = 0.909$, 9 states were observed and the $\eta = 0.973$, the number of states is large typically between 60 and 100. In figure 3.2, in the laminar regime (low Re), the three curves for different η are shifted up due to the end effects that introduce an additional torque with respect to the theoretical laminar torque ($Nu_\omega = 1$) calculated for an infinite cylinder. In the case $\eta = 0.6$, the torque is even larger compared to the other two cases because the aspect ratio is small and hence the end effects are important.

The transition from laminar Couette flow ($Nu_\omega \simeq 1$) to Taylor vortex flow is characterised by an abrupt change in the slope. The critical Re for transition are in agreement with the theory[14] and it decreases with decreasing radius ratio from 0.973 to 0.6. An analytical relationship for the initial slope in the torque was also proposed by DiPrima *et al.*[15] and verified for the current measurements. At relatively large Re, previous investi-

[14]Esser A, Grossmann S. Analytic expression for Taylor-Couette stability boundary. *Phys. Fluids* 8:1814-1819 (1996)

[15]DiPrima RC, Eagles PM, Ng BS. The effect of radius ratio on the stability of Couette flow and Taylor

gations for the case of $\eta = 0.6$ reported the modification of the turbulent Taylor vortices by the presence of Görtler vortices[16] of smaller wavelength[17].

3.1.2 Multiple turbulent states

At larger Re, Nu_ω is higher for small η, suggesting that large gaps induce large velocity fluctuations and large dissipation[18]. It seems also that slope of the $Nu_\omega(Re)$ curve is independent of η. The study of the highly turbulent state will require the measurement of velocity statistics[12,13] to check the statistical properties of this turbulent flow. As many reports[12,19] indicate the presence of large turbulent Taylor vortices still present at $Re = 10^6$, the high-order structure function could be different from the ones in homogeneous turbulence[20]. Turbulent flow at high Re can be understood as the appearance of the ultimate regime where only the boundary layers are turbulent (using the Prandtl-von Kármán law) and homogeneous turbulence in between. An open question is: what is the Re this ultimate regime is attained? The observation of multiple states (of turbulent Taylor cells) at high $Re = \mathcal{O}(10^6)$ turbulence seems to indicate the ultimate regime has not been yet observed and may be reached for higher Re.

3.2 Heated turbulent Taylor-Couette flow

Although many aspects of turbulent Taylor-Couette flow remain to be clarified, we now consider the case of heated turbulent Taylor-Couette flow, specifically Taylor-Couette flow with a radial temperature gradient, as sketched in figure 3.3. This flow involves additional parameters as the heat transfer equation should be taken into account. When weak turbulence is considered, it is usual to take into account the buoyancy forces and the Boussinesq approximation is often used. It assumes the physical properties of the fluid (kinematic viscosity, thermal expansion coefficient, and thermal conductivity) are independent of temperature, while only density in the gravity force term depends linearly on the temperature: $\rho(T) = \rho_0 [1 - \alpha(T - T_0]$, where ρ_0 is the density at a reference temperature T_0 and α is the thermal expansion coefficient.

The governing equation is then controlled by two additional parameters: (i) the Prandtl number, Pr, and (ii) the Grashof number, Gr. $Pr = \nu/\kappa$, represents the ratio of the thermal diffusion time $\tau_\kappa = d^2/\kappa$ to the viscous diffusion time $\tau_\nu = d^2/\nu$, where

flow. *Phys. Fluids* 27(10):2403-2411 (1984)

[16]Faure TM, Adrianos F, Lusseyran F, Pastur L. Visualizations of the flow inside an open cavity at medium range Reynolds number. *Exp. Fluids* 45:169-184 (2007)

[17]Wei T, Kline EM, Lee SHK, Woodruff S. Görtler vortex formation at the inner cylinder in Taylor-Couette flow. *J. Fluid Mech.* 245:47-68 (1992)

[18]Merbold S, Brauckmann HJ, Egbers C. Torque measurements and numerical determination in differentially rotating wide gap Taylor–Couette flow. *Phys. Rev. E* 87:23014 (2013)

[19]Huisman SG, van der Veen RCA, Sun C, Lohse D. Multiple states in highly turbulent Taylor-Couette flow. *Nat. Commun.* 5:3820 (2014)

[20]Anselmet F, Gagne Y, Hopfinger EJ, Antonia RA. High-order velocity structure functions in turbulent shear flows. *J. Fluid Mech.* 140:63-89 (1984)

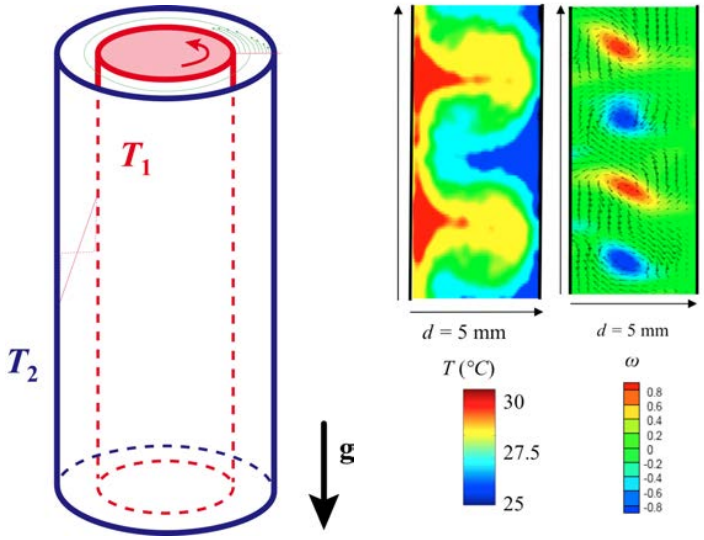

Figure 3.3: (Left) Schematic of the heated Taylor-Couette flow. Note the laminar and turbulent temperature profile on the left and the velocity profile on the top. (Right) An example of measurement of the temperature and vorticity field for $\eta = 0.8$, $\Gamma = 111.8$, $Re = 270$ and $Gr = 2400$ from Guillerm[23].

κ the thermal diffusivity in m^2/s. As we consider water as the working fluid, $Pr \cong 7$. The Grashof number can be defined as $Gr = (\tau_\nu/\tau_\alpha)^2 = g\alpha\Delta T d^3/\nu^2$ where $\tau_\alpha = \sqrt{d/g\alpha\Delta T}$ is the characteristic time related to buoyancy. The work of Lepiller *et al.*[21,22] and others[23,24,25] report the case a water in a vertical Taylor-Couette flow ($\eta = 0.8$, $\Gamma = 111.8$) with only the inner cylinder rotating and a radial temperature gradient. Hence, there are two forces acting on the system: the centrifugal force and the buoyancy force. The spatio-temporal dynamics of this thermo-hydrodynamic instability revealed the conditions for the formation of a propagating spirals, the properties of soliton solutions, the wavelength and the velocity of the vertically propagating patterns as well as the velocity field measured by PIV (Particle Image Velocimetry) and the temperature field measured using thermochromic liquid crystals. Figure 3.3 present a schematic of the problem and a temperature and vorticity field around a small number of vortices.

[21]Lepiller V, Prigent A, Dumouchel F and Mutabazi I. Transition to turbulence in a tall annulus submitted to a radial temperature gradient. *Phys. Fluids* 19:054101 (2007)

[22]Lepiller V, Goharzadeh, Prigent A, Mutabazi I. Weak temperature gradient effect on the stability of the circular Couette flow. *Eur. Phys. J. B* 61:445-455 (2007)

[23]Guillerm R. Etude expérimentale des instabilités thermo-hydrodynamiques dans un système de Couette-Taylor. *Thèse de doctorat, Université du Havre* (2010)

[24]Savaro C. Etude expérimentale de l'effet d'un gradient radial de température sur les instabilités du système de Couette-Taylor. *Thèse de doctorat, Université du Havre* (2014)

[25]Kang C, Yang KS, Mutabazi I. Thermal effect on large-aspect-ratio Couette-Taylor system: numerical simulations. *J. Fluid Mech.* 771:57-78 (2015)

At relatively large $Re \gtrsim 5000$, the flow pattern is dominated by turbulent Taylor vortices. It is sometimes useful to make the hypothesis of no density variation as the gravitational effects are small compared to the inertial effects ($Gr \ll Re^2$), then the buoyancy could be neglected. The turbulent flow may be divided into two regions, the inviscid region and the viscous dominated region near the wall. The boundary layer theory[26] predicts its thickness, $\delta/d \propto (Vd/\nu)^{-1/5}$, where V is the velocity at the boundary of the two regions.

The relevant parameter to quantify the temperature difference is the thermal Nusselt number, Nu_θ, that is defined at the inner and outer cylinder as:

$$Nu_{\theta_i} = \frac{d}{T_i - T_m}\left(\frac{\partial T}{\partial r}\right)_{r_i} \quad , \quad Nu_{\theta_o} = \frac{d}{T_o - T_m}\left(\frac{\partial T}{\partial r}\right)_{r_o},$$

where T_m is the mean temperature in the bulk. It is also possible to define an averaged $\overline{Nu_\theta}$ on each surfaces.

The intention of the heat transfer experiments is to measure temperature in order to obtain the Nu_θ and its scaling with Re. There are already several experimental results available for air, water or oil flow in horizontal configuration. An example of such correlation is presented in figure 3.4 from experiments on Tachibana and Fukui[27]. Recent velocity measurements using PIV by Aubert *et al.*[28] were able to estimate the Reynolds stress within the gap, the stresses related to turbulent motion, but most of them rely on a limited number of temperature point measurements.

Numerical modelling of the heat transfer in Taylor-Couette flow is now possible is a number of numerical approach as the Reynolds Stress Modelling[29] or direct numerical simulations. The experimental validation of specific cases and the use of numerical simulation should allow for a better understanding of the similarity solutions expressed in terms of scaling laws.

3.3 Taylor-Couette flow with complex fluids

Coming back to transitional flow and assuming that the first bifurcations for transition to turbulence are relatively well understood for single phase Taylor-Couette flow, we now turn to multiphase flows. First, we review some results for two-fluids Taylor-Couette flow, describe an intriguing problem from particle suspension flow with a interface and present some results for viscoelastic flow.

[26]Schlichting H, Gersten K. Boundary layer theory. *Springer* (2000)

[27]Tachibana F, Fukui S. Convection heat transfer for the rotational and axial flow between two concentric cylinders. *Jap. Soc. Mech. Eng.* 7(26)385-391 (1964)

[28]Aubert A, Poncet S, Le Gal P, Viazzo S, Le Bars M. Velocity and temperature measurements in a turbulent water-filled Taylor-Couette-Poiseuille system. *Int. J. Thermal Sci.* 90:238-247 (2015)

[29]Poncet S, Haddadi S, Viazzo S. Numerical modeling of fluid flow and heat transfer o, a narrow Taylor-Couette-Poiseuille system. *Int. J. Heat Fluid Flow* 32:128-144 (2011)

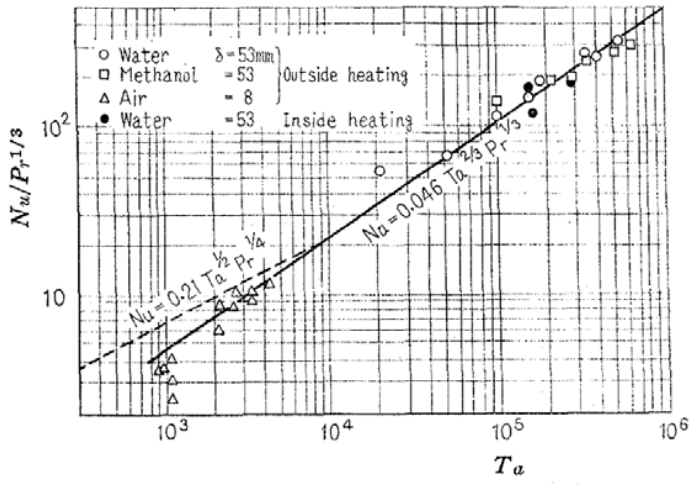

Figure 3.4: Heat transfer results for turbulent Taylor-Couette flow from Tachibana and Fukui[25] ($r_i = 15$ mm, $r_o = 68$ mm, $L = 250$ mm, so $d = 53$ mm, $\eta = 0.22$ and $\Gamma \simeq 4.72$). Ta, is defined as $Ta = (\Omega d r_i/\nu)\sqrt{d/r_i} = Re\sqrt{d/r_i} \simeq 0.365Re$.

3.3.1 Two-fluid Taylor-Couette flow

The flow of two immiscible fluids (usually oil and water) flow in Taylor-Couette is considered in a range of Reynolds numbers small or around the transition to Taylor vortices. The flow is characterised by the interface and the stability of the flow depends also on the stability of the interface. An extensive mathematical study of these flows have been presented in the book by Joseph and Renardy[30] and several experimental studies[31,32,33] reported the formation of the Taylor vortices in one fluid and deformation of the interface. The case of a vertical Couette-Taylor experiment with two newtonian fluids (glycerine solution and air) and an interface instability has been studied by Watanabe, Toya and Nakamura[34] and numerically by Wardle and Lee[35], as shown in figure 3.5 where interface waves are observed.

[30]Joseph DD, Renardy YY. Fundamentals of two-fluid dynamics. Part 1: Mathematical theory and applications. *Springer Science* (1984)

[31]Baier G, Graham MD. Two-fluid Taylor-Couette flow: experiments and linear theory for immiscible liquids between corotating cylinders. *Phys. Fluids* 10(12):3045-3055 (1998)

[32]Bonn D, Kobylko M, Bohn S, Meunier J, Morozov A, van Saarloos W. Rod-climbing effect in Newtonian fluids. *Phys. Rev. Lett.* 82:214503 (2004)

[33]Broadbent AL, Mullin JM, Codd SL, Dockery JD, Seymour JD. Pulsed gradient spin echo nuclear magnetic resonance measurement and simulation of two-fluid Taylor vortex flow in a vertically oriented Taylor–Couette device. *Appl. Magn. Reson.* 42:137 (2012)

[34]Watanabe T, Toya Y. Vertical Taylor-Couette flow with free surface at small aspect ratio. *Acta Mech.* 223(2) 347–353 (2012)

[35]Wardle KE, Lee T. Finite element lattice Boltzmann simulations of free surface flow in a concentric cylinder. *Comput. Math. Appl.* 65:230-238 (2013)

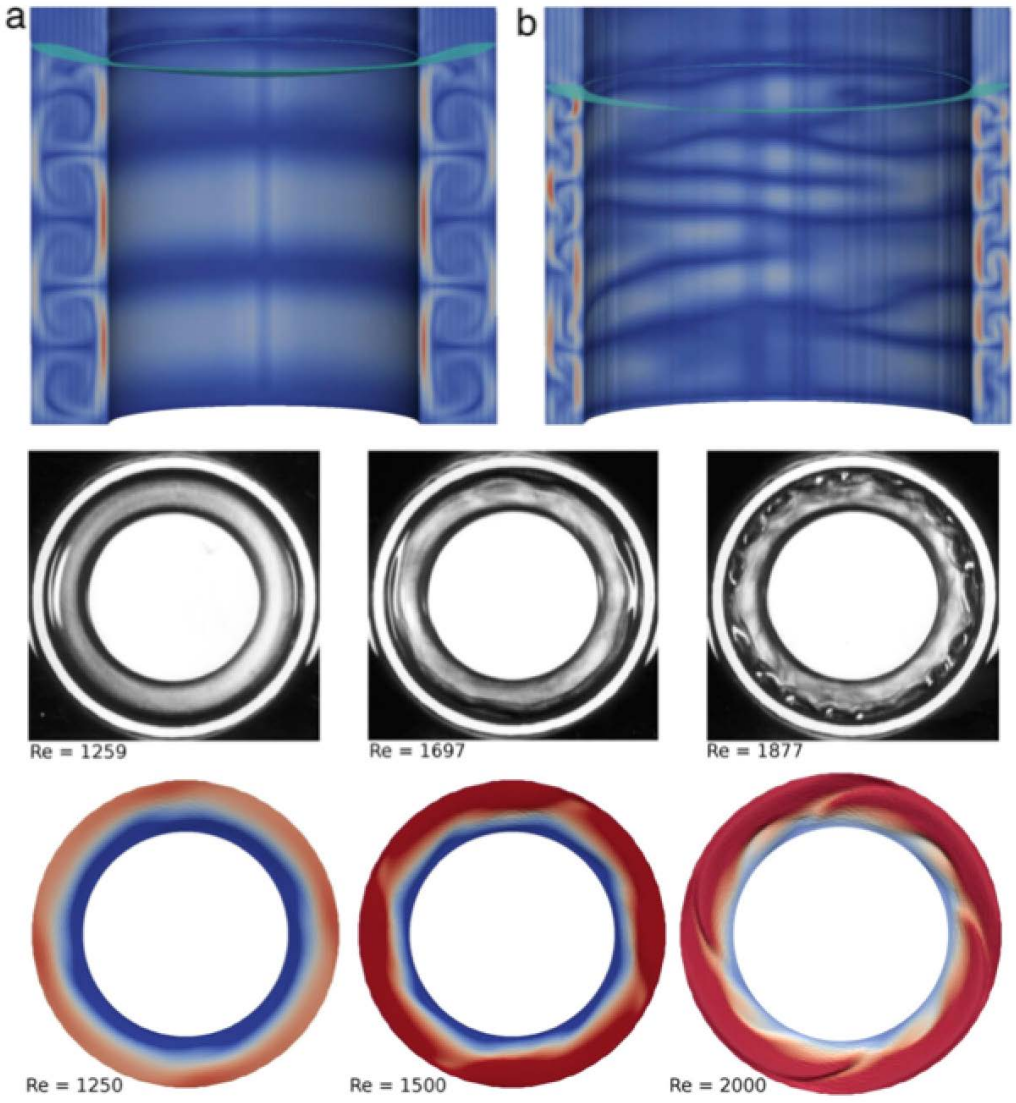

Figure 3.5: Two-fluid in vertical Taylor-Couette flow. (Top) Numerical simulation by Wardle and Lee[33] for (a) $\eta = 0.667$ and (b) 0.883 at $Re = 1500$, (middle) top view of the interface from the experiments of Watanabe and Toya[32] for $\eta = 2/3$, and (bottom) numerical simulation by Wardle and Lee[33] of the surface elevation for $Re = 1250$, 1500 and 2000.

We have studied the simple case of the flow between two concentric horizontal cylinder partially filled with viscous fluids. This flow is modelled using the Navier-Stokes equations including a surface tension term:

$$\rho\frac{\partial \mathbf{u}}{\partial t} + \rho\mathbf{u}\cdot\nabla\mathbf{u} = -\nabla P + \mu\nabla\cdot\mathbf{D} + \rho\mathbf{g} + G\nabla\phi \tag{3.2}$$

where $\mathbf{u}$ is the velocity (m/s), $\mathbf{D}$ is the strain rate tensor: $\mathbf{D} = \nabla\mathbf{u} + (\nabla\mathbf{u})^T$, ρ (kg/m^3) is the density, t is the time (s), P is the pressure (Pa), μ is the dynamic viscosity (Pa.s), $\mathbf{g}$ is the gravity, and the last term of equation (3.2) is the surface tension force where G is the chemical potential (J/m^3) and ϕ is the phase-field variable varying from -1 to 1.

The surface tension effect is obtained from the Cahn-Hilliard equation, given by:

$$\frac{\partial\phi}{\partial t} + \mathbf{u}\cdot\nabla\phi = \nabla\cdot\frac{\gamma\lambda}{\epsilon^2}\nabla\psi \tag{3.3}$$

$$\psi = -\nabla\cdot\epsilon^2\nabla\phi + \left(\phi^2 - 1\right)\phi + \frac{\epsilon^2}{\lambda}\frac{\partial f}{\partial\phi} \tag{3.4}$$

where γ is the mobility, λ is the mixing energy density (N), ϵ is the interface thickness parameter (m) and ψ is the phase-field help variable. Here γ is constant and equals 10 kg^{-1}.m^3.s. ϵ is also constant and equals 10^{-4} m. It is assumed further that the diffuse interface is at equilibrium and thus the ϕ-derivative of free energy is zero: $\partial f/\partial\phi = 0$. Furthermore, there is a relation[36] between λ, ϵ and the surface tension coefficient: $\sigma \propto \lambda/\epsilon$. G is the chemical potential (J/m^3): $G = \lambda\psi/\epsilon^2$.

We simulate the evolution of $\mathbf{u}$ and ϕ in time using a finite element code. A geometry with $\eta = 0.42$ and $\Gamma = 24.3$ is implemented in a two-dimensional cylindrical coordinate system. Equations (3.2-3.4) combined with the non-slip boundary condition at the outer cylinder and oil initially wetting the inner rotating cylinder are solved. In the calculation results presented here, the input parameters equal to the parameters stated in the experiment by Peixinho *et al.*[37]. The viscosity of the top fluid representing air is 1.73×10^{-5} Pa.s. In the case $F = 50\%$, the top fluid viscosity is 0.01 Pa.s for numerical convenience. The viscosity of the bottom fluid is 10 Pa.s. The calculations are unsteady and after sufficient time steps a steady solution is observed and presented in figure 3.6(*c, e* and *f*). Concerning the mesh, up to hundred thousands triangular elements have been used. Furthermore, a very fine mesh was used at the location of the cusp and the interface.

At high rotation, the interface deforms the subsurface flow now exhibits several recirculation regions. Between the recirculation regions, stagnation points and cusps form. The cusp eventually breaks up. The break up of the cusp and the interface is not well predicted because the singularity of the cusp that requires an high resolution of the mesh.

[36]Yue P, Feng JJ, Liu C, Shen J. A diffuse-interface method for simulating two-phase flows of complex fluids. *J. Fluid Mech.* 515:293-317 (2004)

[37]Peixinho J, Mirbod P, Morris JF. Free surface morphology in the flow between two horizontal concentric cylinders. *Eur. Phys. J.* E 35:19 (2012)

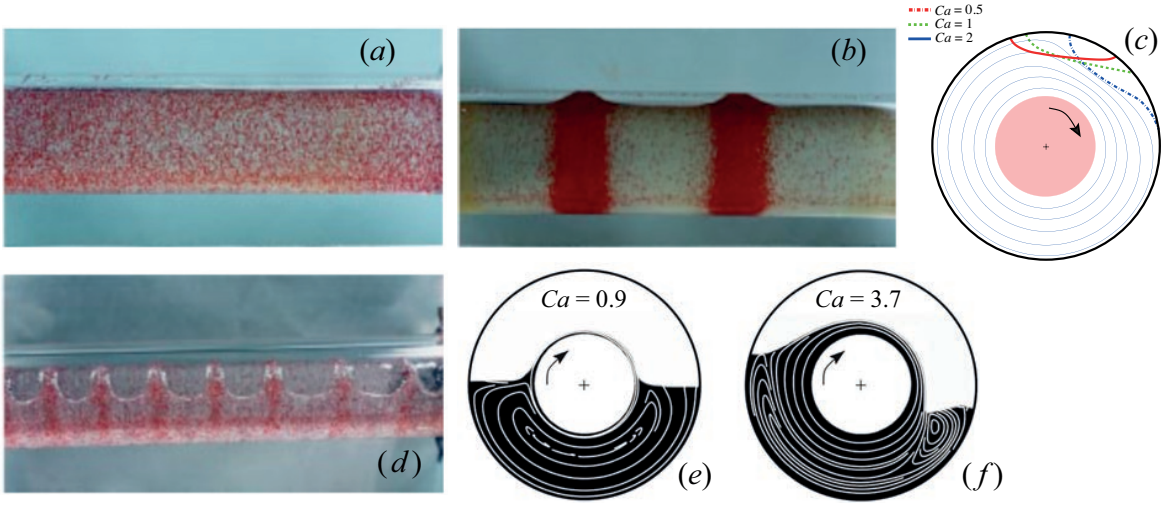

Figure 3.6: (*a*, *b* and *d*) Particle segregation in monodisperse sheared suspensions in a horizontal cell, images from experiments from Tirumkudulu *et al.*[46]. (*a*) Initial state: well mixed 10% suspension (red) at 95% fill level before shearing, (*b*) final state: after shearing at 9 rpm and (*d*) final state: 15% suspension at 50% fill level sheared at 6 rpm. (*c*, *e* and *f*) Fluid flow simulations of the partially filled cell using the mean field method showing flow cross-section and the interface deformation: (*c*) 90% fill level at $Ca = 0.5$, 1 and 2 (*e*) 50% fill level at $Ca = 0.9$ and (*f*) 3.7. Note the cusp formation.

3.3.2 Particle suspension and banding phenomena

Assuming the possibility of computing two-fluid flow, we now consider the horizontal two-fluid Taylor-Couette flow with the bottom fluid been a viscous suspension of small non-Brownian particles. Similar particle systems at intermediate Reynolds numbers can be found in many applications in material transport, waste, coating, printing, food and pharmaceutical processes, etc. Usually, particles in flows are modelled using suspension models[38,39,40,41] considering rigid particles considering infinitely deformable drops. In linear shear flows with no inertia, these models give information about the bulk viscosity. However, in more complex geometries and in transitional flows, very little is known.

The Taylor-Couette arrangement of horizontal concentric cylinders partially filled, presented in the previous section is now considered with particle suspension as a bottom fluid. It is of interest here because of the controllability of the underlying flow and the presence of an interface. Indeed, the cylinders rotation induces a flow which could deform the particles. In the following sections, the banding phenomena problem and the planned research on (i) complex fluids flow and (ii) transition to turbulence are presented. The flow geometry is an arrangement of horizontal concentric cylinders partially filled. It is sometimes called the Taylor-Dean system[42] because it is a combination of Taylor-Couette flow (flow between fully filled concentric cylinders) and Dean flow (flow in curved channel). There is a contrast with the Taylor-Couette system because the partial filling of the gap produces interfaces. The rotations of the cylinders drive fluid toward the interface. Hence a pressure gradient along the azimuthal direction is created. The flow profile in the bulk is a combination of a Couette flow due to the cylinder rotation and a Poiseuille flow due to the azimuthal pressure gradient.

The particle segregation or the banding phenomena observed by several independent investigations[43,44,45,46] is described. Suspension flow in a partially filled horizontal Couette cell system has attracted interest because of the appearance of a banding phenomenon; the concentration of solids is found to vary axially in alternating bands of high and low

[38]Leighton D, Acrivos A. The shear-induced migration of particles in concentrated suspension. *J. Fluid Mech.* 181:415-439 (1987)

[39]Philips RJ, Armstrong RC, Brown RA, Graham AL, Abbott JR. A constitutive for concentrated suspensions that accounts for shear-induced particle migration. *Phys. Fluids* A 4:30-40 (1992)

[40]Morris JF, Boulay F. Curvilinear flows of noncolloidal suspensions: the role of normal stresses. *J. Rheol.* 43(5) (1999)

[41]Miller M, Morris JF. Normal stress-driven migration and axial development in pressure-driven flow of a concentrated suspension. *J. Non-Newton. Fluid Mech.* 135:149-165 (2006)

[42]Mutabazi I, Hegseth JJ, Andereck CD, Wesfreid JE. Pattern formation in the flow between two horizontal coaxial cylinders with a partially filled gap. *Phys. Rev. A* 38(9):4752-4760 (1988)

[43]Karweit MJ, Corrsin S. Observation of cellular patterns in a partially filled, horizontal, rotating cylinder. *Phys. Fluids* 18(1):111-112 (1975)

[44]Timberlake BD, Morris JF. Film depth and concentration banding in free-surface Couette flow of a suspension. *Phil. Trans. R. Soc. A* 361(1806) 895-910 (2003)

[45]Joseph DD, Wang J, Bai R, Yang BH, Hu HH. Particle motion in a liquid film rimming inside of a partially filled rotating cylinder, *J. Fluid Mech.* 496:139-163 (2003)

[46]Guyez E, Thomas PJ. Spatiotemporal segregation-pattern drift in particles-laden rimming flows. *Phys. Rev. Lett.* 100:074501 (2008)

(even zero) concentration for values of the filling fraction from 50 to 95%. The Reynolds number in these flow experiments is less than 0.1. The photographs, presented in figure 3.6, are the sticking example from Tirumkudulu, Tripathi and Acrivos[47,48] and show the case of a 10% suspension where the cell is 95% filled and only the inner cylinder rotates at 9 rotations per minutes. Initially, the particles are well mixed, then after several rotations of the inner cylinder, whereas the outer cylinder is stationary, stable bands are observed. The mechanism for the banding process within the single cylinder has been argued to be a result of gravity driven flows along the axis, and a theory has been developed. This theory utilises understanding of the flow within the rotating cylinder, developed using a lubrication analysis. An argument for segregation into bands based on "differential drainage" resulting from axial flows has also been made. The previous theories[49,50] do not take into account the filling fraction. Yet, when the particles are neutrally buoyant, whereas no bands appear when the system is fully filled[51,52], the segregation is sharpest when the filling fraction is very close to 95% and then deteriorates, against all expectations, as the filling fraction decreases.

The system is partially filled and the flow can be simulated assuming two immiscible fluids where the top fluid is air and the bottom fluid is a viscous liquid. Hence the density and the viscosity differences are usually considered large. Modern numerical methods including level-set, phase field or lattice Boltzmann methods can predict fluid flow and interface deformation in two-fluid problems. The present configuration is "simple" since it is a closed system in contrast with open systems (pipe flow). Many ideas on interface modelling methods use specific methods developed in the 70's to deal with this difficulty and are today know as volume of fluid[53] or immersed boundary method. More modern methods like the phase field[54] method and the lattice Boltzman[51] method have emerged. Our work[37] uses the phase field method to calculate the morphology of the interface. Specifically, in a well-defined range of inner cylinder velocities, two large counter-rotating recirculations are observed. The figure 3.6(c, e and f) presents the deformation of the interface with different rotation speeds and fill levels. The simulations[37] reproduce well the deformation of the interface, the dimension of the recirculation regions and the film thickness. The present simulations are two-dimensional and an extension to three-dimensional

[47]Turumkudulu M, Tripathi A, Acrivos A. Particle segregation in monodisperse shear suspensions. *Phys. Fluids* 11(3):507-509 (1999)

[48]Turumkudulu M, Tripathi A, Acrivos A. Particle segregation in monodisperse shear suspension. *Phys. Fluids* 11(9):S13 (1999)

[49]Jin B and Acrivos A. Rimming flows with axially varying viscosity. *Phys. Fluids* 16(3):633-640 (2004)

[50]Jin B and Acrivos A. Theory of particle segregation in rimming flows of suspensions containing neutrally buoyant particles. *Phys. Fluids* 16(3):641-651 (2004)

[51]Lee T and Lin CI. A stable discretization of lattice Boltzmann equation for simulation of incompressible two-phase flows at high density ratio. *J. Comp. Phys.* 206:16-47 (2005)

[52]Seiden G, Ungarish M, Lipson SG. Banding of suspended particles in a rotating fluid-filled horizontal cylinder. *Phys. Rev. E* 72:021407 (2005)

[53]Gueyffier D, Li J, Nadim A, Scardovelli R, Zaleski S. Volume-of-fluid interface tracking with smoothed surface stress methods for three-dimensional flows. *J. Comp. Phys.* 152(2) 423-456 (1999)

[54]Tryggvason G, Burnner B, Esmaeeli A, Juric D, Al-Rawahu N, Tayber W, Han J, Nas S, Jan YJ. A front-tracking method for the computations of multiphase flow. *J. Comp. Phys.* 169(2):708-759 (2001)

in spherical coordinates will be considered in order to develop bioreactors.

3.3.3 Viscoelastic fluids

Solutions of polymer diluted in a solvent can lead to viscoelastic fluids. Specifically, long linear polymer chains such as polyethylene oxide (PEO) of high molecular weight are known to exhibit viscoelastic properties[55]. The initial experiments were concerned with torque measurement in order to extract viscometric properties of the fluids. Then the stability issue was reported by Denn and Roisman[56] and Groisman and Steinberg[57]. They reported a large torque increase and hysteretic behaviour.

In our recent work, we have found that for dilute concentrations, the critical mode is the stationary and axisymmetric Taylor vortex flow, which bifurcates to time periodic wavy vortex flow for higher shear rate. The oscillation amplitude of wavy vortex flow decreased with the increasing shear rate. For semi-dilute solutions, the critical mode occurs in the form of standing waves, the frequency of which decreases with the shear rate. We also found hysteresic behaviour. Most important is the large torque or drag enhancement at rotation rates slightly above transition. Discussion of polymer degradation and turbulent drag reduction[58,59] and drag enhancement[60] mechanism are needed.

3.4 Future perspectives

The presentation of the previous works leads us to continue the research in Taylor-Couette flow in two different directions: (i) turbulent isothermal and heat Taylor-Couette flow and (ii) transitional viscoelastic Taylor-Couette flow.

3.4.1 Turbulent isothermal and heated Taylor-Couette flow

Studies on turbulent Taylor-Couette flow, multiple states and torque measurements are carried out within the *thèse de doctorat* of Borja Martínez-Arias (September 2012 - September 2015). The experimental finding should be recovered using numerical sim-

[55]Crumeyrolle O, Mutabazi I, Grisel M. Experimental study of inertioelastic Couette-Taylor instability modes in dilute and semidilute polymer solutions. *Phys. Fluids* 14(5)1681-1688 (2002)

[56]Denn M and Roisman J. Rotational stability and measurement of normal stress functions in dilute polymer solutions. *AIChE J.* 15:454-459 (1969)

[57]Groisman A and Steinberg V. Elastic turbulence in curvilinear flows of polymer solutions. *New J. Phys.* 6:29 (2004)

[58]Pereira AS and Soares EJ. Polymer degradation of dilute solutions in drag reduction flows in a cylindrical double gap rheometer device. *J. Non-Newton. Fluid Mech.* 179:9-22 (2012)

[59]Pereira AS, Andrade RM, Soares EJ. Drag reduction induced by flexible and rigid molecules in a turbulent flow into a rotating cylindrical double gap device: comparison between poly(ethylene oxide), polyacrylamide and xanthan gum. *J. Non-Newton. Fluid Mech.* 202:72-87 (2013)

[60]Andrade RM, Pereira AS, Soares EJ. Drag increase at the very start of drag reducing flows in a rotating cylindrical double gap device. *J. Non-Newton. Fluid Mech.* 212:73-79 (2014)

ulations and a collaboration is started to use the YALES2 code with Luminita Danaila and Vincent Moureau (CORIA, Rouen).

In the short term, the torque and visualisation data should be complemented with pressure measurements and velocity measurements. In the range of relatively small Re and specifically for the case $\eta = 0.6$, the Taylor vortex flow regime is large in Re, so there is an opportunity to study the transition through wave-vortex interaction. Also, the presence of small wavelength Görtler vortices has been reported and may explain the different slopes observed in the Nu_ω versus Re curve.

For the range of large Re, there will be the possibility to perform laser Doppler velocimetry and particle image velocimetry to obtain statistics of the turbulent flow: mean velocity profiles, Reynolds stresses, turbulent kinetic energy production and dissipation rates. Although turbulent structure function have been obtained before[13,19] only for $\eta \simeq 0.7$, measuring it for our systems ($\eta = 0.6$ and 0.9) could lead to discrepancies.

Concerning the highly heated and highly turbulent Taylor-Couette flow, a new facility (DIAMECO) will be available in the near future. It will be the chance to measure scaling laws for the heat transfer in heated turbulent flow up to $Re = O(10^6)$ and $Gr = O(10^5)$. There will be also the possibility to measure flow fields and temperature fields. If statistical properties of the turbulent fields are accessible, the assumption of passive scalar will be tested through correlation coefficients and probability density functions to assess the local isotropy[61] in a wide range of Re.

3.4.2 Viscoelastic Taylor-Couette flow

As explained before, the Taylor-Couette flow is the ideal system to study polymer flow in order to study the drag enhancement and reduction phenomena. The phenomena can be quantified using torque measurements. A possible extension of the results of Borja Martínez-Arias is the use of PIV to quantify the viscoelastic turbulence. More experiments could be performed using different polymer properties (flexible, rigid, long, short polymers) in order to quantify further the drag reduction phenomena.

3.4.3 Multiphase Taylor-Couette flow

Concerning the multiphase Taylor-Couette flow, it is planed to carry out more experiment on the two-fluid Taylor-Couette flow and quantify the interface break-up velocity as a function of the difference parameters of the flow. In the long term, our goal is to develop prediction tools for particle segregation and mixing in a partially filled system. This modelling should predict the degree of mixing and the kinetics. A first route is to couple the interface modelling presented here with the suspension model proposed by Morris and Boulay[40] and Miller and Morris[41].

To summarise, below is a list of prospects:

[61] Danaila L, Le Gal P, Anselmet F. Some new features of the passive scalar mixing in a turbulent flow. *Phys. Fluids* 11(5):636-646 (1999)

- *Thèse de doctorat* of Borja Martínez-Arias (September 2012 - September 2015)
- DIAMECO project (DIAgnostic Multi-échelles des systèmes Energétiques COmplexes) for turbulent heated Taylor-Couette flow

Chapter 4

Instabilities of a spherical gel

As seen before, the addition of polymers to a fluid can modify the transition to turbulence in a drastic way. Studying transitions with viscoelastic and yield stress fluids gave us the opportunity to use polymer fluids. Here, some experiments about gels are presented. Gels are elastic model material for porous materials. The gels used here are initially spherical and can be deformed, swollen, dried and compressed or compacted. These transformations can induce surface patterns. The swelling of a single sphere is considered and the main advantage of using a sphere is the possibility of simplifying the problem to one or two dimensions. There are several possible models for the patterns on the surface of a swelling sphere using: (i) reaction-diffusion equation, (ii) linear poroelastic and (iii) nonlinear poroelastic ideas. These models have limitations when trying to compare to experiments.

Publication associated with this chapter
- Shomeek Mukhopadhyay and Jorge Peixinho. Packings of deformable spheres. *Phys. Rev. E* 84:011302 (2011)

4.1 Introduction

Gels are surprising materials: they are mostly made of liquid, but resist to flow. Gels can be found in foodstuffs, but also in cosmetics, contact lenses, drug delivery, etc. Yet there is a large variety of gels. One can define two main types of gels depending on the cross-linking strength. Basically, the weak gels are unable to support themselves and strong gels retain their shape. Usually strong gels are chemical gels based on strong covalent cross-linking of polymer chains and weak gels are called "physical gels" because of their weak hydrogen bonding, hydrophobic association or ion-mediated cross-linking[1]. The polyacrylamide gels used here are classified as strong gels. There are also many surprising phenomena, for example their yield stress behaviour or their mechanical instabilities of buckling during swelling or drying that are observed everyday and remain unexplained.

[1]Williams PA. Handbook of industrial water soluble polymers. *Blackwell Publishing* (2007)

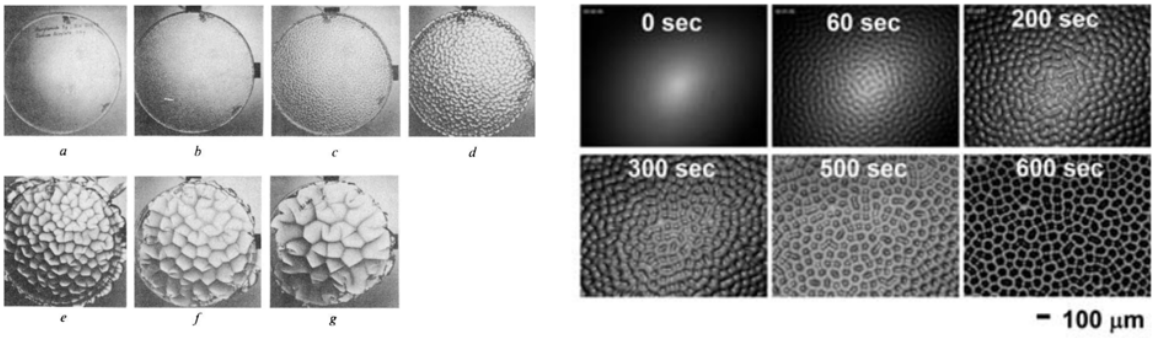

Figure 4.1: Snapshots of the time evolution of a thin layer of (left) ionised acrylamide gel in a Petri-dish swelling in water by Tanaka *et al.*[8] ($a \to g$) and (right) using PHEMA cross-linked with 2% EGDMA (dry thickness 60 microns) by Guvendiren *et al.*[11].

Understanding these gels phenomena could help us to model fruit growth[2,3,4], the shape of embryos, the morphology of planets, the production of pharmaceutics, the evolution of tumours[5,6] or brain developments[7].

Most of the previous works on pattern transformation in swelling gels by elastic instability concentrated on films that absorb water[5,8,9,10]. Examples of snapshots of the swelling of thin layers of ionised acrylamide gel in a Petri-dish swelling in water by Tanaka *et al.*[8] is given in figure 4.1. Recent experiments using poly(2-hydroxyethyl methacrylate) (PHEMA) cross-linked with different concentrations of ethylene glycol dimethacrylate (EGDMA) by Guvendiren *et al.*[11] have shown that the emergence of the different patterns and the wavelength depends on the cross-linker concentration (see figure 4.1).

Matsuo and Tanaka[12] first observed these as transient patterns of the surface of the

[2]Yin J, Cao Z, Li C, Sheinman I, Chen A. Stess-driven buckling patterns in spheroidal core/shell structures. *PNAS* 105:19132-19135 (2008)

[3]Li B, Jia F, Cao YP, Feng XQ, Gao H. Surface wrinkling patterns on a core-shell soft sphere. *Phys. Rev. Lett.* 106:234301 (2011)

[4]Li B, Cao YP, Feng XQ, Gao H. Mechanics of morphological instabilities and surface wrinkling in soft materials: a review. *Soft Matter* 8:5728 (2012)

[5]Dervaux J, Couder Y, Guedeau-Boudeville MA, Ben Amar M. Shape transition in artificial tumors: from smooth buckles to singular creases. *Phys. Rev. Lett.* 107:18103 (20011)

[6]Ciarletta P. Buckling instability in growing tumor spheroids. *Phys. Rev. Lett.* 110:158102 (2013)

[7]Tallinen T, Chung JY, Biggins JS, Mahadevan L. Gyrification from constrained cortical expansion. *Proc. Natl. Acad. Sci. USA* 111(35)12667-12672 (2014)

[8]Tanaka T, Sun ST, Hirokawa Y, Takayama S, Kucera J, Hirose Y, Amiya T. Mechanical instability of gels at the phase transition. *Nature* 325:796-8 (1987)

[9]Boudaoud A and Chaieb S. Mechanical phase diagram of shrinking cylindrical gels. *Phys. Rev. E* 68:021801 (2003)

[10]Mora T and Boudaoud A. Buckling of swelling gels. *Eur. Phys. J. E* 20:119-124 (2006)

[11]Guvendiren M, Burdick JA, Yang S. Kinetic study of swelling-induced surface pattern formation and ordering in hydrogel films with depth-wise crosslinking gradient. *Soft Matter* 6:2044-2049 (2010)

[12]Matsuo ES and Tanaka T. Kinetics of discontinuous volume-change transition of gels. *J. Chem. Phys.* 89:1695 (1988)

gel when the immersed sphere are submitted to temperature increase. Their study concentrated in kinetics, temperature effect and gel radius. There is numerous theoretical/numerical studies in spherical systems but few quantitative experiments. A recent experiment[13], using nuclear magnetic resonance (NMR), revisited the subject and their measurements of a rigid core region now support the core-shell model. That is the surface swells more than the interior resulting in instability patterns. Our contribution consists in new measurements and discussion of the poroelastic and core-shell model.

There are several ways to model swelling polymeric gels: (i) the reaction-diffusion models, (ii) the linear poroelastic models that the take into account the fluid displacement in the material and (iii) the nonlinear poroelastic models that take into account mixture properties of the materials. The reaction-diffusion models aim at reproducing swelling patterns, whereas the poroelastic models aim at predicting the stresses in the material. These models briefly recalled before describing the swelling and drying experiments.

4.1.1 Reaction-diffusion models

When a sphere of hydrophilic polymer is immersed in water, it experiences a volume phase transition. The water diffuses into the sphere and the polymer reacts. A first type of model for reaction-diffusion phenomena can lead to pattern formations. It was proposed by Turing and others[14,15] who found different patterns when solving a reaction-diffusion system on the surface of a sphere. The reaction-diffusion equation is:

$$\frac{\partial \boldsymbol{q}}{\partial t} = \boldsymbol{D}\nabla^2 \boldsymbol{q} + \boldsymbol{R}(\boldsymbol{q}), \tag{4.1}$$

where each component of the vector $\boldsymbol{q}(\boldsymbol{x}, t)$ represents the concentration of one substance, $\boldsymbol{D}$ is a diagonal matrix of diffusion coefficients, and $\boldsymbol{R}$ accounts for all local reactions. In its one-component version and if the reaction term vanishes, the reaction-diffusion equation represents a pure diffusion process.

In the context of the swelling hydrogels, $\boldsymbol{q}(\boldsymbol{x}, t)$ could be the water concentration in the gel and $\boldsymbol{R}$ could account for the polymer reaction to the imbibition or evaporation of the solvant.

4.1.2 Linear poroelastic models

A poroelastic material can imbibe solvent and swell. Radial and azimuthal stresses will develop when the material swells. For a homogeneous poroelastic material, in equilibrium state, the swelling ratio is uniform and the stress in the material is zero. In transient

[13]Barros A, de Azevedo EN, Engelsberg M. Surface pattern formation in a swelling gel. *Soft Matter* 8:8511 (2012)

[14]Turing AM. The chemical basis of morphogenesis. *Phil. Trans. R. Soc. Lond. B* 237:37 (1952)

[15]Plaza RG, Sánchez-Garduño F, Dadilla P, Barrio RA, Maini PK. The effect of growth and curvature on pattern formation. *J. Dyn. Diff. Equat.* 16(4):1093-1121 (2004)

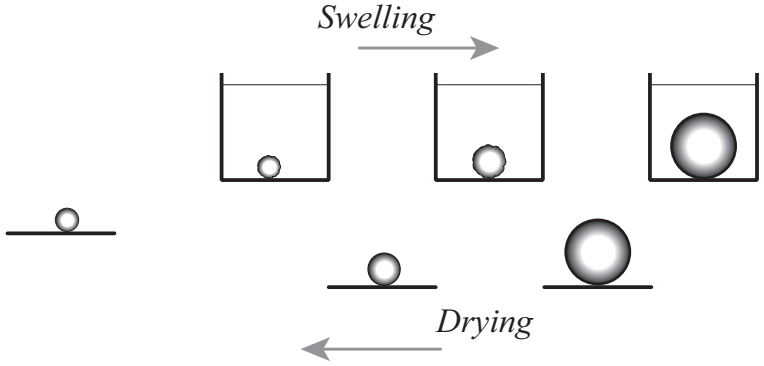

Figure 4.2: A spherical dried gel is transferred into water, in which it swells until equilibrium. When place in a watch glass, water evaporates from the gel until complete drying.

state, however, due to the inhomogeneous swelling, the stresses are finite in the material and can trigger mechanical instabilities[12,16].

A variety of instability patterns, induced by the transient stress field in a poroelastic material, have been observed in experiments[17]. The instability patterns usually disappear when the porous material reaches equilibrium state or when the material is cut so that the stresses are released. Figures 4.2 and 4.3 show schematics and snapshots of an example of the swelling process of a spherical gel. Water molecules can migrate into the gel through the surface and cause swelling. In the transient state, the surface swells more than the interior, resulting in instability patterns. As water migrates within the sphere, the surface pattern coarsens and eventually disappears.

The Biot's poroelasticity theory[18] allows to calculate how stress fields evolve with time in a poroelastic material. By perturbing the transient deformation field a sphere, it may be possible to deduce the critical conditions of wrinkling instability in the sphere from the computed stresses. Ignoring the influence of the wrinkled morphology of the sphere on the process of the diffusion of water, it is also possible to determine the time for the disappearance of wrinkles in the sphere[16].

Let's consider a poroelastic sphere with radius, R, sketched in figure 4.2. In the initial state, the poroelastic sphere is taken to be homogeneous and stress free, c_0 is the concentration of solvent (water) in the sphere (*i.e.*, the number of solvent molecules per unit volume of the material) and μ_0 being the chemical potential of the solvent in the polymer. The poroelastic sphere is then submerged into a solvent-containing environment with chemical potential μ_f. If $\mu_f > \mu_0$, the solvent migrates into the material and the material swells. If $\mu_f < \mu_0$, solvent leaves the material and the material dries and shrinks.

It is assumed the solvent can only migrate into the sphere through its surface. Before

[16]Li K, Ding K, Cai S. Diffusion-induced wrinkling instability in a circular poroelastic plate. *Appl. Phys. Lett.* 102:241908 (2013)

[17]Stoop N, Lagrange R, Terwagne, Reis PM, Dunkel J. Curvature-induced symmetry breaking determines elastic surface patterns. *Nat. Mat.* 14:337-342 (2015)

[18]Biot MA. General theory of three-dimensional consolidation. *J. Appl. Phys.* 12:155 (1941)

the instability happens, the deformation of the poroelastic sphere is axisymmetric and time dependent. Therefore, the displacement in radial direction is $u_r = u_r(r,t)$, the displacement in other directions are $u_\theta = u_\theta(r,t)$ and $u_\phi = u_\phi(r,t)$ are zero: $u_\theta = u_\phi = 0$. By adopting small deformation assumption and the approximation $u_\theta = u_\phi = 0$, one can obtain the strain field in the sphere:

$$\varepsilon_r(r,t) = \frac{\partial u_r(r,t)}{\partial r}, \quad \varepsilon_\theta(r,t) = \frac{u_r(r,t)}{r}, \quad \varepsilon_\phi(r,t) = \frac{u_r(r,t)}{r}. \tag{4.2}$$

The concentration of the solvent in the poroelastic plate is also a time dependent field, $c(r,t)$. The number of solvent molecules is conserved, so that

$$\frac{\partial c}{\partial t} + \frac{\partial (rF_s)}{r\partial r} = 0 \tag{4.3}$$

where F_s is the inward flux of solvent in the radial direction.

It is also assumed that the poroelastic sphere is in mechanical equilibrium in the process of solvent migration, so that stress field satisfies:

$$\frac{\partial \sigma_r}{\partial r} + \frac{\sigma_r - \sigma_\theta}{r} = 0, \tag{4.4}$$

where σ_r is the radial stress and σ_θ the ortho-radial stress.

Clearly the poroelastic sphere in not in diffusive equilibrium, so that the chemical potential of the solvent in the gel is time dependent: $\mu_f = \mu_f(r,t)$. The migration of the solvant in the gel is assumed to follow Darcy's law:

$$F_s = -\left(\frac{\kappa}{\eta\Omega^2}\right)\frac{\partial \mu_f}{\partial r} \tag{4.5}$$

where κ is the permeability of the poroelastic material, η the viscosity of the solvent, and Ω the volume per solvent molecule. The increase in the volume of the poroelastic material is entirely due to the additional solvent molecules absorbed:

$$\epsilon_r + \epsilon_\theta + \epsilon_\phi = \Omega(c - c_0). \tag{4.6}$$

In addition to these basic principles, an equation of state of the poroelastic material relating the stress and the displacement is needed. It introduces, the instantaneous shear modulus of the poroelastic material, the Poisson's ratio of the poroelastic material in equilibrium state, and the quantity $(\mu_f - \mu_0)/\Omega$ as the pore pressure.

As the solvent migrates into or out of the sphere, the concentration and the stress varies along the radial direction. A combination of all the above equations gives the two controlling equations in terms of the radial displacement $u_r(r,t)$ and the solvent concentration $c(r,t)$:

$$\frac{\partial c}{\partial t} = \frac{D}{r}\frac{\partial}{\partial r}\left(\frac{r\partial r}{\partial r}\right), \tag{4.7}$$

$$2\frac{\partial}{\partial r}\left[\frac{\partial\left(ru_r\right)}{r\partial r}\right]=\Omega\frac{\partial c}{\partial r}, \tag{4.8}$$

where $D = G\kappa/(1-2\nu)\eta$. These last two equations could be solved numerically, with the boundary conditions, $\mu_f(R,t) = \mu_f$, $\sigma_r(R,T) = 0$ and $u_r(0,t) = 0$. The initial conditions are: $c(r,0) = c_0$, $\mu(r,0) = \mu_f$ and $u_r(r,0) = 0$. In this model, the controlling equation and the quantity $\mu - \mu_0$ is the forcing parameter, which is difficult to measure experimentally. Depending on the chemical potential difference of the solvent in the environment and in the poroelastic plate at the initial state, wrinkling instabilities of different modes may be triggered by the transient stress field. These poroelastic models predict the network stress and the pore pressure (conditions for wrinkling), the migration of solvent, the different modes of deformation and the onset on wrinkling[16]. Note that both the initial and boundary conditions are linear with $\mu_f - \mu_0$, the only driving parameter. Hence the stress, the strain and the concentration depend linearly on the chemical potential.

4.1.3 Nonlinear poroelastic models

The approach described above (linear poroelasticity) may not be applicable when the strains are large, as in the case of super-absorbent polymers. What is missing is the mixture thermodynamics and basic properties of the polymer network. The mixing enthalpy parameter χ of the Florry-Huggins theory and the effective number of polymer chains per unit volume of the dry polymer[19]. The mean field theory of Gibbs free energy, ΔG, contains contribution from the mixing enthalty. Basically, these models inspired from Flory-Rehner[20] indicate the Helmholtz free energy is composed of two terms:

$$W = W_{Stretch}(\lambda_1, \lambda_2, \lambda_3) + W_{mix}(J) \tag{4.9}$$

where $W_{Stretch}$ comes from the fact that when stretching the polymer network, chains tend to have a end-to-end distance different than when the polymer is unstretched (in that case, end-to-end distance is gaussian distributed and depends on temperature), this has an energy cost. W_{mix} comes from the fact that there is an energy cost to have solvent molecules next to polymer molecules instead of other solvent molecules. λ_1, λ_2 and λ_3 are the principal stretches, $J = \lambda_1\lambda_2\lambda_3$ the swelling ratio, *i.e.* the ratio of the wet gel to the volume of the dry network (here $J \approx 500$). The stresses are obtained using:

$$\sigma_i = \frac{\lambda_i}{J}\frac{\partial W}{\partial \lambda_i} \tag{4.10}$$

Hence the total stress has two components (i) a stretching term and (ii) a fluid-pore pressure, p. Also the chemical potential has two terms: $\mu_f = p - \Pi_{mix}$, where Π_{mix} is the osmotic pressure.

[19]Engelsberg M and Barros WJ. Free-evolution in a high swelling polymeric hydrogel. *Phys. Rev. E* 88:062602 (2013)

[20]Flory PJ and Rehner JJ. Statistical mechanics of cross-linked polymer networks. *J. Chem. Phys.* 11(11) 521-526 (1943)

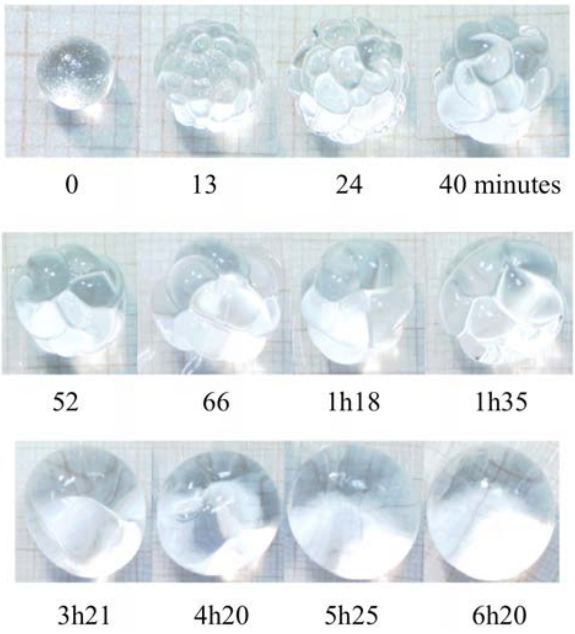

Figure 4.3: Photographs of the swelling of a spherical gel. At $t = 0$, the sphere is dry and has a diameter of 3 mm. The sphere is then immersed in water and every few minutes it is take out and pictured. The swelling time is indicated below the photographs. The whole experiment is conducted at $T = 22 \pm 1°C$.

It is important to note that all possible models indicate that the swelling and the drying are two different boundary condition that can be expressed as: $\sigma_r(R) = 0$ and $\mu_f(R) = \mu_{H_2O}$ for swelling and $\mu_f(R) = \mu^*$. For the drying condition, μ^* depend on the evaporation rate will be limited by the humidity rate in the room.

4.2 Swelling experiments

Dried polyacrylamide polymer spheres were obtained from Educational Innovations^{TM}. The initial diameter of the dry beads used here is 3.2±0.5 mm. A schematic of the swelling and drying experiments is presented in figure 4.1. Initially, the dry polymer sphere is immersed in mineral water (Volvic^{TM}), which pH is 7. A $t = 0$, the polymer sphere is gently immersed.

At the beginning the sphere surface is fine having a texture similar to frosted glass (see the first photograph of figure 4.2). Once the bead is immersed, wrinkle patterns are observed. Then hexagonal or circular lobes appear and seem to merge. The swelling process is not homogeneous as lines between the lobes are due to local shrinking of the gel. A layer at the interface is under a mechanical constraint as the outer surface of the layer is free to expand, whereas the inner surface is fixed to the core of the sphere. Thus the layer is under opposing demands on the upper surfaces, one to expand and the other

to remain partially rigid. Initially, these opposing forces are resolved by stretching the gel unidirectionally perpendicular to the surface. When the osmotic pressure is large the outer surface is forced to buckle. The characteristic wavelength of the pattern must be proportional to the thickness of the swollen layer, as that is the only relevant length scale. As time goes on, the thickness of the swollen layer increases, as does the wavelength of the pattern.

The complete swelling duration until reaching swelled equilibrium can take more than ten hours and can vary significantly for different beads of different diameters. During this period, the mass and volume of the sphere increases roughly linearly. The swelling is a multistage process. First, a modification of the polymer surface corresponding to penetration of water molecules into the polymer. The wetting of the shell of the polymer sphere is related to a slight expansion. During this stage, it is supposed that the core remains rigid[21]. Second, the roughness on the sphere surface appears as regularly spaced hexagonal lobes. Third, random oriented folds or wrinkles appear on the surface. Such pattern was previously observed in prior experiments on films[22,23]. As time proceeds, the number and deepness of the wrinkles slowly decrease. Finally, the sphere becomes smooth, well rounded and continues to growth for several hours until reaching the final diameter.

Using millimetre paper and an imaging software (ImageJ), a measure of the diameters was obtained. The evolution of the diameter is presented in figure 4.4. The experiment is as follow: at $t = 0$, the dry polymer sphere of diameter d_0 is immersed in demineralised water, then at given time the polymer sphere is rapidly taken out using a spoon and weighed, pictured and immersed again. All the experiments were conducted at room temperature. It was found that the growth of the diameter taking place during the firsts hours scales roughly as $d/d_0 \propto t^{0.5}$ indicating a diffusion process[24]. A zoom on the time evolution of the mean diameter is presented in the inset of figure 4.4 where the error bars represent the dispersion from three experiments. Three stages can be distinguished during the swelling process. First a dry layer of the polymeric sphere gets in contact with water and becomes wet. As soon as the polymer is completely wet, water diffuses into the hydrogel. This is in agreement with the results presented in the inset of figure 4.4 were the diameter evolves as $t^{0.5}$. At later times, the swelling is well described by an exponential fit. This suggests that the material is relaxing due to viscoelasticity.

[21]Tomari T and Doi M. Hysteresis and incubation in the dynamics of volume transition of spherical gels. *Macromolecules* 28:8334-8343 (1995)

[22]Trujillo V, Kim J and Hayward RC. Creasing instability of surface attached hydrogels. *Soft Matter* 4:564 (2008)

[23]Sultan E and Boudaoud A. The buckling of a swollen thin gel layer bound to a compliant substrate. *J. Applied Mech.* 75:051002 (2008)

[24]Cabane B and Hénon S. *Liquides - solutions, dispersions, emulsions, gels.* Editions Belin (2007)

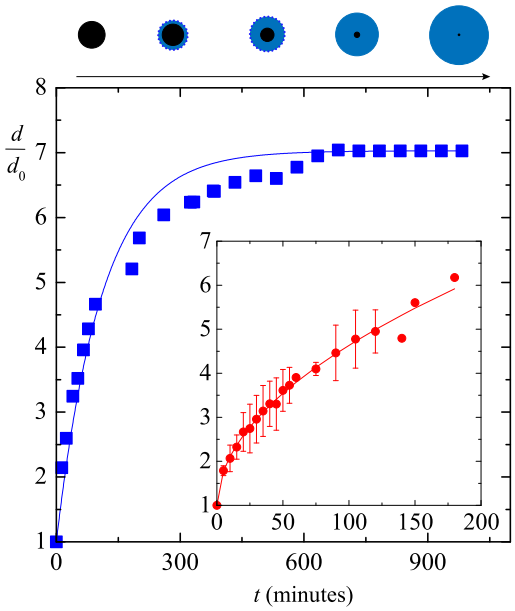

Figure 4.4: Time evolution of the diameter of a spherical gel immersed in water. The blue line represents an exponential fit. The inset is a zoom during the lobed sphere regime where the red line represents a power law fit: $d/d_0 \propto t^{0.5}$, where d_0 is the initial dry bead diameter. The error bars represent the dispersion from three experiments.

4.3 Surface pattern analysis

The patterns observed on the growing sphere surface are due to the elastic properties of the material. Indeed, when a wrinkled sphere is cut with a sharp-edged tool (*e.g.* a razor), the wrinkles instantaneously bounce back and disappears. During the growth of the sphere, two patterns can be distinguished: first regular lobed pattern and then elongated lobe pattern as a results of lobes that merged in a complicated way. The patterns can be described using the number of lobes as reported in figure 4.5. The number of lobes decreases rapidly during the first hour of growth. Then a small number of lobes remains for about one hour before they disappear. Simultaneously, the height of the lobes increases in the first hour and then remain constant. These patterns are observed together with a continuous increase of the diameter of the sphere and change in the properties of the material.

It has been suggested that the different patterns correspond to changes in properties of the sphere, *e.g.*, the ratio of modulus ratio between the shell and the core of the sphere. Yin *et al.*[2], Li *et al.*[3] and Ciarletta[6] computed the elastic deformations of a layer of elastic material glued upon a more rigid core and found that the wavelength of the pattern on the sphere is very sensitive to the elasticity ratio between the two materials and the thickness ratio between the shell and the core. The elastic modulus obtained from compression tests using the Hooke's law indicate that the dry polymer has an elastic modulus of $\sim$ 100 MPa,

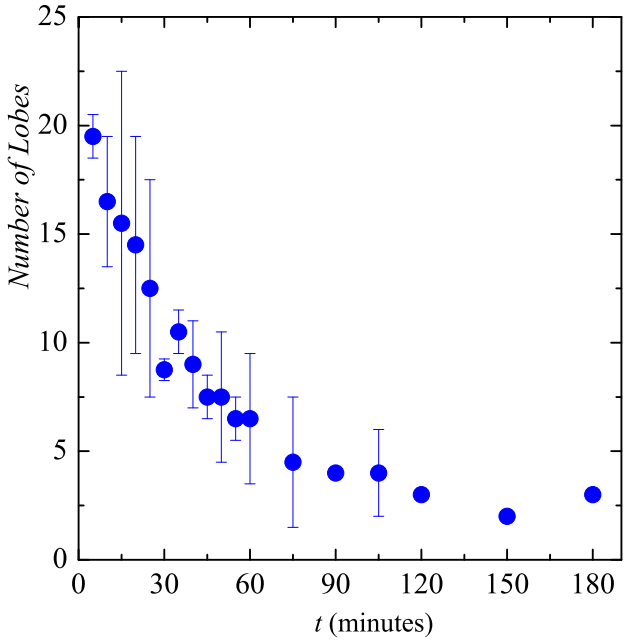

Figure 4.5: Evolution of the number of lobes on the surface of the swelling sphere as a function of time. The error bars represent the dispersion from three experiments.

whereas the wet spheres have a modulus of $\sim$ 10 kPa. So, the modulus ration between the core and the shell is of the order 10^3, much larger than any steady state calculations[2]. However there is no well defined shell thickness, that is to say that the shell and the core are not two distinct materials.

One can get a first evidence of a rigid core from cutting the sphere during the swelling process using a razor. Also, Barros *et al.*[13] used NMR technique to monitor the spin relaxation rate of water molecules to observed their motion in a swelling gel. They found that a rigid core can be observed and its thickness is proportional to the wavelength of the swelling pattern. Figure 4.6 presents our measurements for the relation between the wavelength of the lobed pattern as a function of the translucent shell thickness. As observed before on a similar spherical gel, it is found that there is a linear relationship between although lobes are present.

Direct observations of the sphere is very difficult because more than 99% of the swelled sphere is made of water so its refractive index is very similar to that of water. Here we used a shadowgraph technique using a (1 Watt) LASER source of 532 nm. We take advantage of the collimated laser light to observe small refractive index changes. A schematic of the setup is shown in figure 4.7 together with examples of pictures thresholded in light intensity in order to extract the position of the core/shell interface. Clearly the core diameter is initially of the same diameter than the dry bead. As the swelling takes place, the core also growth and then shrinks. The interface position that is detected through this method is only qualitative but corresponds to a region of poroelastic material where

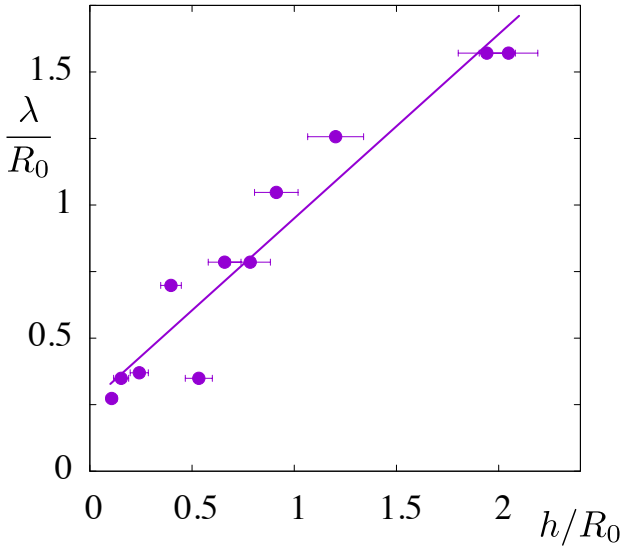

Figure 4.6: The wavelength of the pattern normalised by the initial particle radius with respect to the shell thickness also normalised by the initial particle radius.

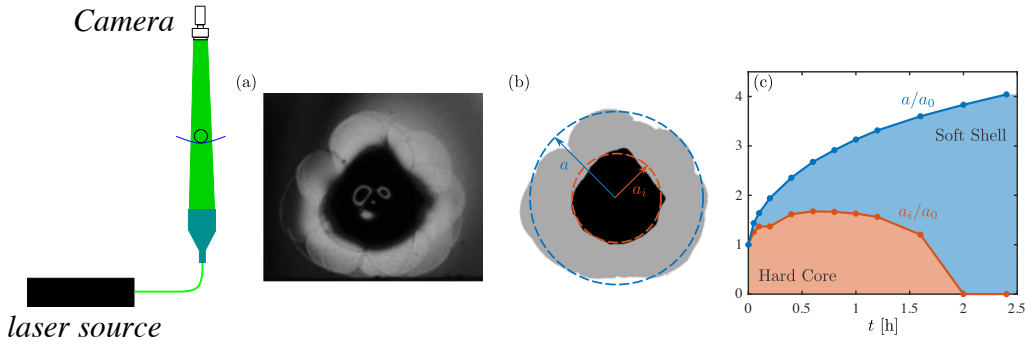

Figure 4.7: (a) Schematic of the shadowgraph experiment and photograph from the shadowgraph experiments. (b) Thresholded image revealing two distinct regions in the internal structure: A dark, low-porosity core surrounded by a light, high-porosity shell. (c) The time evolution of the outer radius of the core (orange) and the outer radius of the sphere (blue).

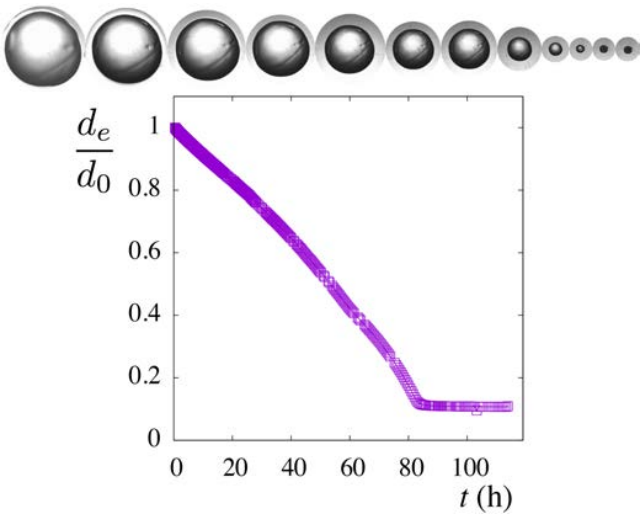

Figure 4.8: Time evolution of the diameter of the spherical gel during drying. Here d_0 is the fulley swelled or wet diameter. At $t = 0$, the swollen (wet) sphere is taken out water and put on a watch glass. A sequence of images showing the drying the polymer over the course of 120 hours. The whole experiment is conducted at $T = 22 \pm 1°C$.

light can not pass through.

4.4 Drying experiments

One question that can be asked is if the instability persists in the reverse process, that is during drying. In practice a slow gradual reduction of the sphere diameter is observed as depicted in figure 4.8. The drying process is much slower as it takes more than two days to completely dry a 25 mm sphere. It is clear that during drying there is an evaporation limited rate that may be related to the humidity rate in the room 45±5%. No uniform distinct pattern was observed during the drying except some imperfections. Note that wrinkling patterns similar to our swelling patterns were reported before during drying in PU/PBO (polypropylene oxide/polybutadiene) absorbing toluene[25,26]. An open question is why some gel network exhibit wrinkling on swelling and others in drying?

4.5 Conclusions and perspectives

An experimental study of the swelling of an hydrophilic polymer sphere in water has been presented. During swelling several patterns were observed. First, the pattern contains

[25]Trindade AC, Canejo JP, Pinto LFV, Patrício, Brogueira P, Teixeira PIC and Godinho MH. Wrinkling labyrinth patterns on elastomeric Janus particles. *Macromolecules* 44:2220-2228 (2011)

[26]Trindade AC, Canejo JP, Patrício, Brogueira P, Teixeira PIC and Godinho MH. Hierarchical wrinkling on elastomeric Janus particles. *J. Mater. Chem.* 22:22044 (2012)

many wrinkles and folds. Then, as water is absorbed the number of lobes decreases rapidly. The lobes merge and the pattern relaxes at large time scale. Using a shadowgraph technique the position of a hard core is monitored supporting the elastic explanation for the formation of the lobe pattern. The wavelength of the lobe pattern appears to grow linearly with the thickness of a soft shell, around the hard core, which absorbs water.

Hydrogels are sensitive to temperature and a short term study will be the drying at elevated temperature. It is anticipated that the stress will be affected by the drying process and cracks may form. These materials are also used to study fractures[27].

These hydrogel sphere have been used to study the behaviour of deformable granular materials[28,29,30,31,32,33] as their refractive index matched properties allows to see the arrangement of the particles inside the packing. Developing laboratory experiments with these type of materials is attractive as they are soft.

The curent comparison aims at predicting the swelling and drying times, the onset of the instability and the initial wavelength of the pattern. Such model using the nonlinear poroelastic approach is carried out in collaboration with Shomeek Mukhopadyay (Yale University), Thibault Bertrand (Yale University) and Chris MacMinn (Oxford University) upon the comparison of the present results with numerical results using the nonlinear poroelastic modelling.

From an experimental point of view, our future work will aim at developing a new technique to manufacture our own spherical gels. It is clear that the control of the cross-linking process is crucial to obtain reproducible diameters. On the other side, using natural gels, such as alginates or agar-agar, is attractive as it is a safe alternative. To manufacture gel beads, an number of techniques are available. However obtaining well controlled spheres of well controlled diameter seems to be an open problem. It is planned to develop new and innovative techniques to manufacture spherical hydrogel beads using centrifugal techniques[34]. Most important is to control the degree of cross-linking[11,25] that is directly related to the elasticity of the material. Clearly the instability could be influenced by other parameters such as the temperature, pH and the ionic strength.

Hydrogel spheres, once swollen are made of more that 99% water and have the same optical index as water. Yet there are small optical inhomogeneities that can be used to observe the motion, the position or the shape of these particle in a bulk flow. Recently,

[27]Baumberger T, Caroli C and Martina D. Solvent control of crack dynamics in a reversible hydrogel. *Nat. Mat.* 5:552-555 (2006)

[28]Lachhab T and Weill C. Compression of a soft sphere packing. *Eur. Phys. J. B* 9:59-69 (1999)

[29]Ye X, Ganley T, Morris JF, Tonmukayakul N and Parker MA. Uniaxial compression of dense granular materials: stress distribution and permeability. *J. Petrol. Sci. Eng.* 65:193-207 (2009)

[30]Lörincz KA and Schall P. Visualization of displacement fields in a sheared granular system. *Soft Matter* 6:3044-3049 (2010)

[31]Mukhopadhyay S and Peixinho J. Packing of deformable spheres. *Phys. Rev. E* 84:011302 (2011)

[32]Dijksman JA, Rietz F, Lörincz KA, van Hecke M and Losert W. Refractive index matched scanning of dense granular materials. *Rev. Sci. Instrum.* 83:011301 (2012)

[33]Brodu N, Dijksman J and Behringer RP. Scanning the scales of granular materials through microscopic force imaging. *Nat. Commun.* 6:6361 (2015)

[34]Gupta A, Eral HB, Hatton TA, Doyle PS. Controlling and predicting droplet size of nano-emulsions. 10^{th} Annual European Rheology Conference, Nantes (2015)5

fluorescence techniques using rhodamine in the spheres have been used to measure the arrangement of particle in packings[31,32,33].

Chapter 5

Conclusions and outlook

In the previous chapters, the developments of the three lines of research have been presented. Basically, these are simple experiments to quantify the development of instabilities or turbulence in some basic geometries. In the pipe flow experiments, the addition of perturbation in the form a finite amplitude disturbances initiated hairpin vortices and turbulent patches. Some conditions for the appearance of the hairpin vortices have been obtained, but the exact reason remains to be mathematically described. In the expansion pipe flow, disturbances gave rise to asymmetry, Kelvin-Helmholtz instability and then turbulent patches. One can wonder about the growth, the decay and the nonlinear growth of permanent and oscillating disturbances. Next, one can wonder about modifying turbulent flows, specifically turbulent Taylor-Couette flows, with polymers or particles.

5.1 Synthetic jet for transition in pipe flow

I am interested in using jets and synthetic jets actuators to test sub-critical expansion pipe flow. That is flow in a circular pipe expansion with the actuators at the inlet section. With Yuji Tasaka (University of Hokkaido, Japan) we are testing and developing a synthetic jet perturbations using a small motor, a chamber and an elastic membrane. It will push and pull liquid with an prescribed frequency and amplitude through a small hole at the inlet on the expansion pipe flow. The evolution of the disturbance will be monitored using sophisticated methods such as PIV (Particle Image Velocimetry) and LIF (Laser Induced Fluorescence) to explore the coherent flow structures in turbulent patches. We hope to record perturbation decay, transient growth and nonlinear growth to turbulence depending on the frequency and amplitude.

It will allow to answer a number of questions: can well defined finite-amplitude solutions be identified for a better description of the nonlinear dynamics inside the turbulent patch? Turning our attention to the spatiotemporal properties of the turbulent patches, can the frequency and amplitude modify the spatiotemporal properties of the turbulent patches. This can be particularly interesting from an industrial perspective, again as a way to passively control or delay the emergence of the turbulent patches or enhance the drag and the mixing of turbulent patches. In the range of large Re, we would like to test

if the localised turbulence can split just as in uniform pipe flow or in the flow behind a sphere (vortex shedding). Our previous measurements indicate that the puff grows in size as Re increases.

5.2 Turbulent Taylor-Couette flow

The presentation of previous works leads us to continue the research in Taylor-Couette flow in three different directions: (i) turbulent isothermal and heat Taylor-Couette flow, (ii) turbulent viscoelastic Taylor-Couette flow and (iii) multiphase Taylor-Couette flow. In all these cases, the previous experimental works have dealt mainly with visualisation. Our strategy is to combine visualisation to highly accurate torque measurements and velocity measurement. In the range of relatively small Re and specifically for the case $\eta = 0.6$, the Taylor vortex flow regime is very large so there is an opportunity to study the transition through wave-vortex interaction. Also, the presence of small wavelength Görtler vortices has been reported and may explain the different slopes observed in the Nu_ω versus Re curve. Clearly, the range of radius ratio is far from the applications but can be easily accessible to numerical simulations. Hence, the opportunity here is to produce enlightening studies that will teach students both methodologies (experiments and simulations). The main feature of the flow is the presence of the Taylor vortices observed both in experiments and simulations.

For the range of large Re, there are opportunities to perform laser Doppler velocimetry and PIV to obtain statistics of the turbulent flow, mean velocity profiles, Reynolds stresses, turbulent kinetic energy production and dissipation rates. Although turbulent structure function have been obtained before[13,19], only for $\eta \simeq 0.7$. Measuring it for our systems, $\eta = 0.6$ and 0.9 could lead to some new results.

As presented before, the Taylor-Couette flow is the ideal system to study polymer flow in order to study the drag enhancement and reduction phenomena. The phenomena can be quantified using torque measurements. A obvious extension of this work in the use of PIV to quantify the viscoelastic turbulence. More experiments could be performed using different polymer properties (flexible, rigid, long, short polymers) in order to quantify further the drag reduction phenomena.

We have presented an experimental study of the swelling and the drying of an hydrophilic sphere in water. During swelling several patterns corresponding to different stages during the growth of the spherical gel were observed. First the pattern contains many wrinkles and folds. Then, as water is absorbed the number of lobes decreases rapidly. The lobes merge and the pattern relaxes at large time scale. Using a shadowgraph technique the position of a hard core is monitored that support the elastic explanation for the lobe pattern. The wavelength of the lobe pattern appears to grow linearly with the thickness of the soft shell. Hydrogels are sensitive to temperature, pH, salt concentration, etc. These hydrogel sphere have been used to study the behaviour of deformable granular materials as their refractive index matched properties allows to see the arrangement of

the particles inside the packing. Developing laboratory experiments with these type of materials is attractive as they are soft. Specifically I would like to develop Taylor-Couette flow with hydrogel particles of different stiffness, different sizes and different concentrations. This system will help understand the drag reduction of bubbly Taylor-Couette flow as these particles have intermediate properties (deformability) and small buoyancy.

Appendix A

CV and Publications

A.1 Curriculum Vitæ

- Curriculum Vitæ
- List of publications
- List of supervised students and mentored postdoctoral associates

A.2 Publications associated with Chapter 2

- **J. Peixinho** and T. Mullin. Decay of turbulence in pipe flow. *Phys. Rev. Lett.* 96:094501 (2006)
- **J. Peixinho** and H. Besnard. Transition to turbulence in slowly divergent pipe flow. *Phys. Fluids* 25:111702 (2013)
- K. Selvam, **J. Peixinho** and A. P. Willis. Localised turbulence in a circular pipe flow with gradual expansion. *J. Fluid Mech.* 771:R2 (2015)

A.3 Publications associated with Chapter 3

- **J. Peixinho**, P. Mirbod and J. F. Morris. Free surface flow between two horizontal concentric cylinders. *Eur. Phys. J.* E 35:19 (2012)
- B. Martínez-Arias, **J. Peixinho**, O. Crumeyrolle and I. Mutabazi. Effect of the number of vortices on the torque scaling in Taylor-Couette flow. *J. Fluid Mech.*748:756-767 (2015)

A.4 Publication associated with Chapter 4

- Shomeek Mukhopadhyay and **J. Peixinho**. Packings of deformable spheres. *Phys. Rev.* E 84:011302 (2011)

CURRICULUM VITAE

Jorge PEIXINHO
Born in Vittel (France) the 18th of Mai 1976, Married
French and Portuguese Citizenships

Professional Address:
Laboratoire Ondes et Milieux Complexes
UMR 6294 CNRS et Université du Havre
53 rue de Prony
76058 Le Havre – France
Tel. 02 35 21 71 03
Email: jorge.peixinho@univ-lehavre.fr
WWW: https://sites.google.com/site/jmpeixinho

Research Career & Education

***Université Henri Poincaré - Nancy* 1 (now *Université de Lorraine*)**
2001 - 2004. *Thèse de Doctorat* (French Ph.D.) in Mechanic and Energetic at the *Laboratoire d'Energétique et de Mécanique Théorique et Appliquée* granted by *Agence Nationale de la Recherche Technique* and *Schlumberger*
Title: "*Contribution expérimentale à l'étude de la convection thermique en regime laminaire, transitoire et turbulent pour un fluide à seuil en écoulement dans une conduite*" under the supervision of **Chérif NOUAR and Michel LEBOUCHE**

University of Manchester (United Kingdom)
2004 - 2006. Postdoctoral Research Assistant at the Manchester Centre for Nonlinear Dynamics and Nonlinear and Liquid Crystal Group of the Physics and Astronomy Department of the University of Manchester under the supervision of **Tom MULLIN** (granted by EPRSC)

University of Tokyo (Japan)
2006 - 2008. Postdoctoral Research Fellow at the Fluid Engineering Laboratory of the Mechanical Engineering Department of the University of Tokyo under the supervision of **Yoichiro MATSUMOTO** (granted by JSPS)

City University of the City College of New York (United States of America)
2008 - 2010. Postdoctoral Research Associate at the Benjamin Levich Institute for Physico-Chemical Hydrodynamics and Chemical Engineering Department of the City University of the City College of New York under the supervision of **Jeffrey F. MORRIS** (granted by Chevron)

CNRS and Chimie-ParisTech
2010 - 2011. CNRS Postdoctoral Research Scientist for Chimie-ParisTech under the supervision of **Grégory LEFEVRE and François-Xavier COUDERT** (granted by *Electricité de France*)

2011 to present, CNRS and *Université du Havre*, *Chargé de Recherche* at the *Laboratoire Ondes et Milieux Complexes* (UMR 6294)

Publications

15 articles in refereed journal, 2 chapters in refereed conference books, 9 papers in proceedings of conferences, 39 communications in congress, symposiums and meetings with abstracts and 31 invited seminars in France and abroad.

Publications in Refereed Journals

A1 J. Peixinho, C. Nouar, C. Desaubry and B. Théron, Laminar transitional and turbulent flow of yield stress fluid in a pipe, *Journal of Non-Newtonian Fluid Mechanics*, 128, 172-184 (2005)
A2 J. Peixinho and T. Mullin, Decay of turbulence in pipe flow, *Physical Review Letters*, 96, 094501 (2006)
A3 I. Zuriguel, J. M. N. T. Gray, **J. Peixinho** and T. Mullin, Pattern selection by a granular wave, *Physical Review E*, 73, 118606 (2006)
A4 T. Mullin and **J. Peixinho**, Transition to turbulence in pipe flow, *Journal of Low Temperature Physics*, 145, 75-88 (2006)
A5 J. Peixinho and T. Mullin, Finite amplitude thresholds for transition in pipe flow, *Journal of Fluid Mechanics*, 582, 169-178 (2007)
A6 J. Peixinho, C. Desaubry and M. Lebouché, Heat transfer of a non-Newtonian fluid (Carbopol aqueous solutions) in transitional pipe flow, *International Journal of Heat and Mass Transfe*r, 51, 198, 198-209 (2008)
A7 A. P. Willis, **J. Peixinho**, R. R. Kerswell and T. Mullin, Experimental and theoretical progress in pipe flow transition, *Philosophical Transactions of the Royal Society A*, 366, 2671-2684 (2008)
A8 I. Zuriguel, **J. Peixinho** and T. Mullin, Segregation pattern competition in a thin rotating drum, *Physical Review E*, 79, 051303 (2009)
A9 J. Peixinho, P. U. Karanjkar, J. W. Lee and J. F. Morris, Rheology of hydrate forming emulsions, *Langmuir* 26(14) 11669-11704 (2010)
A10 S. Mukhopadhyay and **J. Peixinho**, Packing deformable spheres, *Physical Review E*, 84, 011302 (2011)
A11 J. Peixinho, P. Mirbod and J. F. Morris, Free surface morphology in the flow between two horizontal concentric cylinders, *European Physical Journal E*, 35, 19 (2012)
A12 J. Peixinho, G. Lefèvre, F.-X. Coudert and O. Hurisse, Water evaporation in silica colloidal deposits, *Journal of Colloid and Interface Science*, 408, 206-211 (2013)
A13 J. Peixinho and H. Besnard, Transition to turbulence in slowly divergent pipe flow, *Physics of Fluids*, 25, 111702 (2013)
A14 B. Martínez-Arias, **J. Peixinho**, O. Crumeyrolle and I. Mutabazi, Effect of the number of vortices on the torque scaling in Taylor-Couette flow, *Journal of Fluid Mechanics*, 748, 756-767 (2014)
A15 K. Selvam, **J. Peixinho** and A. P. Willis, Localised turbulence in a circular pipe flow with gradual expansion, *Journal of Fluid Mechanics*, 771, R2, 1-13 (2015)

Chapters in Refereed Conference Books

B1 T. Mullin and **J. Peixinho**, Recent observation in the transition to turbulence in a pipe, in International Union of Theoretical and Applied Mechanics (IUTAM) Symposium on Laminar-Turbulent Transition, Bangalore, India (2005) (editor Rama Govindarajan), Springer 45-55 (2006)
B2 J. Peixinho, Flow in a slowly diverging pipe section, in IUTAM Symposium on Laminar-Turbulent Transition, Stockholm, Sweden (2009) (editor Philipp Schlatter and Dan S. Henningson) (2010)

Publications in Proceedings of Conferences

C1 F. Brand, **J. Peixinho** and C. Nouar, A quantitative investigation of the laminar to turbulent transition: application to efficient mud cleaning, Society of Petroleum Engineers (SPE) 71375, New Orleans, Louisiana, US (2001)
C2 J. Peixinho, C. Nouar, C. Desaubry and B. Théron, Laminar transitional and turbulent flow of yield stress fluids in a pipe, European Conference on Rheology (eurheo 2002) Erlangen, Germany (2002)
C3 J. Peixinho, C. Nouar, C. Desaubry and B. Théron, Convection thermique pour des fluides non-Newtoniens en conduite annulaire en régime laminaire transitoire et turbulent, Société Française de Thermique (SFT), Grenoble, France (2003)
C4 K. Okamoto, K. Hashiguchi, **J. Peixinho**, A. Fujiwara, S. Takagi and Y. Matsumoto, The breakup of an air bubble injected into a convergent-divergent nozzle pipe flow, in Proceedings of the International Conference on Multiphase Flow (ICMF), Leipzig, Germany (2007)
C5 A. Fujiwara, K. Okamoto, K. Hashiguchi, **J. Peixinho**, S. Takagi and Y. Matsumoto, Bubble breakup phenomena in a Venturi tube, in Proceedings of the 2007 American Society of Mechanical Engineer/Japanese Society of Mechanical Engineer Fluids Engineering Division Summer Meeting (ASME/JSME FEDSM), San Diego, California, US (2007)
C6 J. Peixinho, Ecoulement dans un tube faiblement divergent, transition laminaire-turbulent, 15ème Rencontre du Non-Linéaire (RNL), Paris, France (2012)
C7 J. Peixinho and S. Mukhopadhyay, Diffusion-mechanical instability of a spherical gel, 16ème RNL, Paris, France (2013)
C8 B. Matínez-Arias, **J. Peixinho**, O. Crumeyrolle and I. Mutabazi, Torque measurements in Newtonian and non-Newtonian fluids in Taylor-Couette flow, Iberian Meeting on Rheology (IBEREO) in Perspective in fundamental and applied rheology, 2nd Edition, Edited by F. J. Rubio-Hernández, A. I. Gómez-Merino, C. del Pino, L. Paras, L. Campo-Deaño, F. J. Galindo-Rosales and Velázquez Navarro, in the Ibereo-American Journal of Rheology (e-rheo-iba.org), Málaga (2013)
C9 L. Kahouadji, H. Yoshikawa, **J. Peixinho** and I. Mutabazi, Heat transfer by Görtler vortices on a wall with finite conductivity, 17ème RNL, Paris, France (2014)

Communications in congress, symposiums and meetings with abstracts

D1 Talk, **J. Peixinho**, C. Nouar and C. Desaubry, Pipe flow of a yield stress fluid, Annual European Rheology Conference (AERC), Guimaraes, Portugal (2003)
D2 Contributed Talk, C. Nouar, **J. Peixinho** and C. Desaubry, Laminar-turbulent transition for a yield stress fluid flow in a pipe, Banff Workshop: Visco-plastic fluids, from theory to application, Banff, Canada (2005)
D3 Poster, **J. Peixinho** and T. Mullin, Tentative of flow pattern in turbulent laminar transition in pipe flow, Isaac Newton Institute (INI) Workshop: Developments in experimental pattern formation, Cambridge, UK (2005)
D4 Talk, **J. Peixinho** and T. Mullin, An experimental investigation of the relaminarization of pipe flow, American Physical Society (APS) Division of Fluid Dynamics (DFD), Chicago, Illinois, US (2005)
D5 Contributed Talk, T. Mullin and **J. Peixinho**, Transition to turbulence in pipe flow, Warwick Turbulence Symposium, Warwick, UK (2005)
D6 Contributed Talk, T. Mullin and **J. Peixinho**, Invited Talk The transition to and from turbulence in pipe flow, APS March meeting, Baltimore, Maryland, US (2006)
D7 Contributed Talk, I. Zuriguel, J. M. N. T. Gray, T. Mullin and **J. Peixinho**, Uphill wave governing a segregated pattern, DygraM, Rennes, France (2006)
D8 Talk, **J. Peixinho** and T. Mullin, Invited Talk in the mini-symposia "New developments in hydrodynamic stability" Thresholds for turbulence transition in pipe flow, Euromech Fluid Mechanics Conference (EFMC), Stockholm, Sweden (2006)
D9 Poster, **J. Peixinho**, S. Takeuchi, S. Takagi and Y. Matsumoto, Instability of a large bubble in a divergent tube, Rencontre annuelle des chercheurs francophones travaillant au Japon, Tokyo, Japan (2007)
D10 Talk, **J. Peixinho**, K. Kazuhiro, S. Takagi and Y. Matsumoto, Short-term dynamics of a bubble into a convergent-divergent pipe flow, APS DFD, Salt Lake City, Utah, US (2007)
D11 Contributed Talk, R. K. Kowalski, B. Piros, **J. Peixinho**, K. Shiba, K. Yoshida and M. Yoshida, Sperm subpopulation in rainbow trout (Oncorhynchus Mykiss) – Computer Assisted Sperm Analyser (CASA) results and derived phenomenological criteria, Aquaculture Europe, Krakow, Poland (2008)
D12 Talk, **J. Peixinho**, S. Takeuchi, S. Takagi and Y. Matsumoto, Instability of the interface of a rising bubble in a vertical diverging pipe, EFMC7, Manchester, UK (2008)
D13 Contributed Talk, K. Hashiguchi, R. Tachibana, K. Shimizu, A. Fujiwara, **J. Peixinho**, S. Takagi and Y. Matsumoto, Liquid jet in a bubble through a converging tube, The seventh Japanese Society of Mechanical Engineer/Korean Society of Mechanical Engineer Thermal and Fluids Engineering Conference (JSME/KSME TFEC), Sapporo, Japan (2008)
D14 Contributed Talk, P. U. Karanjkar, **J. Peixinho**, J. W. Lee and J. F. Morris, Rheology and CP hydrate-forming emulsions, 13th International Conference on Surface and Colloid Science of the International Association of Colloid and Interface Scientists (IACIS) and 83rd American Chemical Society (ACS), Colloid and Surface Science Symposium, New York, NY, US (2009)
D15 Poster, **J. Peixinho**, G. Lefèvre, F.-X. Coudert and O. Hurisse, Confined water boiling in silica colloidal crystal, Thermodynamics, Athens, Greece (2011)

D16 Poster, **J. Peixinho**, O. Crumeyrolle, A. Prigent and I. Mutabazi, Newtonian and non-Newtonian fluid flow in a slowly diverging pipe expansion, The 16th International Congress on Rheology (ICR 2012), Lisbon, Portugal (2012)
D17 Talk, **J. Peixinho**, O. Crumeyrolle, A. Prigent and I. Mutabazi, Ecoulement dans une conduite divergente : experiences et simulations, Journées Activités Universitaires en Mécanique-Association Française de Mécanique (AUM-AFM), Rouen, France (2012)
D18 Poster, **J. Peixinho**, G. Lefèvre, F.-X. Coudert and O. Hurisse, Confined water boiling in silica colloidal crystal, Nuclear Plan Chemistry Conference, Paris, France (2012)
D19 Contributed Talk, B. Martínez-Arias, **J. Peixinho**, O. Crumeyrolle and I. Mutabazi, Torque measurements in Newtonian and non-Newtonian fluids in Taylor-Couette flow, 18th International Couette-Taylor Workshop (ICTW), Enschede, The Netherlands (2013)
D20 Talk, **J. Peixinho**, Newtonian and non-Newtonian fluid flow in a slowly diverging pipe expansion, Iberian Meeting on Rheology (IBEREO), Málaga, Spain (2013)
D21 Talk, **J. Peixinho**, B. Martínez-Arias and I. Mutabazi, Torque scaling and number of states in turbulent Taylor-Couette flow, APS DFD Pittsburgh, Pennsylvania, US (2013)
D22 Contributed Talk, I. Mutabazi, H. Yoshikawa, **J. Peixinho** and L. Kahouadji, Heat transfer enhancement by the Görtler vortices developed on a wall with finite thermal conductivity, APS DFD Pittsburgh, Pennsylvania, US (2013)
D23 Talk, **J. Peixinho** and K. Selvam, Laminar-turbulent transition in the flow through a gradual expansion in a circular pipe, Euromech Colloquium (EC565), Subcritical transition to turbulence, Cargèse, France (2014)
D24 Contributed Talk, B. Martínez-Arias, **J. Peixinho**, O. Crumeyrolle and I. Mutabazi, Visualizations and torque measurements of viscoelastic fluid in Couette-Taylor flow, Workshop Instabilities and Turbulence in Stratified Rotating Flows (ISTROF), Le Havre, France (2014)
D25 Contributed Talk, K. Selvam and **J. Peixinho**, Localized turbulence in a divergent pipe flow, ISTROF, Le Havre, France (2014)
D26 Contributed Talk, K. Selvam and **J. Peixinho**, Localized turbulence in a circular pipe flow with a gradual expansion, 3rd Nek5000 Users & Developers Meeting, Conference Centre, Aristotle University of Thessaloniki, Thessaloniki, Greece (2014)
D27 Poster, **J. Peixinho**, B. Martínez-Arias, M.-C. Renoult and I. Mutabazi, Instabilité des filaments viscoélastiques, 49ème Congrès Annuel du Groupe Français de Rhéologie (GFR), Grenoble, France (2014)
D28 Poster, B. Martínez-Arias, **J. Peixinho**, O. Crumeyrolle, et I. Mutabazi, Couple et nombre de rouleaux dans un écoulement de Taylor-Couette pour des fluides viscoélastiques, 18ème RNL, Paris, France (2015)
D29 Poster, K. Selvam, **J. Peixinho** and A. P. Willis, Turbulence in a gradual expansion circular pipe flow, 18ème RNL, Paris, France (2015)
D30 Talk, **J. Peixinho**, S. Mukhopadhyay, T. Bertrand and C. MacMinn, Diffusion-mechanical instability of spherical spheres, AERC Nantes, France (2015)
D31 Poster, B. Martínez-Arias, **J. Peixinho**, O. Crumeyrolle, and I. Mutabazi, Torque in Taylor-Couette flow of viscoelastic polymer solutions, AERC Nantes, France (2015)

D32 Contributed Talk, M.-C. Renoult, **J. Peixinho**, O. Crumeyrolle and I. Mutabazi, The break-up of viscoelastic jets and filaments: the bead-on-a-string structure, AERC Nantes, France (2015)
D33 Poster, K. Selvam, **J. Peixinho** et A. P. Willis, Turbulence in a gradual expansion circular pipe flow, Understanding and harnessing turbulence honouring W. K. George on occasion of his 70th birthday, Cargèse, France (2015)
D34 Contributed Talk, B. Martínez-Arias, **J. Peixinho**, A. Froitzheim, S. Merbold, C. Egbers and I. Mutabazi, Influence of the radius ratio on the torque in turbulent Taylor-Couette flow, 19th ICTW, Cottbus, Germany (2015)
D35 Contributed Poster, K. Selvam, **J. Peixinho** and A. P. Willis, Turbulence in a gradual expansion circular pipe flow, 19th ICTW, Cottbus, Germany (2015)
D36 Contributed Talk, B. Martínez-Arias, **J. Peixinho**, O. Crumeyrolle and I. Mutabazi, Drag enhancement in subcritical transition to inertio-elastic turbulence in Couette-Taylor flow, 19th ICTW, Cottbus, Germany (2015)
D37 Contributed Poster, M.-C. Renoult, **J. Peixinho**, O. Crumeyrolle and I. Mutabazi, Drop dynamics on a viscoelastic filament: an experimental study, Fluid & Elasticity, Biarritz, France (2015)
D38 Contributed Talk, K. Selvam, **J. Peixinho** and A. P. Willis, Transition to turbulence in a circular pipe flow with gradual expansion, Bifurcations and Instabilities in Fluid Dynamics (BIFD), Paris, France (2015)
D39 Contributed Talk, M.-C. Renoult, **J. Peixinho**, O. Crumeyrolle and I. Mutabazi, Instability of dilute polymer jets, BIFD, Paris, France (2015)

Invited seminars

E1 Pipe flow of a yield stress fluid, Schlumberger, Clamart, France (2003)
E2 Heat transfer of a pipe flow yield stress fluid, Schlumberger, Clamart, France (2004)
E3 Laminar transitional and turbulent flow of yield stress fluids in a pipe, Manchester Centre for Nonlinear Dynamics (MCND), Manchester, UK (2005)
E4 Transition to and from turbulence in pipe flow, MCND (2006)
E5 Thresholds for turbulence transition in pipe flow, Applied Mathematics Seminar, University of Bristol, UK (2006)
E6 Transition thresholds of impulsive perturbations in pipe flow, Panta Rhei Seminar, Laboratory for Aero & Hydrodynamics, Delft, the Netherlands (2006)
E7 Transition to turbulence in pipe flow, Fluid Engineering Laboratory (FEL), Mechanics Engineering Department, University of Tokyo, Japan (2006)
E8 Transition to turbulence in pipe flow, Department of Physics, University of Tokyo, Japan (2007)
E9 Granular segregation in a rotating drum, FEL (2007)
E10 Relaminarisation in pipe flow, Department of Mechanical Systems Engineering, Shinshu University, Nagano, Japan (2007)
E11 Finite amplitude thresholds for transition and relaminarisation in pipe flow, Department of Aerospace, Tokyo Metropolitan Institute of Technology, Japan (2007)
E12 Finite amplitude thresholds for transition in pipe flow, Department of Physics, Osaka City University, Japan (2007)

E13 Seuils de transition laminaire-turbulent et relaminarisation de l'écoulement dans un tube cylindrique, Institut Jean Le Rond d'Alembert, Complex Fluids and Instabilities Group, Université Pierre et Marie Curie, Paris, France (2007)
E14 Short-term dynamics of a bubble into a convergent-divergent pipe flow, FEL Symposium (2007)
E15 Transition to turbulence in pipe flow, Fluid Control Laboratory, Hokkaido University, Sapporo, Japan (2008)
E16 Transition to and from turbulence in pipe flow, Levich Institute (2008)
E17 Flow in slowly diverging pipe expansion sections, Levich Institute (2008)
E18 Free surface morphology in the flow between two horizontal concentric cylinders, Levich Institute (2009)
E19 Transition à la turbulence de l'écoulement de Hagen-Poiseuille, Laboratoire Ondes et Milieux Complexes (LOMC), Le Havre, France (2010)
E20 Transition to turbulence in slowly diverging pipe flow, Cottbus, Germany (2011)
E21 Transition à la turbulence dans un tube cylindrique divergent, Laboratoire de Mathématique Appliquées, Université du Havre (2013)
E22 Ecoulement dans un tube divergent, Laboratoire d'Informatique pour la Mécanique et les Sciences de l'Ingénieur (LIMSI), Orsay, France (2013)
E23 Flow in a diverging pipe, LadHyX, Ecole Polytechnique, Palaiseau, France (2013)
E24 Ecoulement dans un tube divergent, Laboratoire d'Energétique et de Mécanique Théorique et Appliquée (LEMTA), Université de Lorraine, France (2013)
E25 Transition à la turbulence dans un tube cylindrique divergent, DynFluid, Arts et Métiers ParisTech, Paris, France (2013)
E26 Laminar-turbulent transition in the flow through a gradual expansion in a circular pipe, Lehrstuhl für Aerodynamik und Strömungslehre, Brandenburgische Technische Universität, Cottbus, Senftenberg, Germany (2014)
E27 Laminar-turbulent transition in pipes and Taylor-Couette flow, Tokyo University of Science, Japan (2015)
E28 Taylor-Couette flow of polymer solutions or interfaces, I^2plus Seminar, Tokyo University of Science, Japan (2015)
E29 Localised turbulence in circular pipe with gradual expansion: experiments and simulations, Osaka University, Japan (2015)
E30 Localised turbulence in circular pipe flow with gradual expansion: experiments and simulations, Osaka University, JSPS-CNRS Sakura meeting, ESPCI-Paris (2015)
E31 Localised turbulence in circular pipe flow with gradual expansion: experiments and simulations, Rencontres Niçoises de Mécanique des Fluides, Nice (2015)

Services

- Referee for scientific journals (alphabetical order): Chemical Engineering Science, Chemical Physics Letters, Europhysics Letters, Environmental Earth Sciences, Experimental Thermal and Fluid Science, International Journal of Heat and Mass Transfer, Journal of Fluid Mechanics, Journal of Fluids and Structures, Journal of Non-Newtonian Fluid Mechanics, Nature Communications, Physics of Fluids
- Referee for organisations: International Union of Theoretical and Applied Mechanics (IUTAM), University of Málaga, Swiss National Science Foundation (SNF), Agence Nationale de la Recherche (ANR)

Supervised Students, Mentored Postdoctoral Associates and other activities

I have mentored or co-mentored 3 Postdoctoral Associates, supervised or co-supervised 2 *thèses de doctorat*, 4 Master students, 7 Undergraduate students and 2 High-school students.

High-school Students
Juliette LEMAITRE (2013), Natacha MACE (2012)

Undergrad Students
Jumpei OHKUBO (2014), Norio YONEZAWA (2013), Susan TAN (2010), Lucas SCHIMMER (2009), Coralie CARMOUZE (2008), John COULET (2008), Hélène PENISSI (2002)

Master Students:
- Rodrigue Stephane MBAKOP (2014): *Caractérisation de solutions viscoélastiques de polymères par mesures de tension de surface et de viscosité*
- Khac Lan NGUYEN (2012): *Modélisation numérique de l'écoulement du fluide viscoélastique incompressible d'Oldroyd-B dans un tube divergent*
- Abou BA (2012): *Etude de l'écoulement dans un tube faiblement divergent*
- Matheus PEIXOTO DE OLIVEIRA (2012): *Etude de l'influence du type de forçage sur les premiers modes d'instabilités de l'écoulement de Couette-Taylor viscoélastique*

PhD Students:
- Borja MARTÍNEZ-ARIAS, from September 2012 to September 2015: Torque measurement in turbulent Couette-Taylor flows
- Kamal SELVAM, from October 2013 to October 2016: Transition to turbulence in circular expansion pipe flow

Post-doctoral Researchers:
Lyes KAHOUADJI, from July 2013 to July 2014, Heat transfer by Görtler vortices developed on a wall with finite conductivity
Harunori YOSHIKAWA, from January 2012 to July 2013, Heat transfer by Görtler vortices developed on a wall with finite conductivity
Marie-Charlotte RENOULT, from August 2014 to August 2016

Since 2011, I work at LOMC, organised the seminar series (15 seminars per year), organised the *Journée des Doctorants* and have been a member of the *Conseil du Laboratoire* of LOMC.
I co-organised, made the website and edited the book of abstracts of the Workshop Instabilities and Turbulence in Strato-Rotational Flows (Workshop ISTROF) 2014 (40 participants):
https://sites.google.com/site/liaistrof/

Decay of Turbulence in Pipe Flow

J. Peixinho and T. Mullin

School of Physics and Astronomy, The University of Manchester, Manchester M13 9PL, United Kingdom

(Received 15 November 2005; published 8 March 2006)

A novel experiment has been devised which provides direct evidence for critical point behavior in the longstanding problem of the transition to turbulence in a pipe. The novelty lies in the quenching of turbulence by reducing the Reynolds number and observing the decay of disordered motion. Divergence of the time scales implies underlying deterministic dynamics which are analogous to those found in boundary crises in dynamical systems. A modulated wave packet emerges from the long term transients and this coherent state provides evidence for connections with recent theoretical developments.

DOI: 10.1103/PhysRevLett.96.094501 PACS numbers: 47.20.−k, 47.27.−i, 47.60.+i

The enigma of why the fluid motion in a pipe becomes turbulent as the flow rate increases has puzzled the physics community for more than a century [1,2]. All evidence suggests that the flow is linearly stable [3] for all Re. (Here $\mathrm{Re} = UD/\nu$ where U is the mean speed, D is the diameter of the pipe, and ν is the kinematic viscosity of the fluid.) In practice, however, pipe flows are observed to be turbulent even at modest flow rates. The transition to turbulence occurs above a definite amplitude of an injected perturbation and is catastrophic [4]. It is difficult to isolate the effective part of the perturbation, so that the mechanism for transition remains aloof. Therefore, we have devised a novel experiment to investigate the reverse transition, i.e., the change from turbulent to laminar flow. The flow can now be considered as a dynamical system where the turbulent attractor loses stability at a crisis as a parameter is changed [5,6]. Exponential decay of the disordered motion is found when the Reynolds number is reduced and, moreover, the observed divergence in the time scales indicates an underlying critical event. Interestingly, the long term decaying transients contain wavelike structures which point the way to direct connections with modern theoretical developments [7,8].

The size of the disturbance required to cause transition has been shown to scale as Re^{-1} [9]. This relationship cannot hold for small values of Re and it was recently shown that there is a sharp cutoff [10] at $\mathrm{Re} \sim 1800$, i.e., below this value sustained turbulent flow cannot be created by injecting large amplitude disturbances. Further, obtaining clear estimates of this lower limit using significant perturbations produces large scatter in the data since it is known that the flow is sensitive to background noise [1]. The transition process which takes the flow from the laminar to turbulent states is catastrophic [4] and it is thus difficult to obtain insight into the detailed mechanisms involved in the creation of turbulence from onset experiments. Furthermore, the final state which evolves out of the transition process has the form of a localized patch of disordered motion [11,12] in the Re range 1800–3000. Their spatial extent is constant for $\mathrm{Re} < 2223$ [13] and in this Re range they have been called ''equilibrium puffs'' [11] since they do not change their form. Puffs travel at a well defined speed of $\simeq 0.9U$, are approximately 20 pipe diameters long, and comprise a block of disordered flow with a weak decaying wave at the front and a sharp rear interface. They are structured [11] and, recently, more details of the structure [14] have been revealed. Cross-sectional views contain azimuthal features which are similar to traveling waves found in recent theoretical work [7,8].

Our strategy was to generate a turbulent puff and observe its decay back to Poiseuille flow as Re was reduced in a well-controlled manner. The puff can be considered as a natural state or attractor for the system. The objective was to see if the reverse transition was less abrupt, which in turn may reveal more definite evidence for traveling wave states. The decay of turbulence in pipe flows has been investigated in the past where the focus was on the change from fully turbulent to laminar flows [15–17]. The reduction in Re was achieved using both suddenly expanding and diverging pipes so that change in Re was localized. The investigations were concerned with the evolution of spectral properties of the flow and exponential decay of turbulence was found with different exponents for central and near-wall regions. In our experiment, the chosen initial state of the flow was an equilibrium puff which was generated by introducing a short duration perturbation into Poiseuille flow. Then Re was reduced in a controlled way and the subsequent evolution of the puff was monitored as it progressed downstream.

A schematic diagram of a side-view of the apparatus is presented in Fig. 1. The pipe consisted of a tube of diameter $D = 20 \pm 0.01$ mm which was constructed using 150 mm long machined sections push fitted together and

FIG. 1 (color online). Schematic diagram of the pipe flow facility (drawn to scale). The piston moves at a controlled speed and the fluid is pulled through the pipe at constant mass flux. The usable experimental run time is ≈ 30 min.

butted flush so that there was no measurable gap between each section. The pipe was held on a steel base with a total length of 15.7 m ($785D$) and was aligned using a laser. A reservoir with a capacity of 100 liters was connected to the pipe through a smooth trumpet shaped inlet. A 30 cm diameter piston inside a ground steel cylinder pulled the fluid at a constant mass flux along the pipe using a computer controlled motor and lead screw arrangement. Hence, even if the fluid in the pipe became turbulent, the mass flux pulled through the pipe was unaffected, so that the Re remained constant. The experimental facility also allowed the speed of the piston to be varied as a function of time, i.e., the mass flux could be changed during a run to specified values in a controlled way. The long term temperature stability of the laboratory was controlled to $\pm 1\,^{\circ}\mathrm{C}$ at a mean temperature of $20\,^{\circ}\mathrm{C}$. A typical temperature gradient recorded from several thermocouple along the pipe was $0.2\,^{\circ}\mathrm{C}$. By these means, we were able to maintain an accuracy in Re of better than 1%. The facility enabled a laminar flow to be achieved up to a flow rate corresponding to $\mathrm{Re} = 23\,000$. The flow state was monitored using Mearlmaid Pearlessence as flow visualization and single point velocity measurements were made using standard laser Doppler techniques in separate experiments.

An outline of the flow control procedure is shown in Fig. 2. Each experimental run proceeded as follows. An equilibrium puff was generated by introducing a perturbation into fully developed Poiseuille flow 185 diameters from the pipe entrance at $\mathrm{Re} = 1900$. The perturbation was created using a boxcar pulse of fluid which was injected tangential to the main flow via a ring of six equally spaced 0.5 mm holes. The amplitude of perturbation was selected using the criterion established previously [9]. In principle, the perturbation will have a global effect on the flow but checks using push-pull disturbance generators shows that the perturbation is localized in practice. The puff was allowed to evolve for a further 100 diameters so that any of the known sensitivity to initial conditions [4] was lost. Then Re was reduced at a constant rate of 10/ sec to a prescribed value in the range 1580–1740 and the evolution of the puff observed. The reduction in Re was achieved by decelerating the piston which pulled the flow under computer control so that the mass flux was reduced simultaneously all along the pipe. A settling time of 1 h between each experimental run was found to be sufficient to ensure that disturbances in the header tank had decayed.

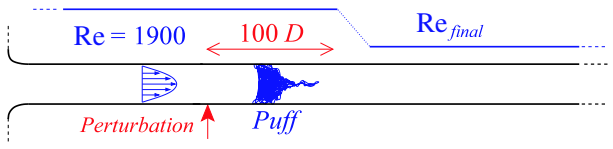

FIG. 2 (color online). Schematic of flow control procedure. Poiseuille flow was developed at $\mathrm{Re} = 1900$ for $185D$ and a perturbation was injected (indicated by the arrow). The puff progressed downstream for $100D$ and Re was then reduced to a prescribed value.

The initial effect of the reduction was that all of the puffs shrank to approximately half their original size during the deceleration phase. The weak wave structure at the head of the puff remained and there was evidence of vortical structures at the tail of the puff. The initial stages of decay were subtle but the final collapse was clear. In the latter stages, the block of vigorous disordered motion at the rear of the puff became detached from the wall and decayed rapidly. This was followed by the decay of the longer waves at the head of the puff. The distance taken for the disordered patch to decay was probabilistic in nature. Hence, the most useful measure which could be taken was the probability, P, of observing a localized disturbed region of flow as a function of distance downstream measured in pipe diameters (D). The measurements were made using between 20 and 50 runs of the experiment for each value of Re. The results are shown in Fig. 3 where the point of injection of the initial perturbation corresponds to zero on the abscissa. The straight lines are least squares fits of exponentials $P(D) \propto \exp(-CD)$ to the experimental data points, where C is a constant. Clear exponential decay is indicated by quality of the least squares fitted lines to the experimental points. It can be seen that the slopes increase as $\mathrm{Re}_{\mathrm{final}}$ decreases, i.e., the distance required for the puff to decay is shorter for smaller $\mathrm{Re}_{\mathrm{final}}$.

A measure which can be extracted from the exponential fits is the time required for half of the initial states to decay [18] and this is defined as the half-life $\tau = (\ln 2)/C$. A

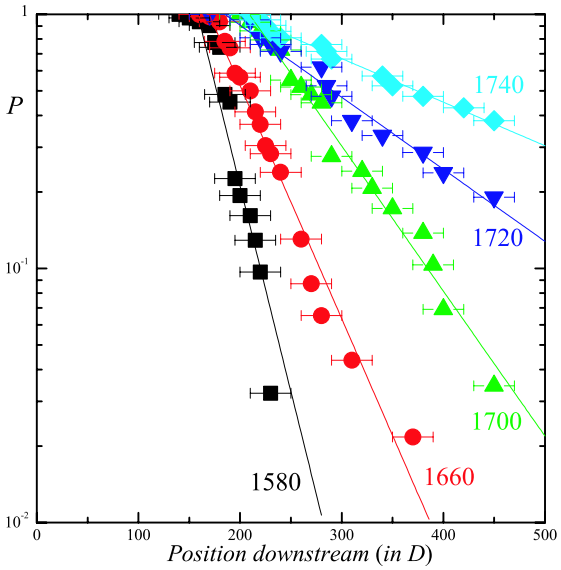

FIG. 3 (color online). Probability of observation of a puff versus downstream distance from the point of perturbation for a range of Reynolds numbers (1580–1740). The data are plotted on lin-log scales. The error bars indicate the experimental uncertainty of the measurements.

graph of τ versus Re is shown in Fig. 4 where it can be seen that there is a sharp cutoff at $\mathrm{Re}_c = 1750 \pm 10$, i.e., the half-life diverges at this value. More points have been used to construct Fig. 4 than available from the set of time histories represented in Fig. 3 (solid points). Some of the results (empty symbols) were obtained using different forms of perturbation including both injection and suction as well as combined injection and suction in one or several holes. In short, the results are independent of the method of creation of the puffs. Further tests on the robustness of the results included varying the distance that the puff was allowed to evolve between 10 and $500D$ and changing the deceleration rate of Re from 1 to 1000/ sec. The results were robust and were unaffected by any of these changes.

The exponential decay in the probability of observing a puff downstream suggests that, at each value of Re, they are independent events following a Poisson process. However, the least squares fit to the data in Fig. 4 shows that the half-life $\tau \propto (\mathrm{Re}_c - \mathrm{Re})^{-1\pm0.02}$, which in dynamical systems theory is a generic feature associated with transient behavior where an attractor loses stability at a crisis [5,6]. In maps and low-dimensional dynamical systems the exponent has been found to be less than 1 but the qualitative features are similar to those uncovered here. Clearly describing the complicated state of turbulence with its associated spatiotemporal disorder using the language of low-dimensional strange attractors is fraught with difficulties [19]. However, if the puff travels at a well-defined speed it is perhaps justified to consider the temporal evolution of the system in a translating frame of reference while neglecting the spatial evolution. Moreover, at these relatively low values of Re it is well known that it contains some spatial and temporal order [11,14]. Therefore considering the puff as a translating low-dimensional complicated dynamical state is a reasonable first order approximation.

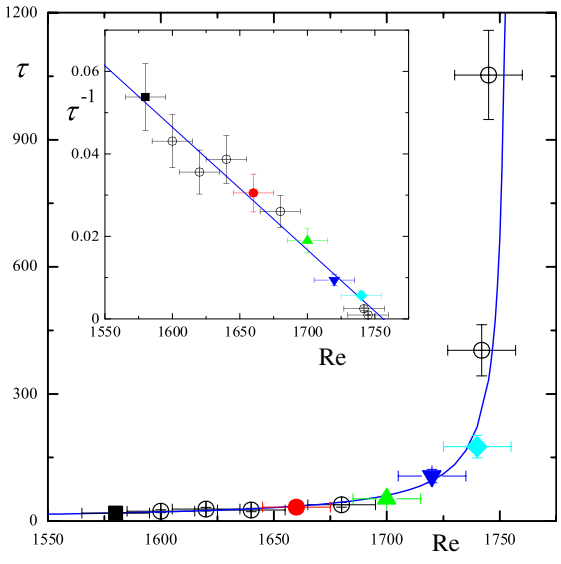

FIG. 4 (color online). Variation of the mean decay rate as a function of Re and a fit, which indicates a sharp cutoff at $\mathrm{Re}_c \approx 1750 \pm 10$. The inset is the inverse half-life versus Re and a linear fit.

When Re is reduced to 1750 ± 10, $\tau \to \infty$, an interesting new type of behavior was observed. We illustrate this using the photographs and velocity-time traces shown in Fig. 5. The velocity-time series were measured using a laser Doppler velocimeter which measured the azimuthal flow component $0.2D$ from the wall. A close-up view ($\approx 10D$) of the disordered region of an equilibrium puff [4,11] at $\mathrm{Re} = 1900$ is shown in Fig. 5(a). The entire puff is approximately 20 diameters long and we have omitted the decaying wavy structure which exists to the right of the field of view of the photograph. Small scale structures are evident and the puff reverts to laminar featureless flow abruptly in the left-hand side. The velocity trace is irregular although details of the temporal structure cannot be seen on the scale of Fig. 5(b). A flow visualization photograph of the state obtained after the reduction of Re to 1750 is shown in Fig. 5(c). The lifetime of the decaying disturbed flow approached infinity at this value of Re and hence the decay was very slow and the observed structure passed beyond the end of the pipe. Hence, it was not possible to decide whether this flow was stable or a long lived transient. The flow depicted in Figs. 5(c) and 5(d) is clearly more structured than those in Figs. 5(a) and 5(b) with a modulated wave pattern which has an axial wavelength of order of $1D$. These structures were observed to emerge after the initial decay of the small scales but in this range of Re they had a more definite and regular form. In practice, the right-hand edge of this wavelike structure reverted to laminar flow via the weak decaying wave associated with puffs so that the total size of the wavy states was on the order of 50 pipe diameters.

It is interesting to note that wavelike structures are not a strong feature of experimental investigations of plane Couette flow [18,20–22], where exponential decay is also found. The initial conditions in plane Couette flow is a fully disordered patch of fluid which does not have the clear spatiotemporal structures found in an equilibrium puff. This important aspect is also a significant difference with numerical modeling work on Poiseuille flow where a very short calculation domain is used together with periodic boundary conditions [23] with fully disordered initial conditions. Another detail which can be seen in the flow visualization photograph in Fig. 5(c), is two longitudinal vortices at the left-hand side which shows a sharp contrast with the puff shown in Fig. 5(a). Moreover, the velocity-time trace shown in Fig. 5(d) contains an evident wave packet trace of wavelength $1.5D$. This is consistent with the global characteristic of the recently discovered development radial symmetric ($m = 2$) traveling wave which has a typical longitudinal wavelength of $1.5D$ [7,8].

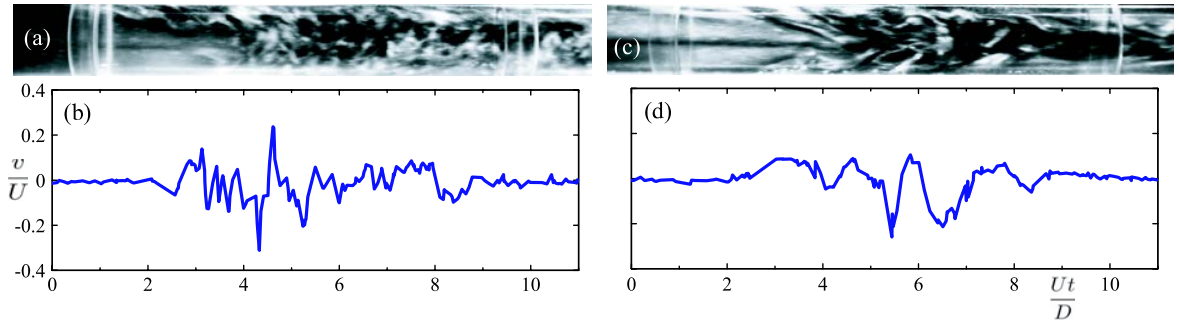

FIG. 5 (color online). Flow visualization (the flow is from left to right) and azimuthal velocity-time trace for initial and final flows: (a),(b) Re = 1900 and (c),(d) Re = 1750 after reduction of Re. These wavelike states were observed in 10% of the experiments.

Our results demonstrate a clear threshold for laminar-turbulent transition which is manifest in the approach to infinity of the lifetime of a disordered patch of fluid at a critical Reynolds number. Below the threshold, turbulence decays systematically via an exponential reduction in the probability of the propagation distance. Close to the threshold, the half-life becomes infinite and a new state which comprises a modulated wave packet emerges. An apparently simple scaling law with an exponent of one has been obtained by performing a ''clean'' experiment. The effects of initial conditions have been removed using a natural state of system, the equilibrium turbulent puff. Hence the effects of external noise, which can lead to long transients in dynamical systems [24] have been significantly reduced. The divergence in time scales provides a definite estimate with small error bars for the lower critical threshold which is in accord with previous values [13,17]. Perhaps, most importantly, our results indicate that the laminarization process progresses through structured stages and suggests a new research direction which will enable a detailed quantitative comparison between experiment and theory. This challenge may be met using a numerical approach with longer calculation domains where the spatiotemporal structure of the flow can be accommodated.

This research is supported by EPSRC via Grant No. GR/576137/01 (J. P.) and additional support (T. M.). We are grateful to R. R. Kerswell for helpful comments.

[1] O. Reynolds, Proc. R. Soc. Lond. A **34**, 84 (1883).
[2] M. Fitzgerald, Phys. Today **57**, No. 2, 21 (2004).
[3] P. G. Drazin and W. H. Reid, *Hydrodynamic Stability* (Cambridge University Press, Cambridge, England, 1980).
[4] A. G. Darbyshire and T. Mullin, J. Fluid Mech. **289**, 83 (1995).
[5] C. Grebogi, E. Ott, and J. A. Yorke, Phys. Rev. Lett. **57**, 1284 (1986).
[6] W. L. Ditto *et al.*, Phys. Rev. Lett. **63**, 923 (1989).
[7] H. Faisst and B. Eckhardt, Phys. Rev. Lett. **91**, 224502 (2003).
[8] H. Wedin and R. R. Kerswell, J. Fluid Mech. **508**, 333 (2004).
[9] B. Hof, A. Juel, and T. Mullin, Phys. Rev. Lett. **91**, 244502 (2003).
[10] T. Mullin and J. Peixinho, in *Proceedings of the IUTAM Symposium on Laminar-Turbulent Transition Bangalore, India, 2004*, edited by R. Govindarajan and R. Narasimha (Springer, Bangalore, 2006), p. 45.
[11] I. J. Wygnanski and F. H. Champagne, J. Fluid Mech. **59**, 281 (1973).
[12] G. Han, A. Tumin, and I. J. Wygnanski, J. Fluid Mech. **419**, 1 (2000).
[13] D. A. Gilbrech and J. C. Hale, *Developments in Mechanics* (Pergamon, Case, 1965), Vol. II, p. 3.
[14] B. Hof *et al.*, Science **305**, 1594 (2004).
[15] K. R. Sreenivasan, Acta Mech. **44**, 1 (1982).
[16] J. Laufer, in *Mizellaneen der angewandten mechanik*, edited by M. Schaefer (Academic-Verlag, Berlin, 1962), p. 166.
[17] M. Sibulkin, Phys. Fluids **5**, 280 (1962).
[18] S. Bottin and H. Chaté, Eur. Phys. J. B **6**, 143 (1998).
[19] S. H. Strogatz, *Nonlinear Dynamics and Chaos* (Perseus, New York, 1994).
[20] J. J. Hegseth, Phys. Rev. E **54**, 4915 (1996).
[21] S. Bottin *et al.*, Europhys. Lett. **43**, 171 (1998).
[22] O. Dauchot and N. Vioujad, Eur. Phys. J. B **14**, 377 (2000).
[23] H. Faisst and B. Eckhardt, J. Fluid Mech. **504**, 343 (2004).
[24] Y. Do and Y.-C. Lai, Phys. Rev. E **71**, 046208 (2005).

PHYSICS OF FLUIDS **25**, 111702 (2013)

Transition to turbulence in slowly divergent pipe flow

Jorge Peixinho[1,2] and Hugues Besnard[1]
[1]*Laboratoire Ondes et Milieux Complexes, CNRS and Université du Havre, 53 rue de Prony, 76600 Le Havre, France*
[2]*Fluid Engineering Laboratory, Department of Mechanical Engineering, University of Tokyo, 7-3-1 Hongo, Tokyo 113-8656, Japan*

(Received 30 July 2013; accepted 31 October 2013; published online 27 November 2013)

The results of a combined experimental and numerical study of the flow in slowly diverging pipes are presented. Interestingly, an axisymmetric conical recirculation cell has been observed. The conditions for its existence and the length of the cell are simulated for a range of diverging angles. There is a critical velocity for the appearance of this state. When the flow rate increases further, a subcritical transition for localized turbulence arises. The transition and relaminarization experiments described here quantify the extent of turbulence. The findings suggest that the transition scenario in slowly diverging pipes is a combination of stages similar to those observed in sudden expansions and in straight circular pipe flow. © *2013 AIP Publishing LLC*. [http://dx.doi.org/10.1063/1.4833436]

The flow in slowly diverging pipes, i.e., cylindrical pipes of slowly increasing diameter along the pipe axis, as depicted in Figure 1(a), is not well documented despite some fundamental and practical features. This flow arises in microfluidics when transferring liquid using pipettes and in physiological flows in veins when blood rushes from organs and tissues towards the heart. Knowledge of the nature of this flow can also be useful in the context of burner-combustion systems, jet engine exhaust, thrust-vectoring nozzles, and flows of confined jets.[1–3]

The general two-dimensional problem of flow stability between two plane walls meeting at a source point with an angle is known as the Jeffery-Hamel problem. There are several theoretical and numerical developments where bifurcations have been found[4–9] and all these works indicate a rich and diverse set of solutions even for small diverging angles. Recently, Putkaradze and Vorobieff[10] observed, using particle image velocimetry, the multiple vortex flow regime predicted by Kerswell *et al.*[5]

A large body of research has dealt with two-dimensional sudden channel expansions, with sharp 90° corners. In the case of a 1:3 sudden expansion flow, it was shown[11,12] that the asymmetry arises at a critical Reynolds number through a pitchfork symmetry breaking bifurcation. Fearn *et al.*[12] were able to measure the degree of asymmetry due to small imperfections of the experimental apparatus and compared it with numerical results.

The present work considers the case of an axisymmetric circular pipe that is slowly expanding. Solutions for the laminar flow in slightly tapered cylinders assuming the lubrication approximation ($D - d \ll L$) can be found in Bird *et al.*[13] in the form of corrected expressions for the velocity profiles. Here d and D are the inlet and outlet diameters of the divergent section and L is its length (see Figure 1(a)). The diverging angle, α, refers to the half angle of the diffuser. When the diameter varies slowly, the axial velocity profile, which depends on the local diameter, conserves its parabolic shape. However, in the diverging section, the centerline velocity scales as $1/x^2$, where x is the axial position, and a fluid particle experiences a rapid deceleration. Additionally, in laminar flow, the pressure along the diverging section decreases rapidly.[14]

The transition to turbulence in the limit case of a 90° (abrupt) 1:2 circular pipe expansion was studied by Sreenivasan and Strykowski,[15] Latornell and Pollard,[16] and others. The steady flow becomes unstable and a periodic time-dependent state was observed at $Re \sim 750$ and around 1500. Re is the Reynolds number based on d. In a modern investigation using high resolution magnetic

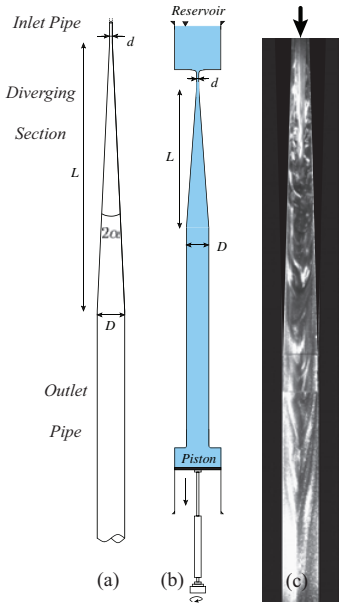

FIG. 1. Schematics of the diverging pipe, the experiment, and a flow visualization photograph. (a) Basic geometry, (b) sketch of the experimental setup drawn up to scale, and (c) flow visualization photograph for $Re = 1000$ in the diverging pipe ($\alpha = 2^\circ$, $\beta = L/d = 128.88$, and $D/d = 8.79$). The flow is from top to bottom and the horizontal lines on the photograph indicate the connection between the divergent section and the expansion (enhanced online). [URL: http://dx.doi.org/10.1063/1.4833436.1]

resonance imaging, Mullin *et al.*[17] found a sharp onset of asymmetry in the downstream flow at $Re = 1140$. Recently, numerical simulations[18,19] confirmed the previous experimental results and showed that the flow is unstable to infinitesimal perturbation for $Re = 3273$. The exact nature of the first instability is unclear since imperfections are likely to produce disturbance that can grow and lead to multiple solutions both stationary and time-dependent.

The stability of the axisymmetric slowly diverging pipe flow has been investigated in a numerical work[20] solving a multigrid Poisson equation for the base flow and partial differential equations for the flow stability in a diverging pipe ($\alpha = 1.5^\circ$, $L/d = 120$, and $D/d \approx 7.3$), and indicate that the flow is linearly unstable from $Re = 150$. In another numerical simulation[21] it is found that the flow separation occurs for Re less than about 2000. The purpose of the present experimental study is to add new quantitative data in order to clarify these findings.

A number of investigations in straight pipes with a axisymmetric constriction have been carried out numerically[22] and in experiments[23,24] as an idealization of a stenosed artery. In this situation, the velocity profile at the inlet of the divergent section is almost flat, the flow in this divergent pipe ($\alpha \approx 45^\circ$, $L \approx D$, and $D/d = 2$) exhibits a laminar recirculation region, and the subcritical transition to turbulence[22] occurs at $Re = 361$.

The remaining part of this paper presents the experimental apparatus. The results of two-dimensional simulations, as well as an investigation of the stability of the recirculation cells, are given in the following paragraphs. Later, the dynamics of the turbulent patches is described and these are tested via a series of relaminarization experiments. Conclusions are drawn in the end.

The experiments consist of flow visualization in slowly diverging axisymmetric pipes. A schematic of the experimental setup is given in Figure 1(b). It is composed of a vertical pipe made of acrylic. The flow is controlled using a syringe pump (TSE Systems Model 540230) together with 100 ml glass syringes. The device pulls the fluid at a constant mass flux along the pipe. Hence, even if the motion becomes turbulent, the mass flux through the pipe is unaffected so that Re remains constant. The maximum pulling velocity corresponded to $Re = 4000$.

The slowly diverging acrylic pipe used here has half-angle, α, of 2° (or $\pi/90$ rad) over a length $L = 128.88d = 275.8$ mm. The inlet diameter was $d = 2.14 \pm 0.1$ mm, the outlet diameter was $D = 18.8 \pm 0.1$ mm, and there was an imperfection due to the fitting of the outlet section. Downstream of the divergent section, a straight pipe section extended for $320d$.

The inlet has a straight section of diameter d over $10d$ in order to obtain a fully developed Poiseuille flow. The development is facilitated by a smooth contraction between the inlet and the reservoir. For flow visualization, 4 ml of Kalliroscope, a suspension of reflective flakes, was added to two liters of degassed water. A vertical light sheet was formed in the center plane of the flow, and a camera was used to record the dynamics of the flow. An example of the flow visualization is shown in Figure 1(c). The Reynolds number is defined by $Re = Ud/\nu$, where U is the mean flow rate and ν is the kinematic viscosity. The temperature of the fluid is taken into account in the calculation of Re. The other parameters of the diverging pipe are the expansion ratio, $E = D/d$, between the outlet and inlet diameters and the non-dimensional length of the diverging section: $\beta = L/d$. For the 2° pipe, $(E, \beta) = (8.79, 128.88)$.

The base flow in slowly diverging pipes is a parabolic velocity profile and the axial velocity on the centerline decreases along the divergent axes. As the flow rate increases or as the diverging angle increases, a recirculation cell is observed close to the walls and its extent depends on Re. In practice, the cell is thin and difficult to measure because of the azimuthal curvature of the outer walls. An example of time-exposure photography is presented in Figure 2(a). The fluid particle paths around the centerline appear as continuous lines, whereas fluid particle paths close to the walls appear as dotted lines indicating that they move at a much slower pace.

The axisymmetric flow is reproduced in numerical simulations of time-dependent Navier-Stokes equations using a two dimensional axisymmetric finite element code (COMSOL Multiphysics). At the inlet, the velocity profile is parabolic over $10d$. In the downstream section, the mesh consists of several blocks and is sufficiently long, typically $100d$, so that Poiseuille flow is recovered. The outlet boundary condition is constant pressure. The number of elements along the divergent section and the outlet section depends on α and E and is around one million. The numerical simulations indicate that the recirculation appears at a finite Re in the corner between the divergent section and the outlet section. As the flow rate increases, the recirculation cell grows both upstream and downstream. The

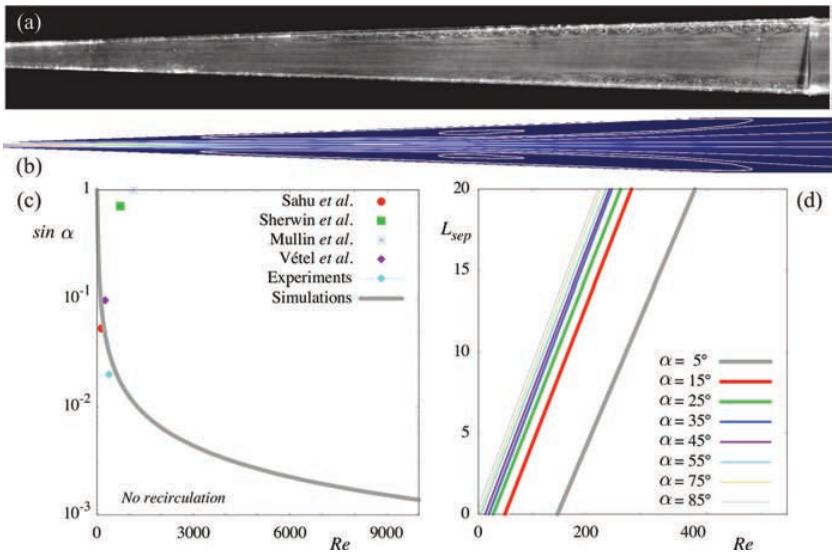

FIG. 2. Laminar flow in a slowly divergent pipe. (a) Time-exposure photograph for $Re = 200$. (b) Numerical simulations of velocity streamlines for $Re = 600$. (c) Onset of axisymmetric recirculation cell as predicted from numerical simulations in terms of $\sin\alpha$ as a function of Re. The points represent the critical Re of transition to turbulence for the current and previous studies.[17,20,22,24] (d) Numerical predictions of the separation length, L_{sep}, versus Re for different α.

calculated streamlines as well as axial velocity magnitude are given in Figure 2(b). The flow can be described as a confined jet which expands downstream and the recirculation cell is long and thin. Notice that the velocity profile exhibits a flow reversal containing inflection points which can lead to Kelvin-Helmholtz instability.

The onset for the growth of the recirculation cells can be tracked using numerical simulations for a range of α, β, and E. For $\alpha \approx 20$ up to 90° ($\sin\alpha \approx 0.34$ up to 1), the recirculation cell is always present. As α decreases, there is a critical Re for the onset of the recirculation cell which grows rapidly as shown in Figure 2(c). Eventually, when α tends to zero, the critical Re becomes large as suggested by linear stability calculations of circular pipe flow of constant diameter.[25] The threshold for the appearance of the recirculation cell is compared to data points for transition to turbulence from the literature.[17,20,22,24] Calculations were performed changing α (or β) keeping E constant from 2 to 10 and the critical Re for the onset of recirculation cell varies by less than 5%.

In the regions around the outlet of the divergent section, the pressure close to the wall and the deceleration of the fluid particle lead to the onset of the recirculation cell. Once the cell appears, it grows linearly with Re. In Figure 2(d), the axial length of the recirculation bubble, L_{sep}, called the separation length, deduced from the positions of zero wall shear stress calculations is presented as a function of Re for different α. Our numerical simulation for $\alpha = 85^\circ$ agree quantitatively with the experiments of Latornell and Pollard[16] on sudden expansion ($L_{sep} = 0.096Re$) and previous numerical works.[18,23]

In the case of abrupt expansions in two-dimensional channels, several authors refer to the "Coanda" effect[3,12] when the initial symmetric flow becomes asymmetric. Specifically, one of the recirculating cells becomes larger and a new time-independent flow is observed. This sequence of events leads to the breaking of the symmetry of the flow in agreement with the ideas of bifurcation theory. In the present case of axisymmetric flow there is a single recirculation cell in contrast with the two-dimensional channels where there is one cell behind each step. Sanmiguel-Rojas and Mullin[19] showed using three-dimensional numerical simulations that the axisymmetric state is sensitive to small imperfections. Depending on the amplitude of a small distortion added to the parabolic inlet flow, the flow change to asymmetric or disordered time-dependent state. Our numerical simulations are two-dimensional axisymmetric. In the experiments, the time-independent asymmetric states were not clearly observed because of azimuthal curvature of the outer walls (see Figure 2(a)). At higher Re, the cell is found to be sensitive to natural disturbances of the system. These imperfections are related to a distortion parameter in a complicated manner and are the source instabilities which lead to the formation of super-critical turbulent patches.

With a further increase of the flow rate, the recirculating bubble breaks down into localized turbulent patches as the one depicted in Figure 1(c). These localized turbulent patches have some similarities with the so-called localized puffs observed in cylindrical straight pipe flow.[27] Puffs seem to have a definite length for a given Re, an active core of high turbulence intensity and a decaying wave at the front. In the diverging pipe outlet section, turbulent patches appear in the divergent section and extend over many diameters. There, the downstream Reynolds number, based on the outlet diameter, is too small to sustain turbulence and decaying turbulence is observed. Contrary to puffs, the turbulent patch does not travel along the pipe. Their origin is the breakdown of the recirculation cell. However, they do have a definite length for a given Re, an active core of high turbulence intensity and a decaying wave at the front.

In Figure 3, space-time diagrams of laminar flow (Figure 3(a)) and turbulent patches (Figures 3(b) and 3(c)) are produced by converting the brightness of the flow visualization photographs along the flow axis and stacking the different lines corresponding to different times. $x/d = 0$ represents the inlet of the divergent section. The dimensionless time, t, used here is defined as $t = ft^*$ where f is the image acquisition frequency (20 Hz) and t^* is the time (in seconds). In Figure 3(b), the puff is represented by fluctuating dark areas in the middle of the diagrams: $60 < x/d < 100$. The comparison of the diagrams for $Re = 800$ (Figure 3(b)) and $Re = 2400$ (Figure 3(c)) suggests that the length of the turbulent patch increases. In Figure 3(b), the clear streaks beyond $x/d = 90$ indicate that constant bright regions are moving at constant velocity. The velocity is given by the slope of the streak. The appearance of the constant brightness streaks is used to detect the decaying wave and the leading edge of the turbulent patches. More information about the relation

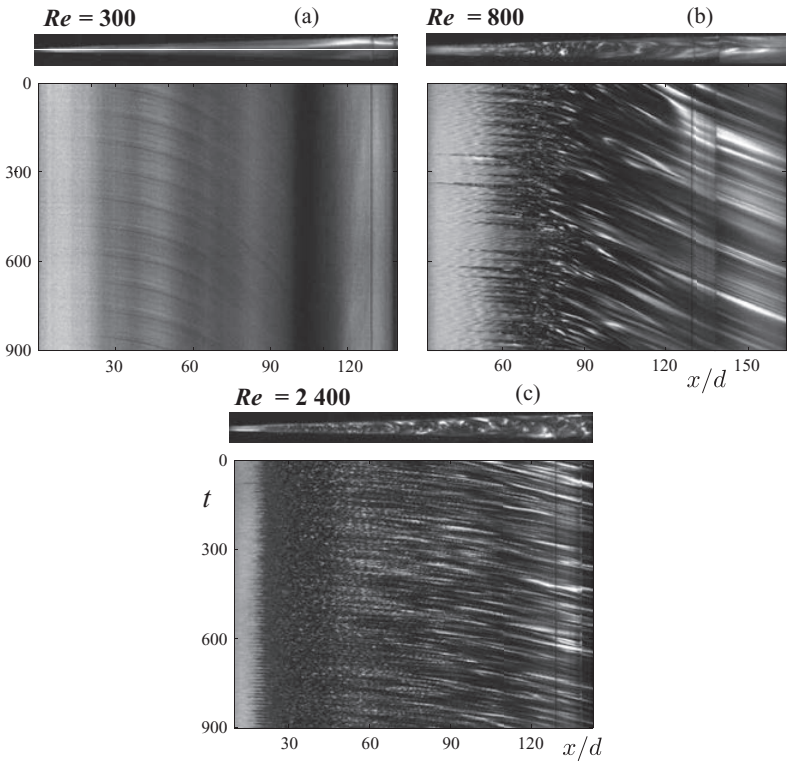

FIG. 3. Photographs of the flow and space-time diagrams for different Re. The photographs are on top of the diagrams, which are based on the brightness along the flow axis. (a) Laminar flow at $Re = 300$, (b) localized turbulent patch at $Re = 800$, and (c) turbulent patch at $Re = 2400$.

between reflected light intensity and velocity field can be obtained from Abcha *et al.*[26] Figure 4(a) presents the positions of the leading and trailing edges of the turbulent patch as a function of Re. The error bars represent the fluctuation of the positions of the leading and trailing edges. The trailing edge is sharper than the leading edge (see Figures 4(b)–4(d)). The boundary between the decaying wave and the laminar flow is tenuous as in the case of puffs.[27] As Re increases, the extend of the

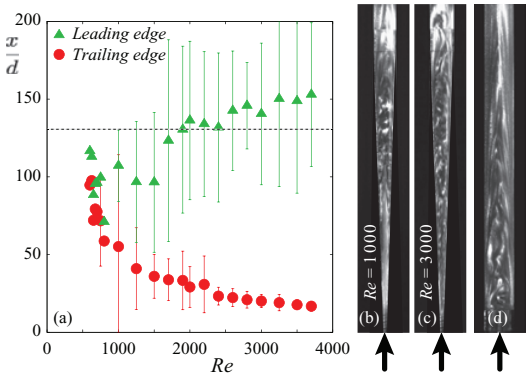

FIG. 4. Length of the turbulent patch in the slowly diverging pipe. (a) Position of the leading and trailing edges of the turbulent patch as a function of Re. The dashed line represents the end of the diverging section at $\beta = x/d = 128.88$. (b) Flow visualization of a turbulent patch at $Re = 1000$, (c) flow visualization of a turbulent patch at $Re = 3000$ in the divergent section, and (d) its decaying front wave in the outlet section.

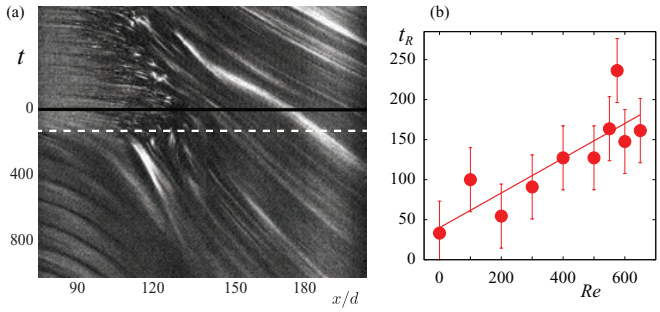

FIG. 5. Relaminarization experiments. (a) Space-time diagram of a relaminarization experiment from a localized turbulent patch: $Re_0 = 800$ to $Re = 400$, the black line represents the moment of the reduction of Re and the dashed white line the estimated relaminarization time when no disordered motion is observed. (b) Relaminarization time, t_R, versus Re.

turbulent patch increases. The position of the trailing edge asymptotes towards a positive value as the turbulent patch cannot propagate beyond the inlet of the divergent section. For large Re the position of the leading edge continues to increase. The results of Figure 4 are reminiscent of Wygnanski and Champagne[27] measurements describing the growth of turbulent puffs in uniform pipes suggesting that the turbulent patches observed here may contain solutions similar to those observed in pipe flow.

It is expected that the position of the leading edge will increase as Re increases. Eventually as the turbulent patch grows, a puff-slug transition[27,28] is likely to take place where the stationary turbulent patch will split. This process is found to be vortex shedding via a Kelvin-Helmholtz mechanism from wall-attached shear layers.

Further increase of Re means a fully developed turbulent flow field. There are many reports on turbulent flow properties in rectangular diffusers suggesting that the manipulation of the recirculation can lead to changes in the conversion of mean-flow kinetic energy to pressure.[29,30] A recent review on turbulent flow in diffusers and direct numerical simulation of the turbulence statistics and coherent structures can be found in the paper by Lee *et al.*[31]

In order to quantify further the turbulent patch regime, relaminarization experiments[32] were performed where turbulent patches are generated and its decay is observed back to laminar as Re was reduced. During the decay of the turbulent patch, a laminar liquid jet going through the turbulent patch sets in quickly and induces the recirculation flow close to the wall. Wavy patterns are observed. The liquid jet seems to fold like a viscous thread. Similar oscillations of the liquid jet in a divergent section were also observed in microfluidic experiments.[33]

Our strategy was to generate a turbulent puff at $Re_0 = 800$. This turbulent patch was stable (see Figure 3(b)) and is considered as a natural state or attractor of the system. The reduction in Re was almost instantly and achieved by reducing the syringe pump velocity. The relaminarization was monitored through spatio-temporal diagrams. A typical example is presented in Figure 5(a). The decay time was estimated from the moment of the reduction in Re ($t = 0$) to the time where no disordered motion is observed within the translating disordered patch ($t = t_R$). In the example presented in Figure 5(a), $t = 0$ and $t = t_R$ are represented as continuous and dashed lines, respectively. The oblique streaks are related to the translation velocity along the pipe axis. The time for the disordered patch to decay, t_R, was extracted from the diagrams and are shown in Figure 5(b). The straight line is a linear fit of t_R indicating that the lifetime of the turbulent patch increases linearly with Re. A divergence of timescales is expected close to transition points.[32] Our experimental setup is limited to a moderate range of t_R. The data suggest that a critical point for sustained localized turbulence may be found at Re between 600 and 800 and is reported in Figure 2(c).

This work presented a study about the flow in slowly diverging pipe. At low flow rate, no recirculation bubble is observed. For larger flow rate, stable laminar recirculation bubble is observed and extends downstream. The results of our computation predict the onset of the recirculation and the extent of the recirculation bubble for a range of parameters.

With further increase of the flow rate, a domain of unstable turbulent patches is uncovered. The extent of the turbulent patch is reported. A future direction of our research will be to investigate the statistical properties of this localized turbulence and the puff-slug transition as the turbulent puff here does not travel along the pipe.

The financial support of the Japan Society for the Promotion of Science and the Région Haute-Normandie are acknowledged. We also thank A. P. Willis, I. Mutabazi, and J. E. Wesfreid for discussions.

[1] A. Craya and R. Curtet, "Sur l'évolution d'un jet en espace confiné," C. R. Acad. Sci. **241**(8), 621–622 (1955).
[2] A. Nahum and A. Seifert, "On the application of confined twin-jet instability to micro-mixing enhancement," Phys. Fluids **18**, 064107 (2006).
[3] C. Y. Soong, P. Y. Tzeng, and C. D. Hsieh, "Numerical investigation of flow structure and bifurcation phenomena of confined plane twin-jet flows," Phys. Fluids **10**(11), 2910–2921 (1998).
[4] M. Hamadiche, J. Scott, and D. Jeandel, "Temporal stability of Jeffery-Hamel flow," J. Fluid Mech. **268**, 71–88 (1994).
[5] R. R. Kerswell, O. R. Tutty, and P. G. Drazin, "Steady nonlinear waves in diverging channel flow," J. Fluid Mech. **501**, 231–250 (2004).
[6] I. J. Sobey and P. G. Drazin, "Bifurcations of two-dimensional channel flows," J. Fluid Mech. **171**, 263–287 (1986).
[7] S. R. Stow, P. W. Duck, and R. E. Hewitt, "Three-dimensional extensions to Jeffery-Hamel flow," Fluid Dyn. Res. **29**, 25–46 (2001).
[8] P. E. Haines, R. E. Hewitt, and A. L. Hazel, "The Jeffery-Hamel similarity solution and its relation to flow in a diverging channel," J. Fluid Mech. **687**, 404–430 (2011).
[9] G. Swaminathan, K. C. Sahu, A. Sameen, and R. Govindarajan, "Global instabilities in diverging channel flows," Theor. Comput. Fluid Dyn. **25**, 53–64 (2011).
[10] V. Putkaradze and P. Vorobieff, "Instabilities, bifurcations, and multiple solutions in expanding channel flows," Phys. Rev. Lett. **97**, 144502 (2006).
[11] F. Durst, A. Melling, and J. H. Whitelaw, "Low Reynolds number flow over a plane symmetric sudden expansion," J. Fluid Mech. **64**, 111–128 (1974).
[12] R. M. Fearn, T. Mullin, and K. A. Cliffe, "Nonlinear flow phenomena in a symmetric sudden expansion," J. Fluid Mech. **211**, 595–608 (1990).
[13] R. B. Bird, R. C. Armstrong, and O. Hassager, *Dynamics of Polymeric Liquids* (John Wiley & Sons, Hoboken, 1987).
[14] S. Rosa and F. T. Pinho, "Pressure drop coefficient of laminar Newtonian flow in axisymmetric diffusers," Int. J. Heat Fluid Flow **27**, 319–328 (2006).
[15] K. R. Sreenivasan and P. J. Strykowski, "An instability associated with a sudden expansion in pipe flow," Phys. Fluids **26**(10), 2766–2768 (1983).
[16] D. J. Latornell and A. Pollard, "Some observations on the evolution of shear layer instabilities in laminar flow through axisymmetric sudden expansions," Phys. Fluids **29**(9), 2828–2835 (1986).
[17] T. Mullin, J. R. T. Seddon, M. D. Mantle, and A. J. Sederman, "Bifurcation phenomena in the flow through a sudden expansion in a circular pipe," Phys. Fluids **21**, 014110 (2009).
[18] C. D. Cantwell, D. Barkley, and H. M. Blackburn, "Transient growth analysis of flow through a sudden expansion in a circular pipe," Phys. Fluids **22**, 034101 (2010).
[19] E. Sanmiguel-Rojas, C. del Pino, and C. Gutiérrez-Montez, "Global mode analysis of a pipe flow through a 1:2 axisymmetric sudden expansion," Phys. Fluids **22**, 071702 (2010).
[20] K. C. Sahu and R. Govindarajan, "Stability of flow through a slowly diverging pipe," J. Fluid Mech. **531**, 325–334 (2005).
[21] E. M. Sparrow, J. P. Abraham, and W. J. Minkowycz, "Flow separation in a diverging conical flow: Effect of Reynolds number and divergence angle," Int. J. Heat Mass Transfer **52**, 3079–3083 (2009).
[22] S. J. Sherwin and H. M. Blackburn, "Three-dimensional instabilities and transition of steady and pulsatile axisymmetric stenotic flows," J. Fluid Mech. **333**, 297–327 (2005).
[23] M. D. Griffith, T. Leweke, M. C. Thompson, and K. Hourigan, "Steady inlet flow in stenotic geometries: Convective and absolute instabilities," J. Fluid Mech. **616**, 111–133 (2008).
[24] J. Vétel, A. Gaton, D. Pelletier, and M.-I. Farinas, "Asymmetry and transition to turbulence in a smooth axisymmetric constriction," J. Fluid Mech. **607**, 351–386 (2008).
[25] A. Meseguer and L. N. Trefethen, "Linearized pipe flow to Reynolds number 10^7," J. Comput. Phys. **186**, 178–197 (2003).
[26] N. Abcha, N. Latrache, F. Dumouchel, and I. Mutabazi, "Quantitative relation between reflected light intensity by Kalliroscope flakes and velocity field in the Taylor-Couette flow system," Exp. Fluids **45**, 85–94 (2008).
[27] I. J. Wygnanski and F. H. Champagne, "On transition in a pipe. Part 1. The origin of puffs and slugs and the flow in a turbulent slug," J. Fluid Mech. **59**, 281–335 (1973).
[28] Y. Duguet, A. P. Willis, and R. R. Kerswell, "Slug genesis in cylindrical pipe flow," J. Fluid Mech. **663**, 180–208 (2010).
[29] H. Schneider, D. A. Von Terzi, H.-J. Bauer, and W. Rodi, "A mechanism for control of turbulent separated flow in rectangular diffusers," J. Fluid Mech. **687**, 584–594 (2011).
[30] A. H. Herbst, P. Schlatter, and D. S. Henningson, "Simulations of turbulent flow in a plane asymmetric diffuser," Flow, Turbul. Combust. **79**, 275–306 (2007).
[31] J. Lee, S. J. Jang, and H. J. Sung, "Direct numerical simulations of turbulent flow in a conical diffuser," J. Turbul. **13**(30), 1–29 (2012).
[32] J. Peixinho and T. Mullin, "Decay of turbulence in pipe flow," Phys. Rev. Lett. **96**, 094501 (2006).
[33] T. Cubaud and T. G. Mason, "Folding of viscous threads in diverging microchannels," Phys. Rev. Lett. **96**, 114501 (2006).

J. Fluid Mech. (2015), *vol.* 771, R2, doi:10.1017/jfm.2015.207

JFM RAPIDS
journals.cambridge.org/rapids

Localised turbulence in a circular pipe flow with gradual expansion

Kamal Selvam[1], **Jorge Peixinho**[1,†] **and Ashley P. Willis**[2]

[1]Laboratoire Ondes et Milieux Complexes, CNRS & Normandie Université, 53 rue de Prony, 76600 Le Havre, France

[2]School of Mathematics and Statistics, University of Sheffield, Sheffield S3 7RH, UK

(Received 2 March 2015; revised 27 March 2015; accepted 30 March 2015)

We report the results of three-dimensional direct numerical simulations for incompressible viscous fluid in a circular pipe flow with a gradual expansion. At the inlet, a parabolic velocity profile is applied together with a constant finite-amplitude perturbation to represent experimental imperfections. Initially, at low Reynolds number, the solution is steady. As the Reynolds number is increased, the length of the recirculation region near the wall grows linearly. Then, at a critical Reynolds number, a symmetry-breaking bifurcation occurs, where linear growth of asymmetry is observed. Near the point of transition to turbulence, the flow experiences oscillations due to a shear layer instability for a narrow range of Reynolds numbers. At higher Reynolds numbers, the recirculation region breaks into a turbulent state which remains spatially localised and unchanged when the perturbation is removed from the flow. Spatial correlation analysis suggests that the localised turbulence in the gradual expansion possesses a different flow structure from the turbulent puff of uniform pipe flow.

Key words: instability, transition to turbulence

1. Introduction

In axisymmetric sudden-expansion pipe flow, bifurcations of flow patterns have been studied experimentally (Sreenivasan & Strykowski 1983; Latornell & Pollard 1986; Hammad, Ötügen & Arik 1999; Mullin *et al.* 2009) and numerically (Sanmiguel-Rojas, Del Pino & Gutiérrez-Montes 2010; Sanmiguel-Rojas & Mullin 2012). In these studies, flow separation after the expansion and reattachment downstream leads to the formation of a recirculation region near the wall. Its extent grows linearly as the flow velocity is increased. Numerical simulations and experimental results have shown that the recirculation region breaks symmetry once a critical Reynolds

† Email address for correspondence: jorge.peixinho@univ-lehavre.fr

number is exceeded. Here, the Reynolds number Re is defined as $Re = Ud/\nu$, where U is the bulk flow velocity, d is the inlet diameter and ν is the kinematic velocity. In experiments, the recirculation region loses symmetry at $Re \simeq 1139$ (Mullin *et al.* 2009) and then breaks to form localised turbulence which tends to remain in the same spatial position (Sreenivasan & Strykowski 1983). In terms of global stability analysis, Sanmiguel-Rojas *et al.* (2010) have shown that the symmetry breaking occurs after a critical Reynolds number of ≈3273. The reason for the early occurrence of transition is believed to be experimental imperfections. Numerical simulations with an applied finite-amplitude perturbation (Sanmiguel-Rojas & Mullin 2012) found the transition to turbulence to occur at $Re \gtrsim 1500$, which depends upon the amplitude of the perturbation.

The goal of the present investigation is to numerically model the gradual expansion (diverging) pipe flow with an imperfection added to the system that could trigger early transition to turbulence. The long-term motivation of this study is to understand the effect of the diverging angle on the transition to turbulence. In § 2, the numerical method and its validation are presented. In § 3, the results for the asymmetric growth of the recirculation are discussed, along with the oscillation of the flow, the time evolution of the localised turbulence and observations of decay of the turbulent structure.

2. Numerical method

The solutions are obtained by solving the unsteady three-dimensional incompressible Navier–Stokes equation for a viscous Newtonian fluid:

$$\boldsymbol{\nabla} \cdot \boldsymbol{v} = 0, \tag{2.1}$$

$$\frac{\partial \boldsymbol{v}}{\partial t} + \boldsymbol{v} \cdot \boldsymbol{\nabla} \boldsymbol{v} = -\boldsymbol{\nabla} P + \frac{1}{Re} \nabla^2 \boldsymbol{v}, \tag{2.2}$$

where $\boldsymbol{v} = (u, v, w)$ and P denote the scaled velocity vector and pressure respectively. Equations (2.1) and (2.2) were non-dimensionalised using the inlet pipe diameter, d, for the length scale and the bulk velocity at the inlet, U, for the velocity scale. The time scale and the pressure scale are therefore $t = d/U$ and ρU^2, where ρ is the density of the fluid. The equations are solved with the boundary conditions:

$$\boldsymbol{v}(\boldsymbol{x}, t) = 2(1 - 4r^2)\boldsymbol{e}_z, \quad \boldsymbol{x} \in \text{Inlet}, \tag{2.3}$$

$$\boldsymbol{v}(\boldsymbol{x}, t) = 0, \quad \boldsymbol{x} \in \text{Wall}, \tag{2.4}$$

$$P\boldsymbol{n} - \boldsymbol{n} \cdot \boldsymbol{\nabla} \boldsymbol{v}(\boldsymbol{x}, t)/Re = 0, \quad \boldsymbol{x} \in \text{Outlet}, \tag{2.5}$$

corresponding to a fully developed Hagen–Poiseuille flow (2.3) at the inlet, no-slip (2.4) at the walls and an open boundary condition (2.5) at the outlet of the pipe, $\boldsymbol{e}_z$ is the unit vector in the axial direction and r is the cylindrical radius. Equation (2.5) enforces Neumann boundary conditions in weak sense for the velocity components, which minimises the possibility of numerical oscillations and reflections of outgoing waves, where $\boldsymbol{n}$ is the normal surface vector directed out of the computational domain. The equations were solved using an open source code nek5000 developed by Fischer *et al.* (2008). Spatial discretisation is based on the spectral-element method using Lagrange polynomials. The equations are reduced to a weak form and discretised in space by Galerkin approximation. Here, Nth-order Lagrange polynomial interpolants on Gauss–Lobatto–Legendre points were chosen as the basis for the

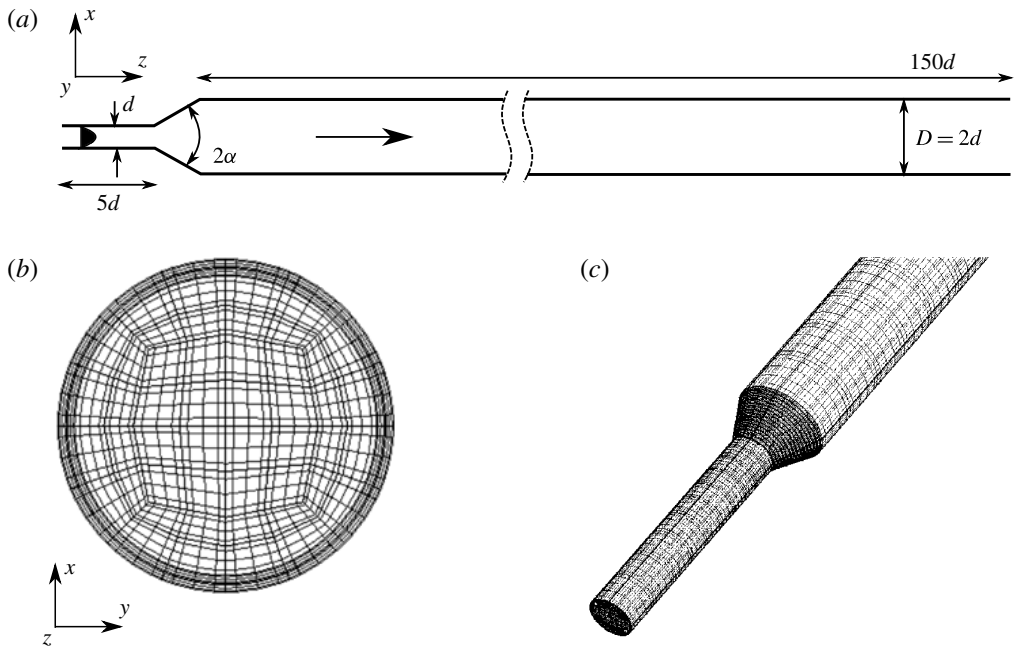

FIGURE 1. The spectral-element mesh used in the present study with a divergent angle of $\alpha = 26.57°$. (*a*) Sketch of the domain, (*b*) cross-section of the mesh (the dark lines represent the elements and the grey lines represent the Gauss–Lobatto–Legendre points) and (*c*) a three-dimensional view of the mesh near the diverging section. The mesh is made of $K = 14\,400$ elements.

velocity space, and similarly for the pressure space. In all the simulations $\mathbb{P}_N - \mathbb{P}_N$ formulations were implemented, which denotes that the same polynomial order was used for both velocity and pressure. The time-stepping in nek5000 is semi-implicit in which the viscous terms of the Navier–Stokes equations are treated implicitly using third-order backward differentiation and the nonlinear terms are treated by a third-order extrapolation scheme (Maday, Patera & Rønquist 1990; Fischer *et al.* 2008).

Figure 1 shows the geometry of the divergent pipe along with the mesh. It consists of three parts: (i) the inlet, (ii) the diverging section and (iii) the outlet. The velocity field is simulated in the Cartesian coordinate system (x, y, z). The expansion ratio is $E = D/d = 2$, where D is the outlet pipe diameter. The length of the divergent section is kept constant in this study and of length d, which leads to a divergence half-angle of $\alpha = 26.57°$. The length of the inlet pipe is $5d$ and the outlet pipe length is $150d$.

The mesh was developed using hexahedral elements with a non-uniform growth rate. It contains 80 elements with refinement near the wall in the (x, y) cross-section and 180 elements in the z direction. A refinement has been applied in the diverging section, as shown in figure 1(*c*), in order to resolve the flow separation. The streamwise extent of the elements increases along z in the outlet section. The total number of grid points in the simulation is approximately KN^3, where K is the number of elements and N is the polynomial order. The flow was initialised with fully developed Poiseuille flow in the inlet section, and each simulation was computed using 512 cores. Table 1 shows the length of the recirculation region for different orders of polynomial at $Re = 1000$. The mesh convergence study was carried out by changing the polynomial order N

N	Reattachment position z_r	Viscous drag
3	43.68	0.8430
4	43.65	0.3566
5	43.58	0.3419
6	43.59	0.3418
7	43.58	0.3419

TABLE 1. Convergence study, changing the order of the polynomial N. Here, z_r is the non-dimensional length of the recirculation region in the pipe for $Re = 1000$.

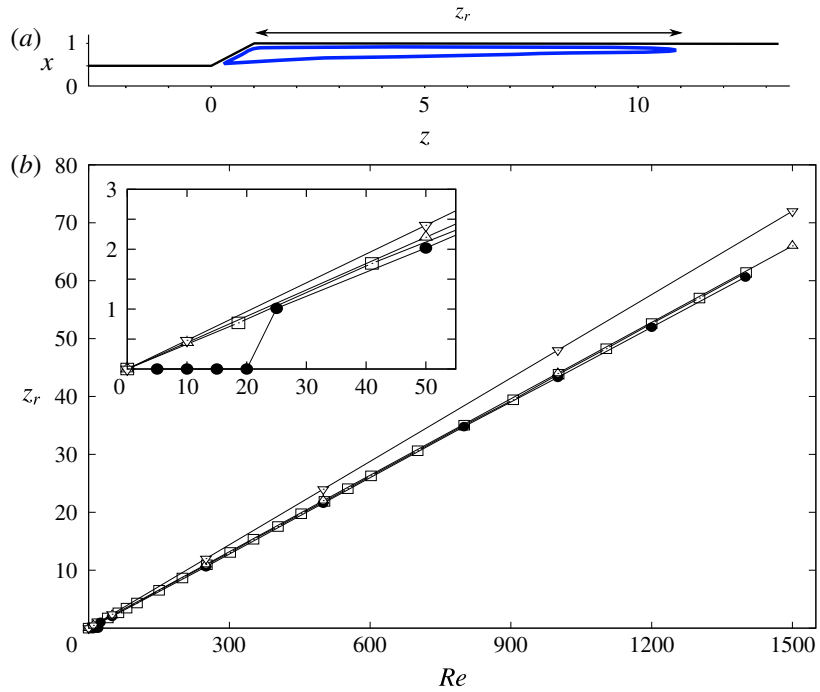

FIGURE 2. (*a*) Streamline of the recirculation region of length z_r inside the diverging pipe at $Re = 300$, (*b*) recirculation region length, z_r, with respect to Re. Here, ● corresponds to best-fit proportionality given by $2z_r = 0.0866Re$ for the present case, □ corresponds to $2z_r = 0.0874Re$ (Cantwell, Barkley & Blackburn 2010), and △ and ▽ correspond to the experimental results (Latornell & Pollard 1986; Hammad *et al.* 1999) $2z_r = 0.088Re$ and $2z_r = 0.096Re$ respectively for sudden expansions.

of the Lagrange polynomial of the spectral elements. The observations used to assess convergence are the flow reattachment point, z_r, and the viscous drag, $(\rho U^2/2)\mathscr{A}_w C_f$, where $\mathscr{A}_w$ is the surface area of the outlet pipe wall and C_f is the friction coefficient. The length of the recirculation region depends sensitively on the resolution of the separated shear layer, particularly near the separation point. The polynomial order of $N = 5$ is sufficient to resolve the flow accurately. These values of N and the mesh have been used in all the following simulations; this corresponds to $KN^3 \approx 1.8 \times 10^6$ grid points.

To validate the simulations further at higher Reynolds number, the growth of the recirculation region as a function of the Reynolds number is shown in figure 2.

The simulations show that the extent of the recirculation region is of the form $2z_r = 0.0866Re$, which agrees well with previous studies for sudden-expansion flow. Unlike the sudden-expansion flow, for a divergent pipe, the recirculation is formed after a critical flow velocity, shown in the inset to figure 2, which depends upon the divergence half-angle α and Re (Peixinho & Besnard 2013).

3. Results and discussion

For sudden-expansion pipe flow, numerical simulations (Cantwell *et al.* 2010; Sanmiguel-Rojas *et al.* 2010) have shown that the flow is unstable to infinitesimal perturbations for $Re \approx 3273$, but the transition in experiments occurs at much lower Re (Sreenivasan & Strykowski 1983; Latornell & Pollard 1986; Mullin *et al.* 2009). The exact nature of the observed instability is therefore unclear. Small disturbances in an experimental set-up are likely to be amplified due to the convective instability mechanism, and appear to be necessary to realise time-dependent solutions. Numerical results (Cantwell *et al.* 2010) have shown that small perturbations are amplified by transient growth in the sudden expansion for $Re \leqslant 1200$, advect downstream and decay. Here, the initial simulations showed that the flow is linearly stable for up to $Re \gtrsim 2200$ for the present computational domain. For larger Re, the recirculation bubble extends close to the end of the outlet section and cannot be calculated reliably. In order to induce early transition, a disturbance is applied to the numerical system in the form (Sanmiguel-Rojas & Mullin 2012)

$$u(\boldsymbol{x}, t) = 2(1 - 4r^2)\boldsymbol{e}_z + \delta \boldsymbol{e}_y, \tag{3.1}$$

adding a finite-amplitude crosswise velocity of magnitude δ.

The perturbation (3.1) distorts the flow, nudging it towards the y direction. A perturbation value of $\delta = 0.001$ is applied in the following simulations. For the sudden-expansion pipe, this is the value of δ for which most results are presented in Sanmiguel-Rojas & Mullin (2012). Results were found to be compatible with the imperfections found in experiments. Figure 3(*a–c*) shows cross-sections of the pipe at $z = 22.5$ and presents contours of the axial velocity. Figure 3(*a*) is at $Re = 1000$ where the flow remains almost axisymmetric. For $Re = 1600$, figure 3(*b*) shows an asymmetry which can just be identified by comparing the solid and dashed lines. To see more clearly the effect of perturbation on the flow, the perturbed flow is subtracted from the (unperturbed) base flow, where it can be observed in the contour plot, figure 3(*c*), that the flow is accelerated on the right-hand side of the pipe section and decelerated on the opposite side. The applied perturbation at the inlet creates a recirculation region with a biased extent (see figure 3*d*). The reattachment pattern is very sensitive to the form of the perturbation given at the inlet, which motivates the application of a simple form of disturbance.

The asymmetry growth of the flow in the cross-section at $z = 22.5$ is measured by calculating the distance of the position of the peak axial velocity component from the centre of the pipe. The square of this distance is denoted ε (Mullin *et al.* 2009). Figure 4(*a*) shows ε as a function of Re with least-squares fitting on the data obtained. It can be seen that at low Re there is no variation in the position of the centroid; a steady symmetric state is observed for $Re < 912$. As Re increases, a symmetry-breaking bifurcation occurs at a critical $Re_c = 912$. This value is smaller than the case of a sudden-expansion pipe ($Re_c = 1139$ in the experiment by Mullin *et al.* 2009). Clearly, the critical Re depends on α and δ. The value of ε increases linearly ($912 < Re < 1500$), forming a steady asymmetric state, with biased growth in

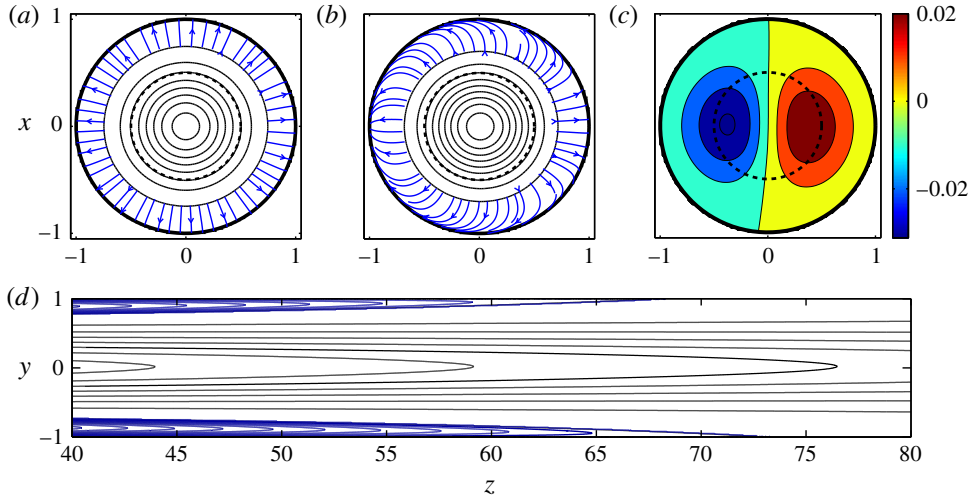

FIGURE 3. Cross-sections of the pipe. Contour line plots of the axial velocity (solid black lines) taken at $z = 22.5$ for (*a*) $Re = 1000$ and (*b*) $Re = 1600$. The dashed line corresponds to the inlet pipe diameter and the blue lines with arrows represent the crosswise velocities within the recirculation region. (*c*) Contour plot of the perturbation, i.e. flow with perturbation ($\delta = 0.001$) subtracted from the base flow ($\delta = 0$) for $Re = 1600$. (*d*) Streamwise cross-section of the flow around the reattachment point at $Re = 1600$ with $\delta = 0.001$.

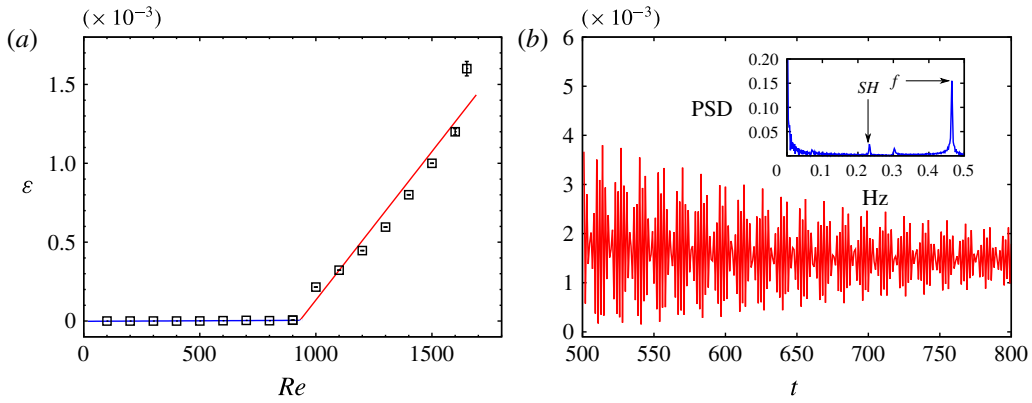

FIGURE 4. (*a*) Asymmetry growth of the flow measured by the square of the distance of the centroid from the centre of the pipe, ε, as a function of Re. The lines are least-squares fits of the data and the intersection of the lines is at $Re_c = 912$ for the estimate of the symmetry-breaking bifurcation point. (*b*) Oscillations of ε at $Re = 1650$ as a function of time. The inset is the fast Fourier transform of the signal with a fundamental frequency $f = 0.468$ and a period doubling sub-harmonic $SH = 0.234$.

the recirculation region. The magnitude of the symmetry deviation grows as the square root of Re, typical of supercritical bifurcation. At larger Re an oscillation state arises ($1500 \leqslant Re \leqslant 1650$), and the flow becomes time-dependent, due to the spatio-temporal oscillation of the reattachment point downstream (Sreenivasan & Strykowski 1983). The error bars in figure 4(*a*) represent the amplitude of the fluctuations in ε. These oscillations are also observed in experiments on sudden-expansion flow (Mullin *et al.*

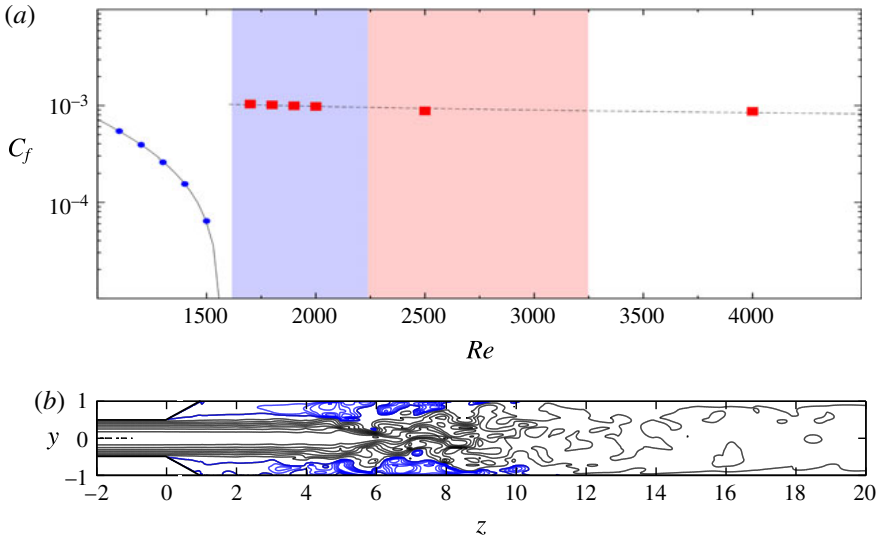

FIGURE 5. (*a*) Plot of the friction coefficient, C_f, with respect to Re. The blue filled circles represent the steady laminar asymmetric flow and the red filled squares represent the unsteady localised turbulent state. The continuous line represents the fit for the laminar state, $C_f = 1.97/Re - 0.0012$, and the dotted line represents a fit for the localised turbulent state, $C_f = 0.0066(Re \times E)^{-0.22}$. The shaded region $1650 \lesssim Re \lesssim 3273$ is the coexistence regime (hysteresis for $\delta = 0$), where the left-hand subregion indicates the extent of the regime explored on the laminar branch in the present system. (*b*) Contour plot of the streamwise velocity of the localised turbulence at $Re = 1680$ with $\delta = 0.001$.

2009). When $Re = 1650$, the flow experiences quasi-periodic oscillations in the shear layer around the recirculation region. This can be seen in the velocity components along the axial as well as in the crosswise direction, and also in the ε evolution (see figure 4*b*). A fast Fourier transform (FFT) was performed on the signal to identify the dominant frequency. The inset in figure 4(*b*) is the FFT of the signal as a function of frequency, where $f = 0.468$ and $SH = 0.234$ is a period doubling sub-harmonic. Here, f seems to correspond to the frequency of vortex shedding around a circular or spherical body which occurs due to the Kelvin–Helmholtz instability (Fabre, Auguste & Magnaudet 2008; Bobinski, Goujon-Durand & Wesfreid 2014). This frequency of oscillation depends upon the type of the perturbation added to the system (Marquet *et al.* 2008; Ehrenstein & Gallaire 2009).

Figure 5(*a*) shows the friction coefficient, C_f, as a function of Re, computed on the wall of the outlet section. At low Re, the flow is steady and asymmetric, and the value of C_f decreases. A significant contributor to the low values of C_f is that the present flow includes the recirculation region, which extends up to approximately half of the outlet section before transition. Around the transition Reynolds number, $Re_t \simeq 1680$, the recirculation region inside the pipe breaks and leads to a localised turbulent state, shown in figure 5(*b*).

An important feature of the turbulence observed here is that it remains spatially localised at a constant position, as observed in sudden-expansion pipe flows (Sreenivasan & Strykowski 1983; Sanmiguel-Rojas & Mullin 2012). The formation of turbulence, near the diverging section, increases C_f due to higher internal mixing and resulting shear at the boundary. In this regime, C_f values scale roughly with the same exponent as the Blasius friction law, even though straight pipe flows are not

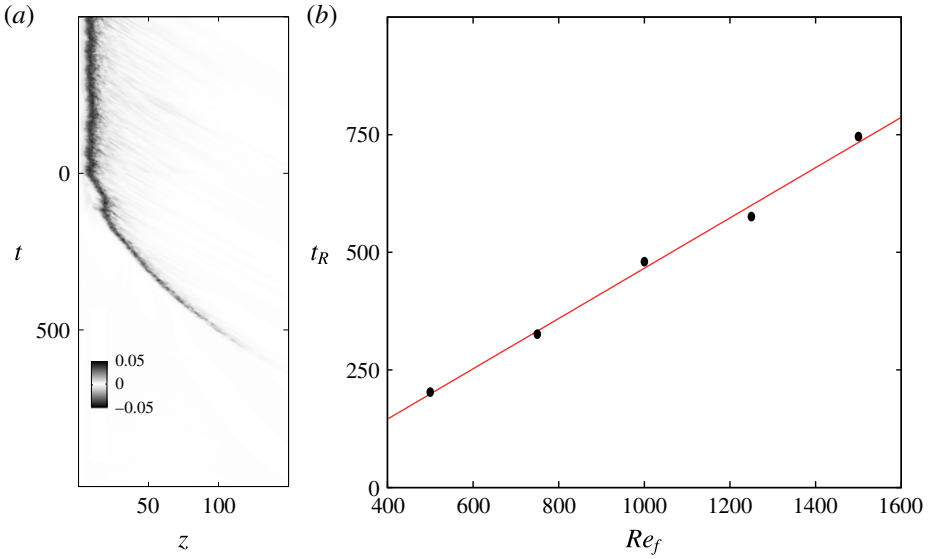

FIGURE 6. Relaminarisation study. (*a*) Spatio-temporal diagram of the streamwise vorticity along the centreline of the pipe, where $z = 0$ corresponds to the start of the diverging section. The localised turbulence decays from $Re_0 = 2000$ to $Re_f = 1500$. (*b*) Relaminarisation time, t_R, versus Re_f.

turbulent at these Re values. The present calculations for the perturbed flow were run up to $t = 600$ and the localised turbulence remained present. The perturbation was then removed and the flow was simulated up to $t = 1200$. The turbulence was observed to be self-sustained, and to occupy the same spatial position. The left-hand shaded region in figure 5(*a*) shows the range of Re in which a laminar state as well as a turbulent state coexist for $1650 \lesssim Re \lesssim 2200$ for the present computational domain. Simulation above $Re > 2200$ without perturbation produces a steady laminar flow with a recirculation region that extends close to or beyond the outlet section. We have therefore limited the range of Re for computation on the laminar branch. For the case of simulations with a perturbation, the amplified energy in the diverging section breaks the recirculation region, creating an early transition, forming localised turbulence, and the computation may be carried out for larger Re along the turbulent branch. Global stability analysis (Sanmiguel-Rojas *et al.* 2010) has revealed that the first bifurcation for the sudden-expansion pipe occurs at $Re \gtrsim 3273$, above which natural transition can be expected without any added perturbation. Given the much larger computational cost, and that we have already computed a range of Re where the laminar and turbulent flows coexist, we have not pursued the linear instability.

Further relaminarisation simulations were performed, where localised turbulence was generated at $Re_0 = 2000$ and the decay to laminar flow was observed for Re below Re_t. In figure 6(*a*), the spatio-temporal diagram shows a typical relaminarisation case. At $t = 0$, Re is reduced suddenly from $Re_0 = 2000$ to $Re_f = 1500$. Here, the localised turbulence detaches from the inlet section almost immediately, then convects downstream and simultaneously decays, which can be seen as the disappearance of the vortical structures (Sibulkin 1962; Sreenivasan 1982). The relaminarisation time, t_R, was obtained by monitoring the time taken for the total energy in the computational domain to fall below a threshold of 10^{-6}. Above $Re_f = 1500$ the turbulence leaves the computational domain before falling below the threshold. Figure 6(*b*) shows

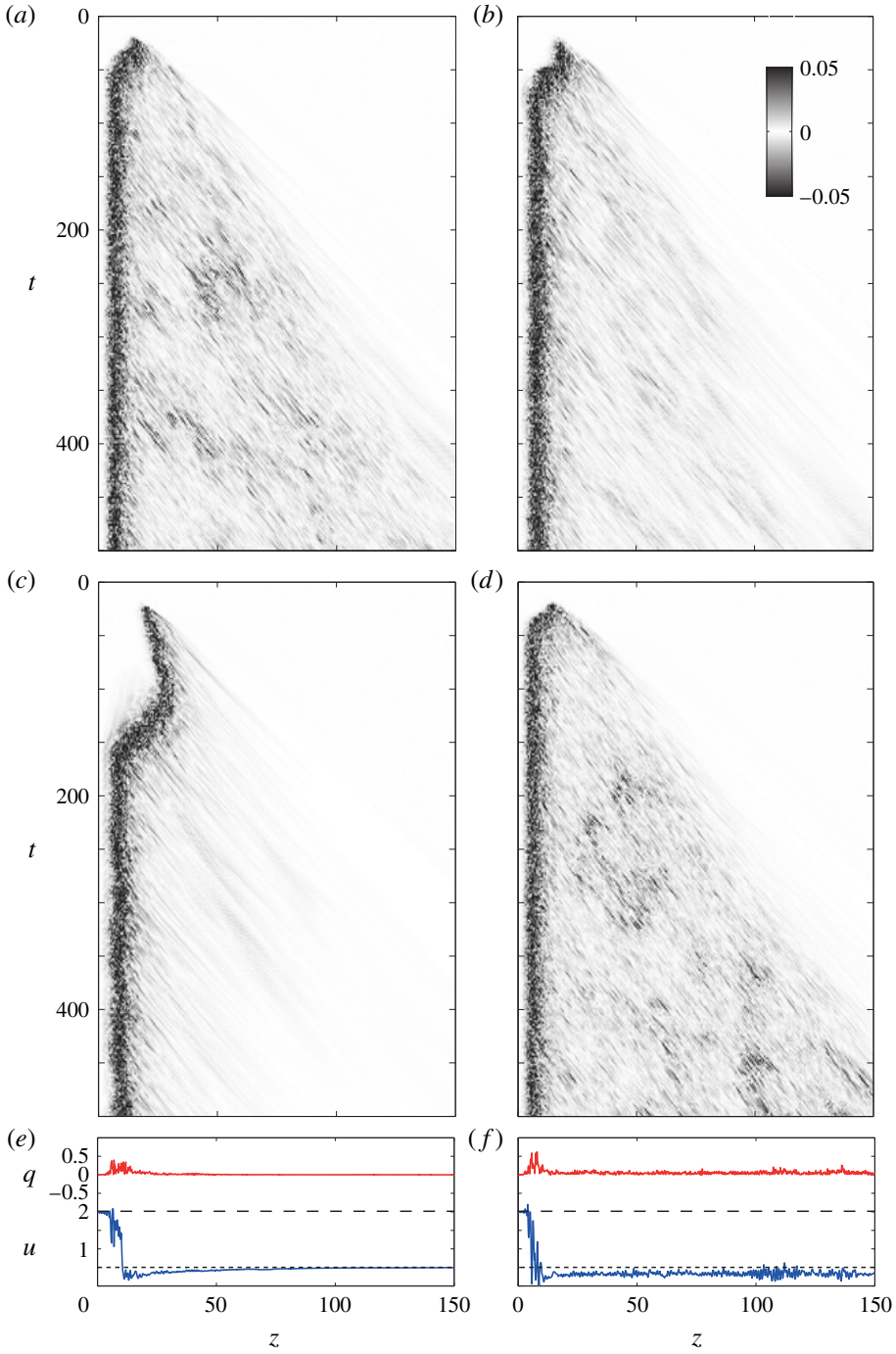

FIGURE 7. The evolution of localised turbulence. Spatio-temporal diagram of the streamwise vorticity along the centreline of the pipe, where $z = 0$ corresponds to the start of the diverging section, for (*a*) $Re = 4000$, (*b*) $Re = 3000$, (*c*) $Re = 2000$ and (*d*) $Re = 5000$. Panels (*e*) and (*f*) show $q = \sqrt{v^2 + w^2}$ in (red) and the streamwise velocity u (blue) at the final time step of (*c*) and (*d*). The dashed lines represent the Poiseuille centreline velocity in the inlet and outlet sections.

t_R as a function of Re_f. The straight line fit indicates that the decay time of the turbulence increases linearly for $Re < 1500$, as identified in experiments (Peixinho & Besnard 2013). Here, no significant period of time was observed before the detachment of turbulence from the walls. Simulations were not carried out within the hysteresis region due to high computational cost. For these Re values the turbulence is self-sustained for some time before detachment from the inlet section, and the time before detachment is expected to diverge rapidly as in uniform pipe flow (Avila *et al.* 2011).

Figure 7 shows the streamwise vorticity spatio-temporal diagram of simulations for (*a*) $Re = 4000$, (*b*) $Re = 3000$, (*c*) $Re = 2000$ and (*d*) $Re = 5000$; the horizontal axis represents the centre axis of the pipe from the diverging section to the outlet. The streamwise vorticity value has been normalised with the maximum vorticity and been plotted with the same scale for comparison purposes. It can be seen that for $Re = 2000$ the turbulence onsets at $t = 25$ and initially moves downstream; at $t = 100$ the turbulence starts moving upstream towards the diverging section and finally holds a stable position $z \simeq 10$. For $Re = 5000$, the onset of turbulence occurs at nearly the same time as that of $Re = 2000$, but the amount of time it takes to reach a localised position is $t = 40$, which is much smaller than that for $Re = 2000$. The time taken to hold a stable position decreases as Re increases. The velocity trace downstream of the localised turbulence for $Re = 2000$ recovers laminar flow (see figure 7*e*). It should be noted that the Reynolds number based on the outlet diameter is half the value of Re. In the case of $Re = 5000$, the flow downstream of the intense region of turbulence exhibits small patches of intense vorticity (see figure 7*d*). The streamwise velocity trace (see figure 7*f*) suggests weak turbulence, which does not return to laminar flow and eventually could lead to puff splitting (Avila *et al.* 2011; Shimizu *et al.* 2014). This property of expansion flow with laminar inlet profile forming localised turbulence and decaying in the outlet section is in good agreement with experiments (Peixinho & Besnard 2013).

The structure within the localised turbulence is further studied using spatial correlations, which have been used to identify fast and slow streaks that dominate the coherent structures within puffs in pipe flow (Willis & Kerswell 2008). The correlation in the streamwise velocity is obtained using the function

$$C(\theta, z) = \left. \frac{2\langle u_z(\theta + \phi, z) u_z(\phi, z)\rangle_\phi}{\langle \max(u_z)^2 \rangle_t} \right|_r , \tag{3.2}$$

where $\langle\cdot\rangle_s$ indicates averaging over the subscripted variable, u_z is the instantaneous axial flow velocity and r is the radial position. The signature of structures of a particular azimuthal wavenumber m is obtained by projecting the correlation function, $C_m(z) = 2\langle C(\theta, z) \cos(m\theta)\rangle_\theta$ (Willis & Kerswell 2008). Figure 8(*a,b*) shows the correlation at $r = 0.5d$, and it can be seen that the $m = 1$ mode dominates the flow, whereas in figure 8(*c,d*) at $r = 0.8d$, the $m = 2$ structure dominates the flow along with $m = 3$ with a much smaller correlation value, which suggests that the flow is more active in the centre region than near the wall. Overall this analysis points out that the localised turbulence in the gradual expansion possesses a different flow structure from the turbulent puff (Wygnanski & Champagne 1973; Willis & Kerswell 2008; Shimizu & Kida 2009), where $m = 3$ and 4 dominate the flow near the wall. The cross-sections in figure 8(*e–h*) indicate slow and fast moving flow.

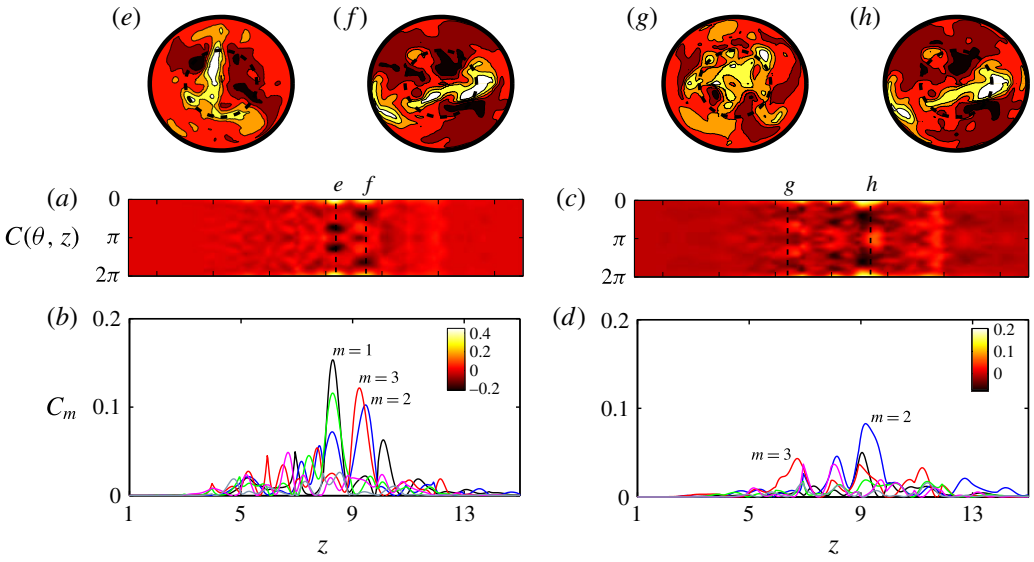

FIGURE 8. Spacial correlation on the streamwise velocity of localised turbulence at $Re = 2000$. Contour of correlation, $C(\theta, z)$, at (*a*) $r = 0.5d$ and (*c*) $r = 0.8d$. Projection function of $C(\theta, z)$ for different azimuthal wavenumbers m at (*b*) $r = 0.5d$ and (*d*) $r = 0.8d$. (*e–h*) Cross-sections of the axial flow relative to the time averaged profile with fast flow (white) and slow flow (red) taken at the corresponding vertical dashed lines.

4. Conclusions

Numerical results for the flow through a circular pipe with a gradual expansion in the presence of an imperfection have been presented. The small imperfection leads to a linear asymmetry growth of the recirculation region, which has also been observed in experiments on sudden-expansion pipe flow. As Re is increased, the long recirculation region oscillates seemingly due to shear Kelvin–Helmholtz instability (Sreenivasan & Strykowski 1983; Mullin *et al.* 2009). This time-dependent motion lies in a narrow range of Re for the amplitude studied here ($\delta = 0.001$). With this level of imperfection, for $Re > 1680$ localised turbulence is triggered in the outlet section of the pipe. As undisturbed laminar flow ($\delta = 0$) is linearly stable up to at least $Re = 2200$, the small disturbance therefore provides a shortcut to subcritical turbulence. Due to the increasing length of the recirculation bubble, the critical Reynolds number for linear instability is beyond our computational limit. We observe that the triggered turbulence is self-sustained if the disturbance is removed. Hence, flow through a perfect gradual axisymmetric expansion ($\delta = 0$) exhibits multiplicity in the solution set of the Navier–Stokes equations, where both the axisymmetric laminar state and turbulent motion coexist over a substantial range of Re, from $Re \approx 1650$ up to the critical Reynolds number for linear instability. By comparison with sudden expansion, we expect the critical Reynolds number to be approximately 3273 (Sanmiguel-Rojas *et al.* 2010). A hysteresis loop therefore exists, where for $\delta = 0$ transition to turbulence occurs at $Re_t \gtrsim 3273$ when Re is increased, and return to laminar flow occurs at $Re \approx 1650$ when Re is decreased. The hysteresis range depends on the value of δ. Our simulations suggest that for $\delta = 0.001$ the hysteresis range is small ($1650 \lesssim Re \lesssim 1680$).

This property of localised turbulent flow with laminar inlet profile forming localised turbulence and decaying in the outlet section agrees with experiments (Sreenivasan

& Strykowski 1983; Peixinho & Besnard 2013). The localised turbulence does not convect downstream but holds a stable spatial position. The structure within the localised turbulence is further studied using spatial correlations, which identify fast and slow streaks that dominate the coherent structures. The main finding is that flow is more active in the centre region than near the wall. Hence, it is important to note that the localised turbulence observed here has a different structure from that of a turbulent puff in uniform pipe flow (Willis & Kerswell 2008).

Acknowledgements

The authors acknowledge the financial support of the region Haute-Normandy and the computational time provided by CRIHAN. Our work has also benefited significantly from many helpful discussions with J.-C. Loiseau, J. E. Wesfreid and I. Mutabazi.

References

AVILA, K., MOXEY, D., DE LOZAR, A., AVILA, M., BARKLEY, D. & HOF, B. 2011 The onset of turbulence in pipe flow. *Science* **333** (6039), 192–196.

BOBINSKI, T., GOUJON-DURAND, S. & WESFREID, J. E. 2014 Instabilities in the wake of a circular disk. *Phys. Rev.* E **89**, 053021.

CANTWELL, C. D., BARKLEY, D. & BLACKBURN, H. M. 2010 Transient growth analysis of flow through a sudden expansion in a circular pipe. *Phys. Fluids* **22** (3), 034101.

EHRENSTEIN, U. & GALLAIRE, F. 2009 Global low-frequency oscillations in a separating boundary-layer flow. *J. Fluid Mech.* **14**, 123–133.

FABRE, D., AUGUSTE, F. & MAGNAUDET, J. 2008 Bifurcations and symmetry breaking in the wake of axisymmetric bodies. *Phys. Fluids* **20** (5), 051702.

FISCHER, P., KRUSE, J., MULLEN, J., TUFO, H., LOTTES, J. & KERKEMEIER, S. 2008, nek5000: Open source spectral element CFD solver http://nek5000.mcs.anl.gov.

HAMMAD, K. J., ÖTÜGEN, M. V. & ARIK, E. B. 1999 A PIV study of the laminar axisymmetric sudden expansion flow. *Exp. Fluids* **26** (3), 266–272.

LATORNELL, D. J. & POLLARD, A. 1986 Some observations on the evolution of shear layer instabilities in laminar flow through axisymmetric sudden expansions. *Phys. Fluids* **29** (9), 2828–2835.

MADAY, Y., PATERA, A. T. & RØNQUIST, E. M. 1990 An operator integration factor splitting method for time-dependent problems: application to incompressible fluid flow. *J. Sci. Comput.* **5** (4), 263–292.

MARQUET, O., SIPP, D., CHOMAZ, J.-M. & JACQUIN, L. 2008 Amplifier and resonator dynamics of a low-Reynolds-number recirculation bubble in a global framework. *J. Fluid Mech.* **605**, 429–443.

MULLIN, T., SEDDON, J. R. T., MANTLE, M. D. & SEDERMAN, A. J. 2009 Bifurcation phenomena in the flow through a sudden expansion in a circular pipe. *Phys. Fluids* **21**, 014110.

PEIXINHO, J. & BESNARD, H. 2013 Transition to turbulence in slowly divergent pipe flow. *Phys. Fluids* **25**, 111702.

SANMIGUEL-ROJAS, E., DEL PINO, C. & GUTIÉRREZ-MONTES, C. 2010 Global mode analysis of a pipe flow through a 1:2 axisymmetric sudden expansion. *Phys. Fluids* **22** (7), 071702.

SANMIGUEL-ROJAS, E. & MULLIN, T. 2012 Finite-amplitude solutions in flow through a sudden expansion in a circular pipe. *J. Fluid Mech.* **691**, 201–213.

SHIMIZU, M. & KIDA, S. 2009 A driving mechanism of a turbulent puff in pipe flow. *Fluid Dyn. Res.* **41** (4), 045501.

SHIMIZU, M., MANNEVILLE, P., DUGUET, Y. & KAWAHARA, G. 2014 Splitting of a turbulent puff in pipe flow. *Fluid Dyn. Res.* **46** (6), 061403.

SIBULKIN, M. 1962 Transition from turbulent to laminar pipe flow. *Phys. Fluids* **5** (3), 280–284.

SREENIVASAN, K. R. 1982 Laminarescent, relaminarizing and retransitional flows. *Acta Mechanica* **44** (1–2), 1–48.

SREENIVASAN, K. R. & STRYKOWSKI, P. J. 1983 An instability associated with a sudden expansion in a pipe flow. *Phys. Fluids* **26** (10), 2766–2768.

WILLIS, A. P. & KERSWELL, R. R. 2008 Coherent structures in localized and global pipe turbulence. *Phys. Rev. Lett.* **100** (124501).

WYGNANSKI, I. J. & CHAMPAGNE, F. H. 1973 On transition in a pipe. Part 1. The origin of puffs and slugs and the flow in a turbulent slug. *J. Fluid Mech.* **59**, 281–335.

Eur. Phys. J. E (2012) **35**: 19
DOI 10.1140/epje/i2012-12019-8

THE EUROPEAN PHYSICAL JOURNAL E

Regular Article

Free surface flow between two horizontal concentric cylinders

J. Peixinho[a], P. Mirbod, and J.F. Morris

Benjamin Levich Institute and Department of Chemical Engineering, City College of City University of New York, New York, NY 10031, USA

Received 20 October 2011 and Received in final form 28 February 2012
Published online: 21 March 2012 –

Abstract. Results are reported on a combined experimental and numerical investigation of a free surface flow at small Reynolds numbers. The flow is driven by the rotation of the inner of two horizontal concentric cylinders, with an inner to outer radius ratio of 0.43. The outer cylinder is stationary. The annular gap is partially filled, from 0.5 to 0.95 full, with a viscous liquid leaving a free surface. When the fraction of the annular volume filled by liquid is 0.5, a thin liquid film covers the rotating inner cylinder and reenters the liquid pool. For relatively low rotation speeds, the evolution of the film thickness is consistent with the theory for a plate being withdrawn from an infinite liquid pool. The overall liquid flow pattern at this condition consists of two counter-rotating cells: one is around the inner cylinder and the other with weaker circulation rate is in the bottom part of the annulus and nearly symmetric about the vertical axis. With increasing rotation rate, the free surface becomes more deformed, and the dynamics of the stagnation line and the cusp line dividing the cells are tracked as quantitative measures of the interface shape. In addition, the recirculating flow cells lose symmetry and the cusp deforms the free surface severely. A comparison of numerically computed flow which describes the interface by a phase-field method confirms the dynamics of the two cells and the interface deformation. For filling fraction 0.75, the liquid level is slightly above the inner cylinder and a significant decrease in size of the bottom cell with increasing rotation rate is found. For filling fractions approaching unity, the liquid flow consists of one single cell and the surface deformation remains small.

1 Introduction

The flow of viscous liquids with free surfaces is fundamental in many situations, ranging from surface coating to geophysical flows. Such flows often exhibit interesting phenomena. One example is liquid flow in a partially filled horizontal cylinder, with flow driven by rotating the cylinder about its axis. For this geometry surprising flow patterns due to secondary flows driven by the dragging of a liquid film have been described [1]; later works showed that different flow patterns may arise [2,3]. A related configuration, in which is found a ribbing or printer's instability, is obtained when the gap between two concentric cylinders is slightly filled with liquid. For small but finite velocities, the flow structure in this geometry may show a complicated set of stagnation lines as well as elliptic and hyperbolic stagnation points between the cylinders. This flow exhibits "nested separatrices" and the structure observed is sensitive to the radius ratio and the speed ratio of the cylinders [4]. The topology of these streamlines and their bifurcations can be understood in the framework of dynamical system theory [5], although experimental comparisons are challenging.

In the present investigation, we consider the flow of a viscous liquid in a partially filled annulus between two horizontal concentric cylinders. Flow is driven by rotation of the inner cylinder. The behavior of the free surface and its relation to the subsurface dynamics are studied. While aspects of this problem have been investigated numerically, there remains a lack of quantitative data, particularly on the free surface morphology, which will be shown to exhibit both large-scale surface deformation and cusp formation.

Analysis of the flow we consider is rather limited. However, the Stokes flow in a half-filled annulus between rotating coaxial cylinders was computed by [6]. This work differs from the present study in considering both cylinders to be rotating, which renders direct comparison impossible given our experimental constraints. The liquid in the calculation noted is confined to the bottom of the annulus, *i.e.* the flow is sufficiently slow that gravity dominates and the interface is flat. Surface tension thus never plays a role. In addition, these authors assumed that i) the thicknesses of the films which develop along the surface of the

[a] *Present address*: Laboratoire Ondes et Milieux Complexes, CNRS UMR 6294 et Université du Havre, 53 rue de Prony, 76600 Le Havre, France.
e-mail: jorge.peixinho@univ-lehavre.fr

cylinders are vanishingly small; and, ii) the free surface remains undeformed everywhere except within the immediate neighborhood of the cylinders. While there can be no direct comparison, it is useful to note that under these conditions, for certain parameter ranges they found the flow to consist of two large cells or eddies: one below but connected to the inner cylinder, and the other in the bottom part of the annulus. Depending on the radius ratio and the speed ratio between the cylinders, the circulations have a potentially rich substructure with separatrices and sub-eddies [4], and it has been noted that the realizability of such flows computed assuming a flat interface depends upon the actual shape of the boundary (*i.e.* the interface).

It is the purpose of the present work to determine this interface shape and the sub-surface flow, both experimentally and numerically, for the arrangement described in [6] but with only the inner cylinder rotating. We outline the main results, as the interface shape and its underlying basis in wetting of the driving boundary lead to a flow quite different than one might deduce for a flat interface and no liquid film over the cylinder. We consider a range of fill fractions with $F \geq 0.5$, as well as for a range of capillary numbers, $0 < Ca \leq 20$, where $Ca = \mu U/\sigma$; μ is the dynamic viscosity of the liquid, U is the surface velocity of the inner rotating cylinder, and σ is the coefficient of surface tension. These conditions include cases in which the free surface is nearly flat at small Ca up to highly deformed at large Ca. While the capillary number is a ratio of interfacial to viscous forces, we note that the large scale flow is determined primarily by a balance of viscous and gravity forces. At small Ca in a half-filled annulus the flow consists of two cells, delineated by a separatrix. One cell orbits the rotating cylinder: it is this feature which clearly differentiates the actual physical flow from the mathematical analysis of [4] and [6].

The structure of the flow implies the need for a stagnation line and a cusp line [7] at the free surface. The cusp line eventually deforms the free surface rather extremely as Ca grows, with the radius of curvature expected [8] to be proportional to $\exp(-\beta Ca)$ once $Ca \gtrsim 1$, where β is a contant. At sufficiently large rotation rate, *i.e.* large Ca, the cusp becomes unstable [9] and air entrainment is observed [10].

Motivation for study of this annular free surface flow arises from phenomena first seen in its application in bioreactors. In this application, a suspension of biological cells is made and fills the annular region, with the flow driven by rotation of the inner cylinder both maintaining cell suspension and enhancing mass transfer of oxygen from the free surface into the bulk. In addition, however, it was observed that the cells formed bands of high and low concentration alternating along the axis of the cylinder, and this has been followed by a number of studies of simpler rigid-particle suspensions [11] and the related flow in a single partially filled cylinder [12–16]. In these studies, the concentration of solids is found to vary axially in alternating bands, with solid fraction even approaching zero in some cases, for $F = 0.5$–0.95 [11, 17]. For the single-cylinder flow, an explanation for the banding process that occurs within a partially filled horizontal rotating cylinder has been proposed [18] based on a lubrication approximation for the flow [19] applied in an analysis for a suspension having a particle-concentration–dependent effective viscosity. The banding instability in the partially filled Couette has been suggested to be mechanistically related to differential drainage rates between particles and fluid [20], and these ideas have been developed into a predictive model [17]. Such analysis has been hampered, because the flow complexity within this geometry does not allow for effective analytical treatments of the global flow. To allow further progress in understanding such flows in application and analysis of multiphase phenomena, we consider the flow with the partially filled Couette in detail.

As this flow is rather complex, it is of interest to develop understanding using numerical tools in combination with experiments. We apply a phase-field model, a diffuse-interface approach, in order to compute the flow over a wide range of conditions and compare against the experiments. We begin in sect. 2 with a description of the experimental setup. The numerical method is presented in sect. 3. A comparison between experimental and numerical results is provided in sect. 4.

2 Experimental setup

Experiments were performed within concentric cylinders shown schematically in fig. 1(a). The outer cylinder is a transparent tube made of acrylic and the interior cylinder is stainless steel. The annulus is closed at each end by acrylic caps into which a sealed bearing is mounted, allowing the inner cylinder to turn while the caps and the outer cylinder are stationary. The device is mounted horizontally, its length is $L = 304 \pm 0.1$ mm and measurements are performed at $L/2$ from the caps (*i.e.*, at the middle). Specifically, high resolution images of liquid levels and film thickness at different rotation speeds were compared and sized using image processing softwares (MATLAB and ImageJ). Several calibrations were performed and all the data are reported with their associated error bars.

Figure 1(b) shows a sketch of the cross-sectional view of the setup where $R_i = 9.5 \pm 0.1$ mm and $R_o = 22 \pm 0.2$ mm. The gap width is $d = R_o - R_i = 12.5$ mm, and the radius ratio is $R_i/R_o = 0.43$, which is normally termed a wide-gap Couette geometry. The cylinder motion is motor-driven (Dayton; model 1L497) and the angular velocity of the inner cylinder can be varied from $\omega \simeq 1$ to 42 rpm, so $U = 2\pi\omega R_i \simeq 1$ to 42 mm/s. Figure 1(b) sketches a cross-sectional view of the liquid film around the inner cylinder. Once the inner cylinder rotates, it drags out a liquid film on one side, and this film then reenters the liquid pool in the annulus on the other side.

The liquid used in the experiments is lubricant UCON 75-H-90,000 (Dow Chemical) of density 1092 kg/m^3 and surface tension 35–40 mN/m at 20°C. This lubricant is stable, noncorrosive, water soluble and its contact angle with acrylic in air is 70–90 degrees. The dynamic viscosity of the liquid was determined from shear ramps of increasing

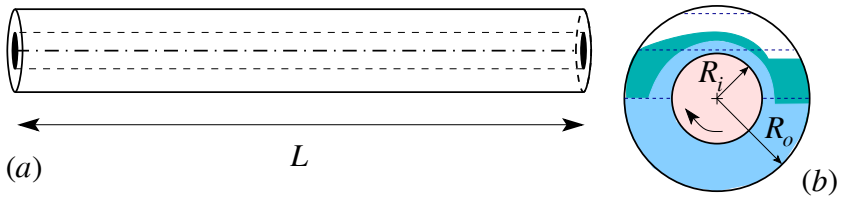

Fig. 1. (Color online) Schematic of the experimental setup. (a) Horizontal concentric cylinders, drawn to scale. (b) Cross-sectional view: a liquid film is coating the inner cylinder. The lighter color represents the liquid in a 50% full annulus, the darker color represents the case of 75% full annulus, both under flow; the dashed horizontal lines represent the levels for 50%, 75% and 90% filling levels (from bottom to top) in the absence of flow.

and decreasing shear rate using a cone-and-plane geometry in a rheometer (TA Instruments). The viscosity is sensitive to temperature, so the room temperature variations are taken into account. The viscosity, μ, in the range 15 to 35°C, can be represented by $\mu(T) = A\exp(-E/RT)$, with $A = 94.35\,\mathrm{Pa\,s}$ and $E = 0.95\,\mathrm{J\,mol^{-1}}$; here T is in Kelvin, and $R = 8.314\,\mathrm{J\,K^{-1}\,mol^{-1}}$ is the gas constant.

We identify five dimensionless parameters describing the flow: a) the Reynolds number which is defined as $Re = UR_i/\nu = 2\pi\omega R_i^2/\nu$; b) the ratio of the inner to outer radius of the annulus; c) the Bond number $Bo = \rho g R_i^2/\sigma$; d) the fill fraction F, *i.e.* ratio between the liquid volume and the annular gap volume between the two cylinders; and e) Ca as defined above. Since $Re = UR_i/\nu = O(10^{-3}$–$0.1)$, inertia may safely be neglected. Indeed, in a similar configuration at filling fraction 0.66 and a thin gap width with radius ratio 0.882, the authors of [21] found that the flow is unstable to inclined traveling rolls from $Re \approx 250$.

With Re essentially zero, a fixed radius ratio (0.43), and constant Bo (28), the independently variable parameters are reduced to two, namely F and Ca. We note that an alternative way of expressing the dimensionless parameters would be to take the ratio between viscous and gravitational forces (which is physically related to the drainage from the cylinder) defined as $\alpha^2 = \omega\nu/gR_i$, where g is the gravitational acceleration. As an alternative, one may use $\alpha^2 = 0.032\,Ca$ for the work described here, and thus $\alpha^2 = O(0.001$–$1)$. We prefer to use the ratio between viscosity and capillary forces captured in Ca, as the free surface here exhibits a cusp. One may view Ca as a convenient nondimensionalization of U on large scales, while retaining the interpretation as a viscous-capillary balance at small feature scales.

3 Numerical formulation

This flow is modeled as axially invariant, and thus we reduce to a two-dimensional calculation on a cross-section. We compute the flow based on the Navier-Stokes equations including a surface tension term

$$\nabla \cdot \mathbf{u} = 0, \tag{1}$$

$$\rho\frac{\partial \mathbf{u}}{\partial t} + \rho\mathbf{u}\cdot\nabla\mathbf{u} = -\nabla p + \mu\nabla\cdot\mathbf{D} + \rho\mathbf{g} + G\nabla\phi, \tag{2}$$

where $\mathbf{u}$ is the velocity, $\mathbf{D}$ is the strain rate tensor: $\mathbf{D} = \nabla\mathbf{u} + (\nabla\mathbf{u})^T$, ρ is the fluid density, t is time, p is the pressure, $\mathbf{g}$ is the gravity, and the last term of eq. (2) represents the surface tension force with G the chemical potential (J/m^3) and ϕ the phase-field variable. We note that $-1 \le \phi \le 1$.

The surface tension is obtained from the Cahn-Hilliard equation, which is given by

$$\frac{\partial\phi}{\partial t} + \mathbf{u}\cdot\nabla\phi = \nabla\cdot\frac{\gamma\lambda}{\epsilon^2}\nabla\psi, \tag{3}$$

where ψ is an auxiliary variable satisfying

$$\psi = -\nabla\cdot\epsilon^2\nabla\phi + \left(\phi^2 - 1\right)\phi + \frac{\epsilon^2}{\lambda}\frac{\partial f}{\partial\phi}, \tag{4}$$

where f is the free energy, γ is a mobility with a fixed value for our work ($\gamma = 10\,\mathrm{m^3\,s/kg}$), λ is the mixing energy density, and ϵ is the interface thickness scale. Note that $\epsilon = 10^{-4}\,\mathrm{m}$ is also constant. It is assumed that the diffuse interface is at equilibrium and thus $\partial f/\partial\phi = 0$. There is a relation [22] between λ, ϵ and the surface tension coefficient such that $\sigma \propto \lambda/\epsilon$, and the chemical potential is defined as $G = \lambda\psi/\epsilon^2$. While boundary element approaches [7, 23–25] are likely to be able to more accurately resolve the detailed structure near the cusp because it reduces the dimensionality of the calculation (here, to the surface contour), this requires an additional step in determining the flow field. For the determination of flow field structure of interest here, the diffuse-interface approach on a spatially variable-mesh density is an efficient and satisfactory method.

We simulate the evolution of $\mathbf{u}$ and ϕ in time using a finite element solver (COMSOL Multiphysics). The geometry described in sect. 2 is implemented in a two-dimensional cylindrical coordinate system. Equations (1)–(4) combined with the no-slip boundary condition at the outer cylinder and oil initially wetting the inner rotating cylinder are solved for small Re. The finite element solver also allows for calculations with a level-set method. However the phase-field method was chosen because it can be constructed by physical arguments and is often used to model viscous flows. In the calculation results presented here, all input parameters equal to the parameters stated in the experimental section, with the upper fluid being air with viscosity $1.73\times10^{-5}\,\mathrm{Pa\,s}$.

The contact angle between the oil and the outer wall can be varied as a boundary condition. This influences the shape of the interface close to the outer wall, the stagnation point position and the cusp position. In the results presented here the contact angle is fixed to 90 degrees. The calculations are unsteady. In any calculation reported, after sufficient time steps a steady solution is observed and the asymptotically steady solution is presented here. The total number of elements of the two-dimensional mesh varies with F and is over 40 000 elements. As noted, the mesh density is also spatially variable within a calculation, and a very fine mesh is used along the interface, particularly near the cusp, as well as along the inner and outer surfaces.

4 Results and discussion

We first describe the experimental measurements and the calculations as a function of Ca for the half-full case, *i.e.* $F = 0.5$. We present results for the film thickness, cusp angle and stagnation line radial position. From these measurements, the shape of the free surface is reconstructed, and its deformation is compared to numerical calculations. For $F = 0.75$, the comparison between experiments and calculations is presented. The results for $F = 0.9$ indicate the presence of a single flow cell.

4.1 Half-full case: F = 0.5

4.1.1 Film thickness

Each experiment began with the apparatus carefully positioned with axis horizontal, and the annulus was filled to the desired fill level with the viscous liquid. The inner cylinder rotation was then started at the desired rate. As noted, this cylinder motion drags a film over the cylinder and into the liquid pool. Hence, the flow consists of two cells, each extending the full range of possible wetted angles around the cylinder. A drawing of a cross-sectional view of the flow pattern is provided in the inset of fig. 2.

Turning to quantitative results, we first consider the film thickness over the inner cylinder, h. As the rotation rate increases, the film thickness increases and the reduction in liquid level downstream, denoted H, also grows as indicated in fig. 2. The error bars represent the spread around an average, taken from two to four measurements. Note that the measured h is roughly proportional to $Ca^{0.46}$ which is consistent with the theoretical scaling of $h \sim Ca^{0.5}$ for the thickness of a liquid film on a vertical flat plate being pulled from an infinite bath for $Ca \gtrsim 1$ [26–28]. Interestingly, the downstream surface level reduction, H, evolves similarly to h for small rotation rates, but appears to saturate within error bar while h continues to grow; specifically, for $Ca \gtrsim 4$, H tends toward a constant value. The saturation before interface breakup may be due to three-dimensional effects or transversal flow [29]. The scatter on the measured H is

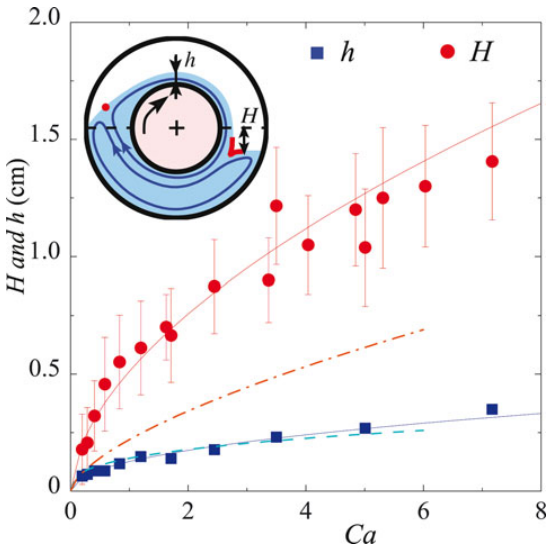

Fig. 2. (Color online) Film thickness, h, and downstream surface level reduction, H, as a function of Ca for the half-full apparatus. The continuous lines represent $H = 0.51\ Ca^{0.56}$ and $h = 0.13\ Ca^{0.46}$ (H and h are expressed in cm). The dashed lines represent the numerical results. The inset sketches the cross-section flow pattern as well as h, H, the stagnation point (red dot) and the cusp.

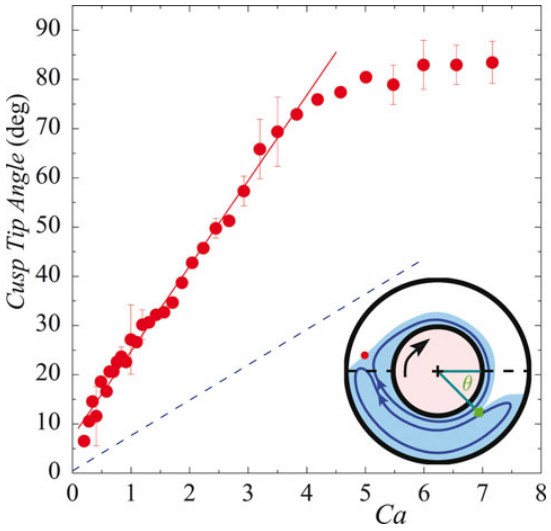

Fig. 3. (Color online) Angle of the cusp tip, θ, as a function of Ca for the half-full apparatus. The continuous line represents a linear fit: $\theta \propto Ca$. The dashed line represents the numerical results. The inset sketches the cross-section flow pattern as well as θ and the stagnation point (red dot).

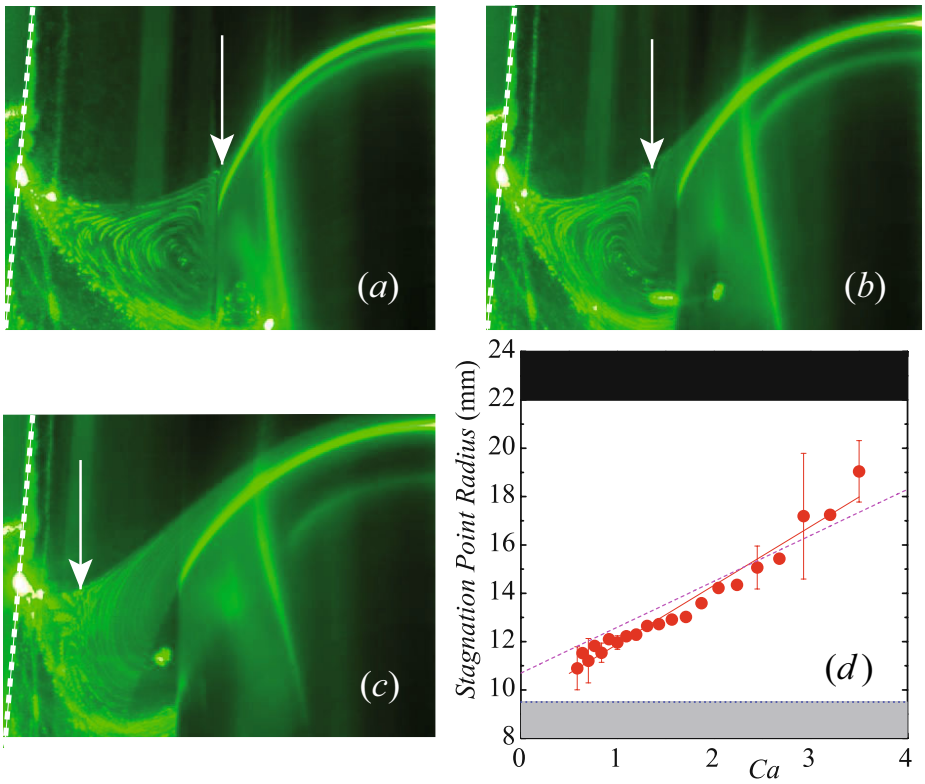

Fig. 4. (Color online) Time lapse photographs of the cross-section in the rising side of the rotating cylinder: (a) $Ca = 0.4$, (b) $Ca = 1.7$, and (c) $Ca = 3.5$ for $F = 0.5$. The white arrow indicates the position of the stagnation line. The dashed white line on the left of each photograph indicates the outer wall position and the right side of each picture is in the vertical plane passing through the rotating axis of the inner cylinder, which is rotating in the clockwise direction. (d) Radial position from the cylinders axis of the stagnation line as a function of Ca. The continuous line represents a linear fit: $2.4\,Ca + 9.6$ (expressed in mm), with the inner cylinder radius: $R_i = 9.6\,\text{mm}$. The dashed line represents a fit of the numerical results.

large because of complications associated with the dynamics of the contact line at the outer cylinder surface. The predictions from the numerical solution are also shown in fig. 2, and are in good agreement with the measurements for h, in fact lying within the experimental error. The predicted H underestimates the measurements.

4.1.2 Cusp angle

On the downstream side of the rotating cylinder, a viscous cusp is formed as in related experiments by [7,8,30]. Whereas these previous studies consider a large pool, here the confinement or the radius ratio affects the cusp tip position. For sufficiently high Ca, the angular position of the cusp tip relative to the original flat interface, θ, was determined, as sketched in the inset in fig. 3. The evolution is roughly linear for $Ca < 4$, but reaches a limiting value of $\theta = 86 \pm 4°$. In the range $Ca \leq 4$, the experimental data can be described with a linear fit, $\theta = 17.4\,Ca + 7.4$. Note that the fit does not predict zero for the origin because the detection of a cusp at low Ca is not straightforward, but we note the slope is somewhat larger for $Ca < 1$. The evolution of the tip radius has been described in related configurations [8,30] and it has been found that the radius of curvature, r, is proportional to $\exp(-\beta Ca)$ when $Ca \gtrsim 1$. As expected the numerical data predict an exponential decrease ($r = 2.78\exp(-0.28Ca)$) of the radius of curvature of the cusp as a function of Ca for $1 \leq Ca \leq 6$.

The calculations results for the tip angle are also reported in fig. 3. Again the model is in qualitative agreement with the experiments, but underestimates θ. The simulation does not recover the saturation region; this could be due to three-dimensional effects not captured in the calculations.

The cusp is asymmetric, as the velocity in the cell adjacent to the inner cylinder is about one order of magnitude larger than that in the outer recirculation cell. The calculations predict the interface breakup and air entrainment at the cusp for $Ca_c \simeq 6$ whereas it is $Ca_c \simeq 8$ in the present experiment. This critical velocity or Ca_c is in agreement with previous measurements [30] where a scaling of Ca_c as a function of the viscosity ratio of the two

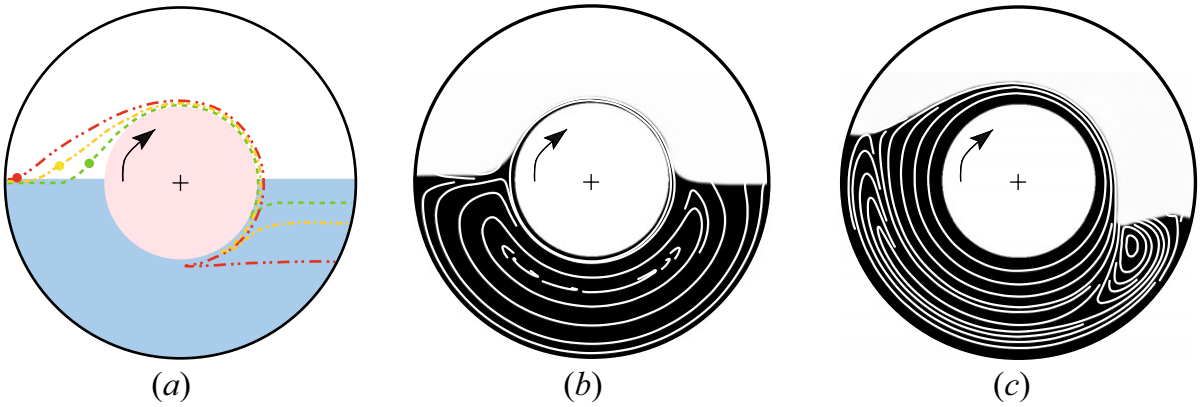

Fig. 5. (Color online) (a) Reconstruction of the free surface at $F = 0.5$ in the absence of flow (light blue filled region), $Ca = 1$ (dashed green line), $Ca = 3$ (dashed-dotted yellow line), and $Ca = 6$ (dashed-dotted-dotted red line). The stagnation line positions are represented by filled dots. (b) and (c) Numerical simulation of the flow for $Ca = 0.9$ and 3.7, respectively. The white lines are velocity streamlines.

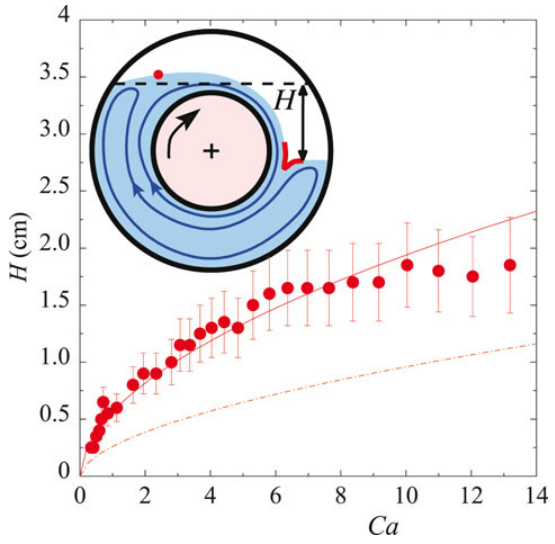

Fig. 6. (Color online) Downstream surface level reduction, H, as a function of Ca for $F = 0.75$. The line represents $H = 0.56\ Ca^{0.54}$ (expressed in cm). The dashed line represents a fit of the numerical results. The inset sketches the cross-section flow pattern as well as H and the stagnation point (red dot).

fluids is observed in agreement with an exponent of $-4/3$ proposed by Eggers [31].

4.1.3 Stagnation line position

Between the two large cells on the rising side of the inner cylinder, there is a stagnation line on the free surface where close streamlines separate. Using time lapse photography and a dilute seeding with 50 μm diameter polyamide particles (from Dantec), the cells can be observed, as depicted in the photographs of fig. 4. A laser sheet is generated perpendicular to the cylinder axis and photographs are taken at an angle of 30° from the horizontal. Quantitative positions of the stagnation line are extracted by comparison with the initial static liquid level. The radial position of the stagnation line increases linearly with Ca as indicated in fig. 4(d). Note that for small Ca, the stagnation line is on the surface rising over the inner cylinder. As Ca increases, the stagnation line moves along the free surface towards the outer wall, while there is a rise and change in curvature of the free surface. As the stagnation line closely approaches the stationary wall, the secondary cell weakens and we are unable to resolve it on the rising side of the rotating cylinder for $Ca > 3.5$. The calculations of the flow reproduce the linear evolution of the stagnation line position within experimental error. We could not experimentally access the limit $Ca \to 0$, but in this limit (obtained by taking $U \to 0$) the stagnation point is expected to asymptotically approach the inner cylinder surface as the film thickness tends to zero; the linear fit of the stagnation point radial position, $2.4\ Ca + 9.6$ (expressed in mm), with the inner cylinder radius $R_i = 9.6$ mm, is in good agreement with this expectation.

The finding that the cusp angle, θ, and the surface level reduction, H, both approach limiting values for $Ca > 4$ suggests there is a roughly fixed flow structure, with the position of the secondary cell underneath the rotating cylinder and the primarily cell varying little as the rate increases. However, h continues to grow with increasing rotation rate.

The numerically computed flow is quantitatively in agreement in terms of the position of the stagnation line and h. The evolution of H and θ as a function of Ca is only qualitatively predicted. A number of runs have been carried out varying the contact angle at the outer wall from 30 to 150 degrees and small changes on the film thicknesses

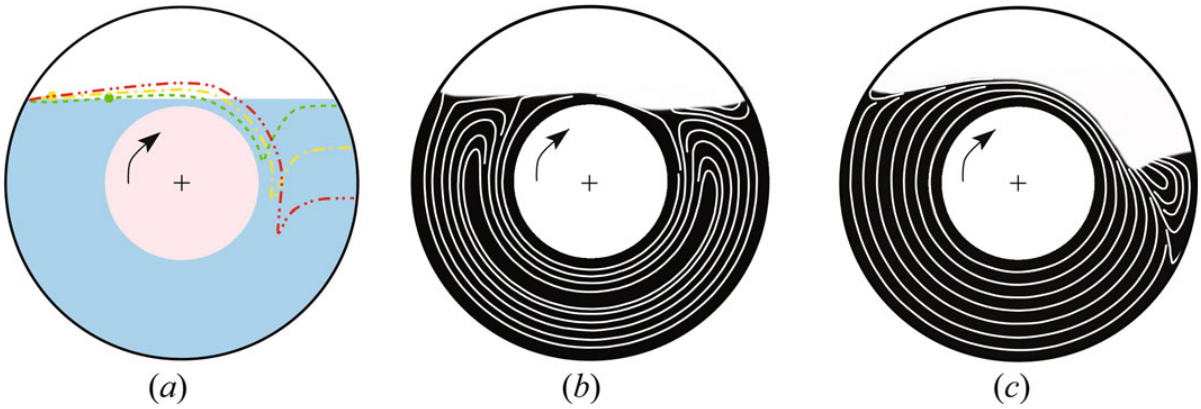

Fig. 7. (Color online) (a) Reconstruction of the $F = 0.75$ free surface for no flow (light blue filled region), $Ca = 1$ (dashed green line), $Ca = 3$ (dashed-dotted yellow line), and $Ca = 6$ (dashed-dotted-dotted red line). The stagnation lines positions are represented by filled dots. Note that there is no dot on the upper left side for $Ca = 6$. Numerical calculations for (b) $Ca = 0.1$ and (c) $Ca = 3.7$ where the secondary cell is confined to the right corner. The white lines are velocity streamlines.

and the positions of the cusp were observed. The main effect of the contact angle is the curvature of the interface close to the outer wall. So our present understanding is that the contact angle is not the only responsible for the discrepancy between experiments and numerical results.

4.1.4 Free surface morphology

From the experimental measurements of film thickness, downstream surface level reduction, cusp angle, and the radial position of the stagnation line, we reconstruct the free surface. We assume that the contact line on the rising side is pinned at the wall because observations indicate it does not change with Ca. Figure 5(a) presents a reconstruction of the free surface for $F = 0.5$. Note that the surface on the downstream side of the inner cylinder is dropped in elevation compared to the initial condition by H, providing the liquid volume associated with the film and the free surface rise around the stagnation line region. The output of the numerical simulation is also displayed in fig. 5(b) and (c), with results at $Ca = 0.9$ and 3.7, respectively. The free surface as well as numerical streamlines for the bottom fluids are also reported. As Ca increases, the two cells become more asymmetric about the vertical centerline. The upper cell in which the flow orbits the inner cylinder grows, as does the film which forms a part of this cell.

4.2 3/4 full case: F = 0.75

4.2.1 Film thickness

When the annulus is 3/4 full, the film thickness, h, has a finite value of approximately 1 mm at $Ca = 0$ (no flow) and increases with Ca. The variation of h is represented by $h \propto Ca^{0.5}$ in the range $2 < Ca < 5$. Meanwhile, the reduction in liquid level downstream surface level, H, again varies roughly as $Ca^{0.5}$ in the range $2 < Ca < 5$ as depicted in fig. 6.

4.2.2 Free surface morphology

For $F = 0.75$, the reconstruction of the free surface from measurements is depicted on fig. 7(a). As explained earlier, the stagnation line moves toward the stationary wall as Ca increases. From the numerical calculations, we find that for small Ca, there are two counter-rotating cells and the stagnation line moves along the free surface toward the outer wall with increasing Ca. The cusp penetration depth is only a few millimeters below the level of the annular pool surface, *i.e.* the surface defining H. Moreover, the cusp does not go unstable to breakup even for large rotation speed corresponding to $Ca = 20$.

Figures 7(b) and (c) present the results of calculations for $Ca = 0.1$ and 3.7, respectively. For small Ca, the flow pattern consists of two cells almost symmetric with respect to the vertical axis. As Ca increases, the bottom cell reduces in size and at large Ca, the outer cell gets confined on the cusp side along the outer cylinder. As Ca increases, the cell reduces in size and eventually disappears.

4.3 Effect of the filling ratio, F

Experiments were conducted for $F = 0.9$. Only a single cell around the inner cylinder is observed for this large fill fraction. There is apparently a continuous transition in the flow structure between $F = 0.75$ (where two cells appear at small Ca) and $F = 0.90$ with its single cell. Note that this behavior is specific to the experimental geometry studied here, with $R_i/R_o = 0.43$.

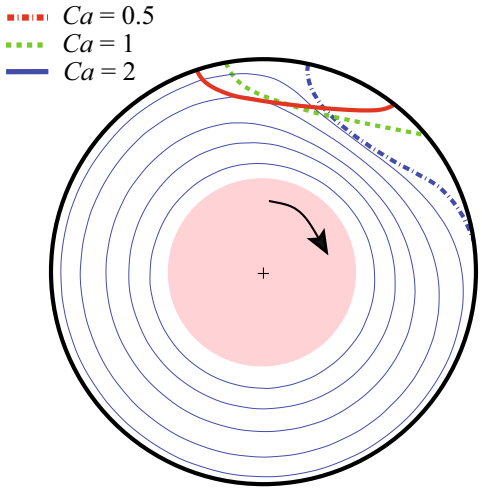

Fig. 8. (Color online) Numerical calculations for $F = 0.90$ and $Ca = 0.5$, 1 and 2. The thick lines represent the interfaces and the thin lines represent velocity streamline in the viscous liquid for the case $Ca = 2$, which evidence only a single cell.

In fig. 8, results of calculations for $F = 0.9$ for $Ca = 0.5$, 1 and 2 are presented. Below $Ca = 0.5$, the interface is almost symmetric with respect to the vertical axis. As Ca increases, the interface deforms and the positions of the contact lines move. Although there is a significant interface deformation, the streamlines of the liquid flow form only a single circulation cell. At high Ca, no cusp can be detected, and the effect of rotation rate leads to minimal changes in the position of the free surface even for large rotation speeds corresponding to $Ca = 20$.

The agreement between our experiments and the calculations leads to the following conclusions. For $F = 0.5$, two cells are always observed up to cylinder rotation rates which cause interface breakup. For $F = 0.75$, there is a transition from two cells to a single cell for Ca between 2 and 3. For $F = 0.9$, only a single cell is observed.

5 Summary

The present work provides information necessary for understanding of the flow in the neighborhood and at the free surface of flow in a partially filled horizontal Couette device, and could serve as the basis for application of the flow or to support analysis of the flow-induced segregation in the particle-laden flow in the same geometry. In addition, the results serve as an interesting test of the accuracy of numerics of free-surface Stokes flow as this flow exhibits features on a range of scales from the cusp to the global structure, as well as a very rich sub-surface flow topology.

Specifically, we have quantified the morphology of the free surface of the flow of a very viscous liquid in a partially filled Couette apparatus at annular filling fractions of $F = 0.5$, 0.75, and 0.9. When the inner cylinder rotates, a thin liquid film is dragged over and plunged into the remaining liquid pool. At the smallest F, two counter-rotating flow cells are observed, one directly adjacent to, and driven by the motion of, the inner cylinder and the other a recirculation lying below. At the free surface, these flow zones are delimited by a stagnation line and a cusp line. When increasing the flow rate, the stagnation line moves from the inner cylinder to the steady wall. On the downstream side of the rotating cylinder, the tip of the cusp line moves below the inner cylinder as the rotation rate increases, with significant deformation of the cells. At the intermediate fill fraction of $F = 0.75$, a significant decrease in size of the bottom cell with increasing rotation rate is found, while $F = 0.9$ exhibits only a single cell for all driving rates.

To properly understand the phenomena in this free-surface Couette geometry and related systems requires consideration of the free surface structure as a function of dynamical variables. The quantitative reconstruction of the free surface, confirmed by our calculations of the flow, indicates that the deformation at elevated driving rates is extreme for the lower fill fractions. A comparison between the measurements and these calculations using a phase-field (diffuse interface) model of the free surface is provided. The position of the stagnation line and the height of the liquid film over the inner cylinder are quantitatively predicted. However, the position of the cusp and the liquid level downstream are only qualitatively recovered by the calculations.

Partial funding for this research (support of P. Mirbod) was provided by the CCNY/UofChicago MRSEC Partnership on the Dynamics of Heterogeneous and Particulate Materials, an NSF PREM (DMR-0934206), and partial funding (software, supplies, and support of J. Morris and P. Mirbod) was provided by the donors of the ACS Petroleum Research Fund (49080-ND9). The authors are grateful to Coralie Carmouze, John Coulet, and Lukas Schimmer for assistance in the initial experiments. We also acknowledge Andreas Acrivos for comments on our earlier version of the paper.

References

1. R.T. Balmer, Nature **227**, 600 (1970).
2. S.T. Thoroddsen, L. Mahadevan, Exp. Fluids **23**, 1 (1997).
3. F. Melo, S. Douady, Phys. Rev. Lett. **71**, 3283 (1993).
4. M.C.T. Wilson, P.H. Gaskell, M.D. Savage, Phys. Fluids **17**, 093601 (2005).
5. M. Brøns, Adv. Appl. Mech. **41**, 1 (2007).
6. P.H. Gaskell, M.D. Savage, M. Wilson, J. Fluid Mech. **337**, 263 (1997).
7. D.D. Joseph, J. Nelson, J. Renardy, Y. Renardy, J. Fluid Mech. **223**, 383 (1991).
8. J.-T. Jeong, H.K. Moffatt, J. Fluid Mech. **241**, 1 (1992).
9. Y.C. Severtson, C.K. Aidun, J. Fluid Mech. **312**, 173 (1996).
10. K.T. Kiger, J.H. Duncan, Annu. Rev. Fluid Mech. **44**, 563 (2012).
11. M. Tirumkudulu, A. Tripathi, A. Acrivos, Phys. Fluids **11**, 507 (1999).

12. M.J. Karweit, S. Corrsin, Phys. Fluids **18**, 111 (1975).
13. O.A.M. Boote, P.J. Thomas, Phys. Fluids **11**, 2020 (1999).
14. M. Tirumkudulu, A. Mileo, A. Acrivos, Phys. Fluids **12**, 1615 (2000).
15. P.J. Thomas, G.D. Riddell, S. Kooner, G.P. King, Phys. Fluids. **13**, 2720 (2001).
16. E. Guyez, P.J. Thomas, Phys. Fluids. **21**, 033301 (2009).
17. B.D. Timberlake, J.F. Morris, Philos. Trans. R. Soc. A **361**, 895 (2003).
18. B. Jin, A. Acrivos, Phys. Fluids **16**, 641 (2004).
19. M. Tirumkudulu, A. Acrivos, Phys. Fluids **13**, 14 (2000).
20. B.D. Timberlake, J.F. Morris, Phys. Fluids **14**, 1580 (2002).
21. I. Mutabazi, J.J. Hegseth, C.D. Andereck, J.E. Wesfreid, Phys. Rev. A **38**, 4752 (1988).
22. P. Yue, J.J. Feng, C. Liu, J. Shen, J. Fluid Mech. **515**, 293 (2004).
23. M.K. Berkenbush, I. Cohen, W.W. Zhang, J. Fluid Mech. **613**, 171 (2008).
24. J. Eggers, S. Courrech du Pont, Phys. Rev. E **79**, 066311 (2009).
25. D. Zhou, J.J. Feng, J. Non-Newtonian Fluid Mech. **165**, 839 (2010).
26. S.D.R. Wilson, J. Engg. Math. **16**, 209 (1982).
27. P.-G. de Gennes, F. Brochard-Wyard, D. Quéré, *Gouttes, bulles, perles et ondes* (Editions Belin, 2002).
28. B. Jin, A. Acrivos, A. Munch, Phys. Fluids **17**, 103603 (2005).
29. G. Bohme, G. Pokriefke, A. Muller, Arch. Appl. Mech. **75**, 619 (2006).
30. E. Lorenceau, F. Restagno, D. Quéré, Phys. Rev. Lett. **90**, 184501 (2003).
31. J. Eggers, Phys. Rev. Lett. **86**, 4290 (2001).

J. Fluid Mech. (2014), *vol.* 748, *pp.* 756–767.
doi:10.1017/jfm.2014.213

Effect of the number of vortices on the torque scaling in Taylor–Couette flow

B. Martínez-Arias, J. Peixinho†, O. Crumeyrolle and I. Mutabazi

Laboratoire Ondes et Milieux Complexes, Université du Havre & CNRS UMR 6294,
53 rue de Prony, 76600 Le Havre, France

(Received 14 November 2013; revised 11 March 2014; accepted 12 April 2014)

Torque measurements in Taylor–Couette flow, with large radius ratio and large aspect ratio, over a range of velocities up to a Reynolds number of 24 000 are presented. Following a specific procedure, nine states with distinct numbers of vortices along the axis were found and the aspect ratios of the vortices were measured. The relationship between the speed and the torque for a given number of vortices is reported. In the turbulent Taylor vortex flow regime, at relatively high Reynolds number, a change in behaviour is observed corresponding to intersections of the torque–speed curves for different states. Before each intersection, the torque for a state with a larger number of vortices is higher. After each intersection, the torque for a state with a larger number of vortices is lower. The exponent, from the scaling laws of the torque, always depends on the aspect ratio of the vortices. When the Reynolds number is rescaled using the mean aspect ratio of the vortices, only a partial collapse of the exponent data is found.

Key words: rotating turbulence, Taylor–Couette flow

1. Introduction

Since the work by Mallock (1888), Couette (1890), Wendt (1933) and Taylor (1936), there has been theoretical and experimental interest in the torque from liquids confined between two concentric differentially rotating cylinders.

Following the work by Taylor (1923), important contributions to the understanding of this flow instability have been made by many authors, including Stuart (1958), Donnelly & Simon (1960), Coles (1965), Snyder (1969), Gollub & Swinney (1975), Barcilon *et al.* (1979), Koschmieder (1979), Mullin & Benjamin (1980), Di Prima & Swinney (1981), Benjamin & Mullin (1982), Nakabayashi, Yamada & Kishimoto (1982), Riecke & Paap (1986), Cliffe, Kobine & Mullin (1992), Lathrop, Fineberg & Swinney (1992), Lewis & Swinney (1999), Takeda (1999), Xiao, Lim & Chew (2002), Czarny *et al.* (2003), Lim & Tan (2004), Abshagen *et al.* (2005), Racina & Kind (2006), Dutcher & Muller (2009), Burin, Schartman & Ji (2010) and many others. Because of these successes, the Taylor–Couette system is used to investigate the turbulence scaling laws, in particular the behaviour of the dimensionless torque acting on the rotating cylinder as a function of the Reynolds number.

† Email address for correspondence: jorge.peixinho@univ-lehavre.fr

From a practical point of view, Wendt (1933) and Donnelly & Simon (1960) provided scaling laws for the dimensionless torque, G, as a function of the Reynolds number, Re, i.e. $G \propto Re^{\alpha}$, with an exponent, α, that depends on Re and other parameters. More recent studies (Lathrop *et al.* 1992; Lewis & Swinney 1999; Dubrulle *et al.* 2005; Ravelet, Delfos & Westerweel 2010; van Gils *et al.* 2011; Paoletti & Lathrop 2011) provided additional data on torque and were concerned with fairly large Reynolds numbers.

Eckhardt, Grossmann & Lohse (2007) proposed analogies between turbulence in Rayleigh–Bénard convection and in Taylor–Couette flow with emphasis on the evolution of the exponent. An argument was put forward to investigate turbulent Taylor–Couette flow because it has a stronger driving than Rayleigh–Bénard flow and should allow access to the ultimate turbulent regime (Huisman *et al.* 2012; Ostilla-Mónico *et al.* 2014). This unifying theory was tested using the data of Lathrop *et al.* (1992) and Lewis & Swinney (1999). They found good agreement for a range of Reynolds numbers above 10^4.

From a numerical point of view, several groups (Coughlin & Marcus 1996; Batten, Bressloff & Turnock 2002; Bilson & Bremhorst 2007; Pirró & Quadrio 2008; Brauckmann & Eckhardt 2013; Ostilla *et al.* 2013; Ostilla-Mónico *et al.* 2014) were able to simulate turbulent Taylor–Couette flow up to relatively high Re. Most of these investigations (Brauckmann & Eckhardt 2013; Ostilla *et al.* 2013; Ostilla-Mónico *et al.* 2014) used periodic boundary conditions with relatively short calculation domains. Ostilla *et al.* (2013) presented the effect of three- and four-vortex pairs on the dimensionless momentum transport, suggesting that the larger number of vortex pairs induces an increase in torque. Brauckmann & Eckhardt (2013) investigated the effect of the vortex size on the torque and found a maximum of torque for vortices of axial wavelength of 1.93 times the gap width for $Re = 5000$. Hence, the Taylor–Couette system offers an opportunity to vary the number of vortices for a fixed value of the aspect ratio and therefore to modify the vortex shape and the shear between two adjacent vortices. However, none of the recent studies have explicitly mentioned the number of cells, although both Lathrop *et al.* (1992) and Lewis & Swinney (1999) provided torque data for eight- and 10-vortex states.

In this article, we elucidate the effect of the number of vortices on the torque–speed relationship in a system containing up to nine states. This article is organised as follows. A description of the experimental apparatus is given in § 2 together with a detailed discussion of the protocols to obtain the different numbers of vortices. This is followed, in § 3, by the results for the torque data which are analysed. Finally, we draw some conclusions in § 4.

2. Experimental set-up and procedure

2.1. *Experimental set-up*

The Taylor–Couette geometry used here is fitted on a rheometer (Physica MCR 501, Anton Paar). Figure 1 shows a sketch of the experiment. The inner cylinder has a radius of $r_i = 50 \pm 0.01$ mm and the outer cylinder has a radius of $r_o = 55 \pm 0.01$ mm. Hence, the gap between the two cylinders is $d = r_o - r_i = 5 \pm 0.01$ mm. The length of the inner cylinder is $L = 150 \pm 0.5$ mm. Consequently, the dimensionless parameters that describe the geometry are the radius ratio $\eta = r_i/r_o = 0.909$ and the aspect ratio $\Gamma = L/d = 30$. The object of the present experiments was to examine the relationship between the angular speed of the inner cylinder, Ω, and the torque that it exerts on the fluid, T. The Reynolds number, Re, is based on the angular velocity of the

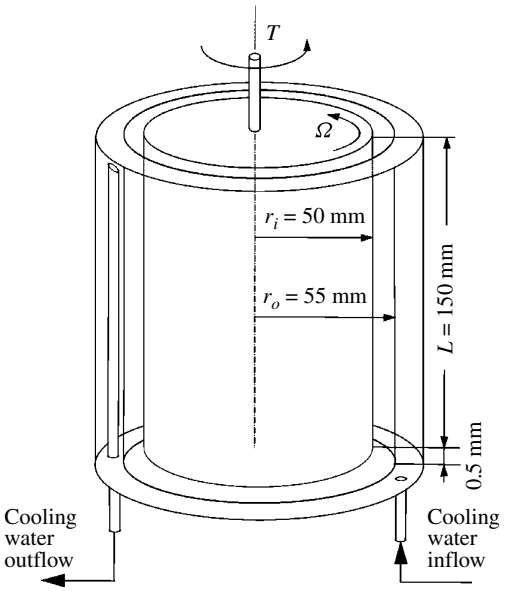

FIGURE 1. Sketch of the Taylor–Couette system, drawn to scale.

inner cylinder, the radius of the inner cylinder, the gap between the cylinders and the properties of the fluid, $Re = \Omega r_i d/\nu$, where ν is the kinematic viscosity of the working fluid. The dimensionless torque, G, is based on the torque exerted by the fluid in the walls of the inner cylinder, the height of the inner cylinder and the properties of the fluid. Here, G is defined as $G = T/2\pi\rho\nu^2 L$, where ρ is the density of the working fluid. In addition to G, the so-called ω-Nusselt number, Nu_ω, defined according to Eckhardt *et al.* (2007), is also used,

$$Nu_\omega = \frac{G}{G_{lam}}, \quad \text{where } G_{lam} = \frac{2\eta}{(1+\eta)\,(1-\eta)^2} Re. \tag{2.1}$$

Here, Nu_ω represents the torque measured in units of laminar torque.

The inner cylinder is made of aluminium and its surface is anodised. The bottom of the inner cylinder is recessed. There is a gap of 0.5 ± 0.001 mm between the edge of the base of the inner cylinder and the flat bottom of the outer cylinder filled with an air bubble, which minimises the shear stress on the bottom of the cylinder. The top part of the gap between the two cylinders is covered with an annular PVC lid. It is positioned so that the bottom of the lid is at the same height as the upper edge of the inner cylinder. This means that the gap is completely filled and there is no contact between the lid and the inner cylinder. The outer cylinder is made of glass and there is an additional glass jacket connected to a flow of water in order to maintain the working temperature at $22 \pm 0.01\,^\circ$C. For flow visualisation purposes, 2 % of Kalliroscope is added to the fluid. The rheometer allows for torque- or speed-controlled runs. The highest acquisition frequency is 100 Hz and the real resolution of the encoder is smaller than 1 μrad. The accuracy of the torque is 0.5 % of the measured value and is never smaller than 0.2 μN m. Several fluids, mixtures of water and glycerol, were used in order to optimise the speed acquisition. Additional measurements were made using a low-viscosity silicone oil in order to obtain data in the highest range of Re.

2.2. *Experimental procedure*

In quasi-static ramping of the velocity, the Taylor vortex flow is characterised by 30 time-independent axisymmetric toroidal vortices from $Re_c = 138$. This value is close to the predicted value (139) given by the stability theory (Esser & Grossmann 1996). For $157 < Re < 199$, wavy vortex flow is seen. Then, from $Re = 199$, modulated wavy vortex flow is observed.

In figure 2, a spatio-temporal diagram over the whole height of the cylinders is presented. The flow is driven by the rotation of the inner cylinder at a constant ramping rate, $\partial Re/\partial\tau = 4$, where $\tau = t\nu/d^2$ and t is time. As Re increases from laminar Couette flow, Eckman vortices develop at the ends of the cylinders (Czarny *et al.* 2003). Then, these vortices evolve into a well-defined state of axisymmetric steady toroidal Taylor vortices that rapidly join at the centre of the cylinder at $Re = 143$. At $Re = 174$, wavy vortex flow starts. In figure 2, the second interval ($250 < Re < 450$) shows sequences of regions of strong modulation leading to the merging of cells (26, 24 and 22). In this same range of Re, Coles (1965) showed in a system of similar aspect ratio that a large number of expected states were accessible due to the vertical oscillations and the merging of these cells. Clearly, as we progress in time or in Re the number of cells decreases from 30 to 20. To obtain a smaller number of cells, say 18, a lower acceleration is used. Hence, this merging of cells will allow us to prepare an initial state with 30 to 18 cells. Only the number of cells is taken into account and spiral modes are not considered here. Once the desired number of cells is set up, our strategy is to instantaneously change the torque to a prescribed value and then measure the velocity for a few minutes before the next measurement. The stability of each state was tested for approximately 70 times the viscous time, i.e. ν/d^2, to ensure that the number of vortices remained constant. The velocity fluctuations of the rotating cylinder are small, typically around 0.6 %.

3. Results and discussion

The results are a combination of torque measurements and simultaneous flow visualisations. The first set of results is concerned with the properties of two distinct states, 30- and 18-cell states. The second set of results presents and analyses the torque data, and describes the stability limit of the states as well as the change in behaviour in the torque–speed curves for different states.

3.1. *Aspect ratio of cells*

The finding of different states for the same boundary conditions requires that the size of the cells varies from one state to another. In figure 3(*a*,*b*), photographs of two states with 30 and 18 cells at $Re = 6000$ are presented. Figure 3(*c*) presents their aspect ratio along the vertical axis. For intermediate numbers of cells, 20, 22, 24, 26 and 28, intermediate curves are expected. For the primary state of 30 cells, the aspect ratio, l/d, of all the cells is close to one. However, for the 18-cell pattern, the ratio l/d is 1.5 in the centre of the cylinder, so the cells are elongated. It should be noted that the cells close to the ends of the cylinders have a significantly larger aspect ratio up to 2.5. This indicates that the caps have a local effect and strongly elongate the two cells close to the ends (Czarny *et al.* 2003). Although the data on the aspect ratio are for $Re = 6000$, using the same protocol we have observed states with different numbers of vortices over a wide range of Re that look essentially similar to the ones in figure 3(*a*,*b*).

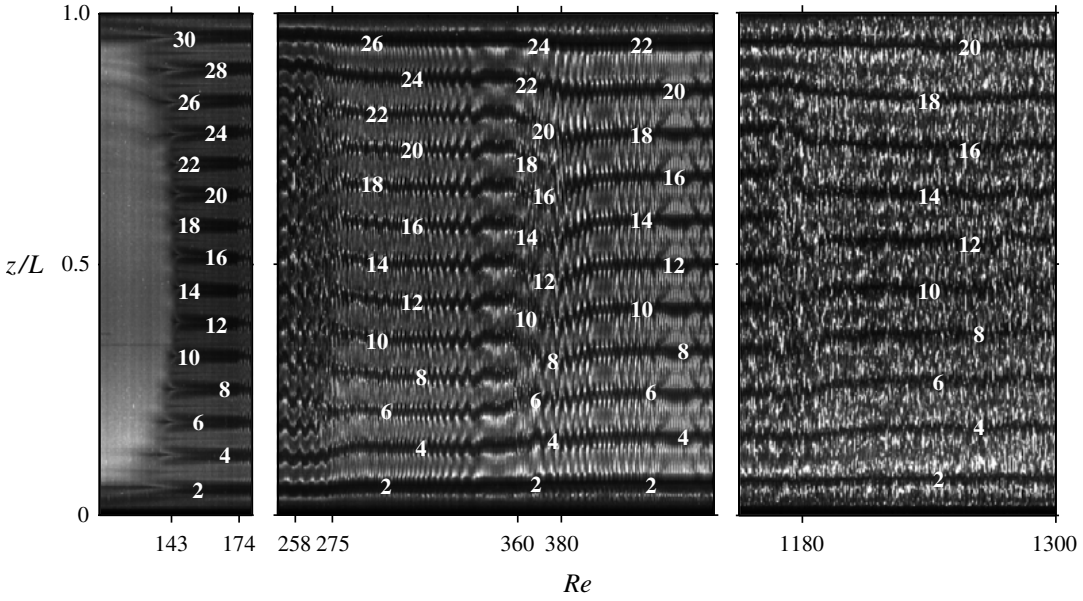

FIGURE 2. Spatio-temporal diagram over the whole height ($\Gamma = L/d = 30$) of the Taylor–Couette flow ($\eta = 0.909$) in three intervals from $Re = 110$ to 1300. The acceleration rate is $\partial Re/\partial\tau = 4$. The numbers on the diagram count the number of cells from bottom to top.

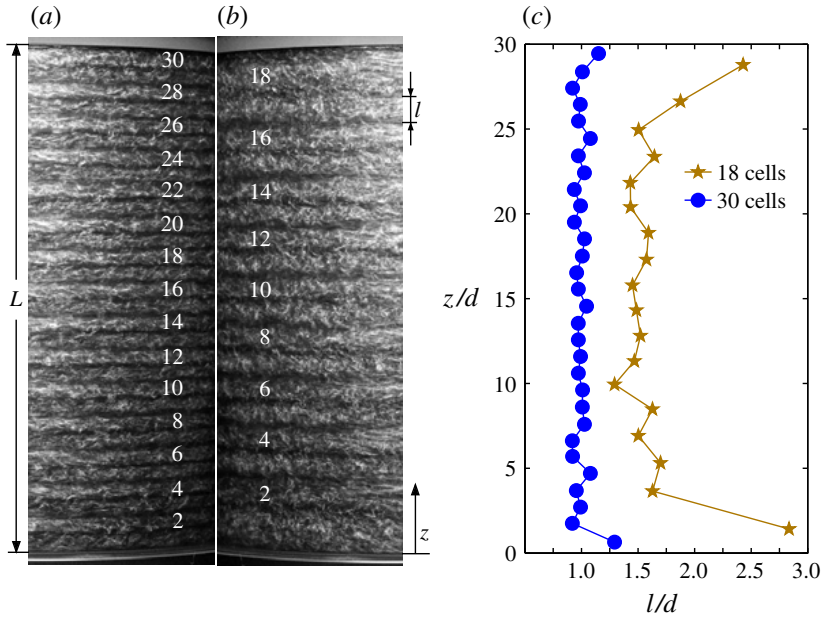

FIGURE 3. (Colour online) Photographs and aspect ratios along the axis of 30 and 18 cellular modes at $Re = 6000$. (*a*) Normal 30 cells, (*b*) abnormal 18 cells and (*c*) the associated aspect ratio along the axis.

The states in figure 3 were obtained at $Re = 6000$. The difference in the measured torque between the 18-cell state and the 30-cell state is 13.5 %. The state with the larger number of cells experiences a larger torque. This is in agreement with the

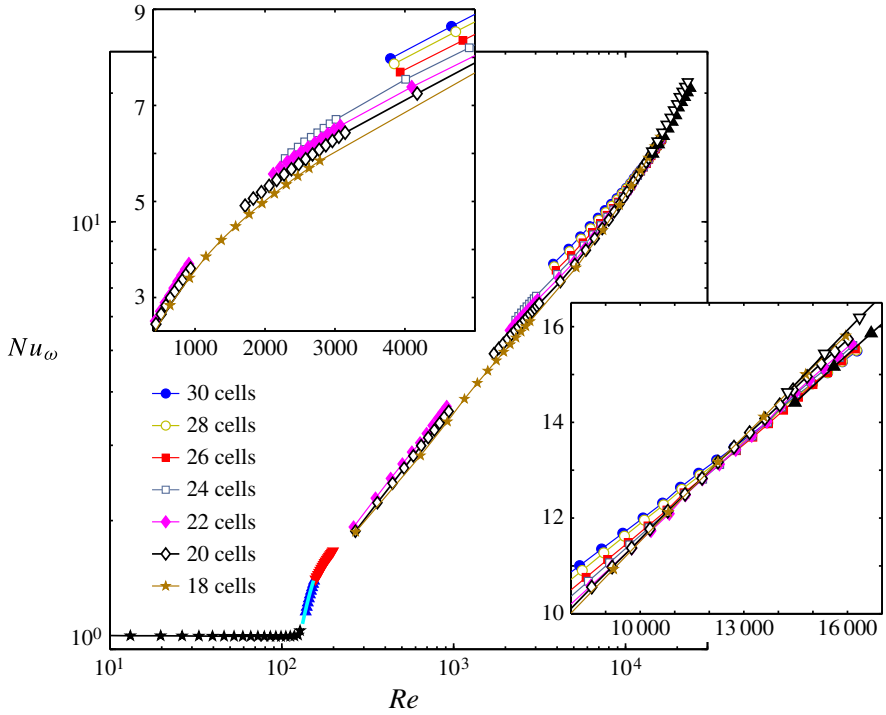

FIGURE 4. (Colour online) Rescaled torque, Nu_ω, as a function of Re for the different flow states. The black stars (★), blue triangles (▲) and red triangles (▼) represent the Couette flow, the Taylor vortex flow and the wavy vortex flow, respectively. The thick (cyan) line represents a fitting using the proposed scaling of Donnelly & Simon (1960). The top inset is a zoom at small Re in linear scale showing the stability limits of some states. The bottom inset is a zoom at large Re in linear scale showing the intersections. The black triangles (▲) and the empty triangles (▽) represent data obtained using low-viscosity silicone oil. The error bars are smaller than the plotting symbols.

numerical simulation of Ostilla *et al.* (2013), although their range of Re ($400 < Re < 1600$) and the number of cells tested (six or eight cells) is smaller.

3.2. *Torque*

Torque and speed measurements have been performed up to an Re of 24 000. Using the procedure presented earlier we were able to measure the torque associated with seven different states: 30, 28, 26, 24, 22, 20 and 18 cells. The relationship between the ω-Nusselt number and the Reynolds number for these states is presented in figure 4. Different symbols and colours represent the different states: the laminar Couette flow, the Taylor vortex flow (30 cells), the wavy vortex flow and the seven different turbulent Taylor vortex flows with 30, 28, 26, 24, 22, 20 and 18 cells. In order to access large values of Re up to 24 000, low-viscosity silicone oil was used and two series of data are reported in figure 4. The use of silicone oil does not allow one to visualise the flow and therefore to count the number of vortices. These data were obtained by applying protocols leading to states with large and small numbers of cells. The trend of the curves suggests that the black triangles correspond to large numbers of cells and empty triangles to small numbers of cells.

In figure 4, the ω-Nusselt number associated with Couette flow ($Re < Re_c$) is almost constant and just above one; the small difference from one is due to end effects. The Taylor vortex flow and the wavy vortex flow have distinct properties, corresponding to different slopes in the Nu_ω versus Re curve. The rescaled torque behaviour for Taylor vortex flow ($138 < Re < 154$) is fitted by a relation suggested from the finite amplitude theory by Stuart (1958) and proposed by Donnelly & Simon (1960),

$$Nu_\omega = aRe^{-2} + bRe^{0.36}, \tag{3.1}$$

with $a = -13\,374$ and $b = 0.33$.

The stability domains of the different numbers of vortices are shown in the top inset of figure 4. It is interesting to notice that the 30-, 28- and 26-vortex states are not stable for Re below 3800. Similarly, the 24-, 22- and 20-cell states are not stable for Re below 2300, 2100 and 1700, respectively. In the range between 1000 and 1700, only the 18-cell state is stable. These results are reminiscent of the stability studies of Coles (1965), Snyder (1969), Koschmieder (1979) and Cliffe *et al.* (1992).

As the Reynolds number increases, a systematic increase of the ω-Nusselt number is observed. The 18-cell state always has the lowest ω-Nusselt number, whereas the states associated with the largest number of cells always have the highest ω-Nusselt number. As the Reynolds number increases further, the curves of Nu_ω versus Re move closer together. Then, the curves for different states intersect in a range of Re between 9600 and 15 500. A zoom in this range is shown in the bottom inset of figure 4, where most of the intersections are located at approximately 12 600. Below each intersection, the torque is larger for states where the number of cells is larger. Above each intersection, the trend changes and a smaller number of cells leads to a larger torque. Similar intersections were reported by Lathrop *et al.* (1992) and Lewis & Swinney (1999) for eight- and 10-cell states in a system with a radius ratio of 0.724.

The analysis of our data allows us to present, in figure 5, the rescaled torque as a function of the aspect ratio of the vortices, $\bar{l}/d$, for several values of Re. For relatively small Re, the rescaled torque decreases as the aspect ratio of the vortices increases. For large Re, the rescaled torque increases with $\bar{l}/d$. At $Re = 13\,000$, Nu_ω is almost constant. In the experiments, values of $\bar{l}/d$ between 0.88 and 1.5 correspond to states with 34–18 cells. Our results confirm a clear effect of the vortex aspect ratio on Nu_ω, which was predicted by numerical simulations (Brauckmann & Eckhardt 2013; Ostilla *et al.* 2013). For $Re = 5000$, our values of Nu_ω are slightly lower than the numerical results of Brauckmann & Eckhardt (2013) and do not exhibit the peak that these authors found in their data at $\bar{l}/d = 0.965$. The discrepancy between the experiments and the numerical simulations may be due to the fact that the numerical simulations were performed for a radius ratio of 0.71.

3.3. *Exponent*

The dependence of Nu_ω on Re can be described by

$$Nu_\omega = \mathcal{A}\, Re^{\alpha-1}, \tag{3.2}$$

where $\mathcal{A}$ depends on the vortex aspect ratio and is a decreasing function of Re. A motivation behind seeking scaling laws is that insight into the turbulence mechanisms can be uncovered (see Dubrulle *et al.* 2005; Eckhardt *et al.* 2007). It is clear that the scaling laws discussed above cannot hold for Taylor vortex flow and wavy vortex flow since the flow is non-turbulent. Donnelly & Simon (1960) discussed this issue

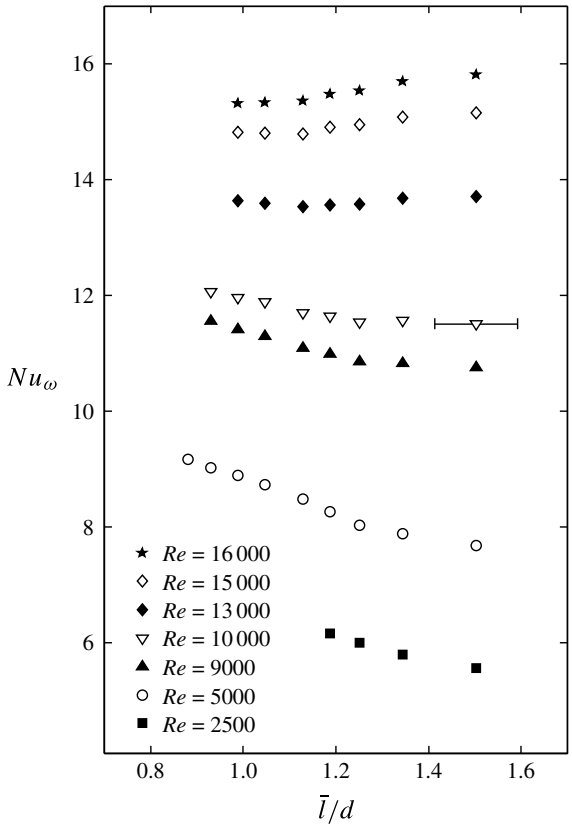

FIGURE 5. The rescaled torque in dependence on the aspect ratio of the cells for different values of Re. The horizontal error bar for $Re = 10\,000$ represents the maximum error on $\bar{l}$. The vertical error on Nu_ω is smaller than the symbol height.

and proposed the scaling (3.1) for Taylor vortex flow. For the range of Re below 3000, the exponent found in the present study is almost constant ($\alpha \simeq 1.5$) and agrees well with the data from Lim & Tan (2004) and Ravelet *et al.* (2010).

Figure 6(*a*) displays the variation of $\alpha - 1$ as a function of Re for different numbers of cells for $4000 \lesssim Re \lesssim 21\,000$. Here, $\alpha - 1 = \partial(\log_{10} Nu_\omega)/\partial(\log_{10} Re)$ is calculated for each state separately as a function of the Re using a sliding least-square fit (Lathrop *et al.* 1992; Lewis & Swinney 1999; Ravelet *et al.* 2010; Merbold, Brauckmann & Egbers 2013) over the interval $\Delta(\log_{10} Re) = \Delta_{10} = 0.1$. For the 18-cell state the interval is 0.2. The results are compared with those of Ravelet *et al.* (2010) whose experiment has $\eta = 0.917$ and $\Gamma = 22$. Although their aspect ratio is smaller then ours, there is good agreement between their results and the present exponents for the 20- and 22-cell states. Both studies exhibit monotonic increase for $3000 \lesssim Re \lesssim 15\,000$.

A new scaling of the Reynolds number based on the mean aspect ratio of the cells, $\bar{l}Re/d$, is proposed for the exponent in figure 6(*b*). Only a partial collapse of the data is found. This suggests that the size of the cells is an important parameter in the turbulent regime studied here. It should be noted that at higher $\bar{l}Re/d$, the collapse is better.

The meaning of α is related to the viscosity dependence of the torque (Lathrop *et al.* 1992). The Kolmogorov assumption assumes $\alpha = 2$ for fully developed turbulence

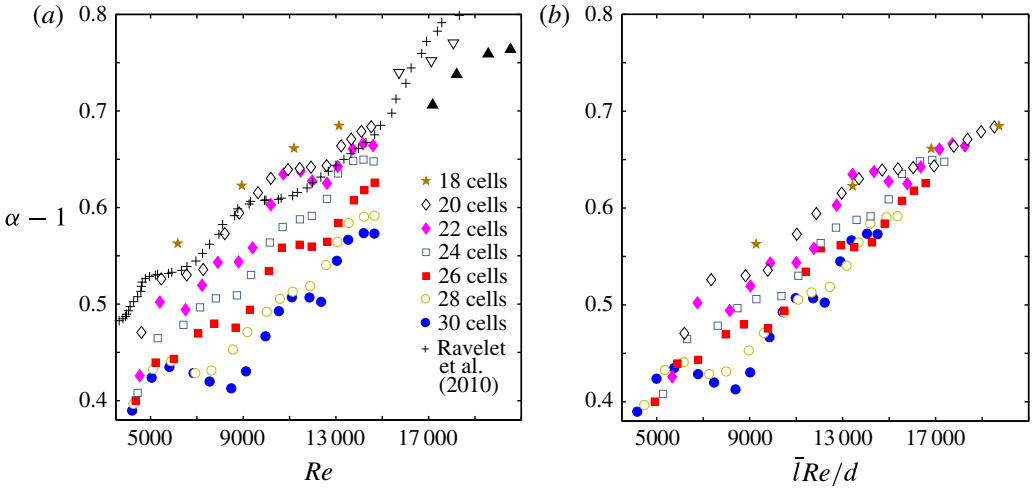

FIGURE 6. (Colour online) Evolution of the exponent for different numbers of cells. The black triangles (▲) and the empty triangles (▽) represent data obtained using low-viscosity silicone oil. (*a*) $\alpha - 1$ as a function of Re and (*b*) $\alpha - 1$ versus $\bar{l}Re/d$, based on the averaged height of the cells, $\bar{l}$.

(Doering & Constantin 1992). Any deviation from $\alpha = 2$ implies a particular form of velocity fluctuations. In a flow system with a given number of vortices, the form of the velocity fluctuations is constrained by the presence of large-scale vortices and cannot be completely random. Modern investigations using particle image velocimetry (see Racina & Kind 2006; Tokgoz *et al.* 2012) aim to quantify the velocity fluctuations and estimate the average turbulent kinetic energy dissipation rate.

The principal feature that we wish to highlight is the systematic dependence of the scaling on the aspect ratio of the cells, displayed in figure 6. For situations where the number of cells is small, typically 18 here, the flow is less constrained by the cells. Therefore, the turbulent flow will exhibit larger velocity fluctuations, leading to higher turbulence and a larger α. For situations were the number of cells is large, typically 30, the flow is more constrained by the cells and the velocity fluctuations are weaker, leading to a smaller α.

4. Conclusions

The effect of the number of vortices on the torque in a Taylor–Couette flow ($\eta = 0.909$ and $\Gamma = 30$) up to $Re = 24\,000$ has been quantified. A specific protocol was used to obtain different states with 34, 32, 30, 28, 26, 24, 22, 20 and 18 cells. The evolution of the rescaled torque, Nu_ω, versus Re for different numbers of cells was obtained. The results are in agreement with those of Lim & Tan (2004) and Ravelet *et al.* (2010) and, moreover, the curves superpose self-consistently.

The effect of the vortex size on the rescaled torque indicates a change in behaviour corresponding to an intersection in the Nu_ω versus Re curves at Re between 9600 and 15 500. For most of the states, the intersection is at approximately 12 600. Before each intersection, the torque is larger for a large number of cells and smaller after the intersection. In the same range of Re, but for a system with a radius ratio of 0.725, Lathrop *et al.* (1992) found a transition from centrifugal instability to shear turbulence using torque and local wall shear stress data. Lewis & Swinney (1999) confirmed

this transition by means of additional data on torque and wall shear stress, as well as velocity measurements. The data from Lewis & Swinney (1999) show a similar intersection for eight- and 10-cell states. In our case, it is not possible to conclude that the intersection is an indicator of a transition to shear-driven turbulence.

The scaling exponent of the torque is larger for states with large aspect ratios. It is also found that the exponents collapse when scaled with a Reynolds number based on the aspect ratio of the vortices. Finally, new large experimental apparatuses have been built (van Gils *et al.* 2011; Avila & Hof 2013; Merbold *et al.* 2013), and these effects will be further detailed in ranges of higher Re if future investigations attempt to count the number of vortices.

Acknowledgements

We are grateful to Florent Ravelet for providing the data from Ravelet *et al.* (2010) and Sebastian Merbold for discussions on the calculation of the exponents. The authors also acknowledge the financial support of the Région Haute Normandie and the Agence Nationale de la Recherche (ANR), through the programme 'Investissement d'Avenir' (ANR-10-LABX-09-01), LabEx EMC3.

REFERENCES

ABSHAGEN, J., LOPEZ, J. M., MARQUES, F. & PFISHER, G. 2005 Mode competition of rotating waves in reflection-symmetric Taylor–Couette flow. *J. Fluid Mech.* **540**, 269–299.

AVILA, K. & HOF, B. 2013 High-precision Taylor–Couette experiment to study subcritical transitions and the role of boundary conditions and size effects. *Rev. Sci. Instrum.* **84**, 065106.

BARCILON, A., BRINDLEY, J., LESSEN, M. & MOBBS, F. R. 1979 Marginal instability in Taylor–Couette flows at a very high Taylor number. *J. Fluid Mech.* **94**, 453–463.

BATTEN, W. M. J., BRESSLOFF, N. W. & TURNOCK, S. R. 2002 Transition from vortex to wall driven turbulence production in the Taylor–Couette system with a rotating inner cylinder. *Intl J. Numer. Meth. Fluids* **38** (3), 207–226.

BENJAMIN, T. B. & MULLIN, T. 1982 Notes on the multiplicity of flows in the Taylor experiment. *J. Fluid Mech.* **121**, 219–230.

BILSON, M. & BREMHORST, K. 2007 Direct numerical simulation of turbulent Taylor–Couette flow. *J. Fluid Mech.* **579**, 227–270.

BRAUCKMANN, H. J. & ECKHARDT, B. 2013 Direct numerical simulation of local and global torque in Taylor–Couette flow up to $Re = 30\,000$. *J. Fluid Mech.* **718**, 398–427.

BURIN, M. J., SCHARTMAN, E. & JI, H. 2010 Local measurements of turbulent angular momentum transport in circular Couette flow. *Exp. Fluids* **48**, 763–769.

CLIFFE, K. A., KOBINE, J. J. & MULLIN, T. 1992 The role of anomalous modes in Taylor–Couette flow. *Proc. R. Soc. Lond.* A **439**, 341–357.

COLES, D. 1965 Transition in circular Couette flow. *J. Fluid Mech.* **21**, 385–425.

COUETTE, M. 1890 Etudes sur le frottement des liquides. *Ann. Chim. Phys.* **6**, 433–510.

COUGHLIN, K. & MARCUS, P. S. 1996 Turbulent bursts in Couette–Taylor flow. *Phys. Rev. Lett.* **77**, 2214–2217.

CZARNY, O., SERRE, E., BONTOUX, P. & LUEPTOW, R. M. 2003 Interaction between Ekman pumping and centrifugal instability in Taylor–Couette flow. *Phys. Fluids* **15**, 467–477.

DI PRIMA, R. C. & SWINNEY, H. L. 1981 Instabilities and transition in flow between concentric rotating cylinders. In *Hydrodynamics Instabilities and the Transition to Turbulence*, Topics in Applied Physics, vol. 45, pp. 139–180. Springer.

DOERING, C. R. & CONSTANTIN, P. 1992 Energy equation in shear driven turbulence. *Phys. Rev. Lett.* **69**, 1648–1651.

DONNELLY, R. J. & SIMON, N. J. 1960 An empirical torque relation for supercritical flow between rotating cylinders. *J. Fluid Mech.* **7**, 401–418.

DUBRULLE, B., DAUCHOT, O., DAVIAUD, F., LONGARETTI, P.-Y., RICHARD, D. & ZAHN, J.-P. 2005 Stability and turbulent transport in Taylor–Couette flow from analysis of experimental data. *Phys. Fluids* **17**, 95103.

DUTCHER, C. S. & MULLER, S. 2009 Spatio-temporal mode dynamics and higher order transitions in high aspect ratio Newtonian Taylor–Couette flows. *J. Fluid Mech.* **641**, 85–113.

ECKHARDT, B., GROSSMANN, S. & LOHSE, D. 2007 Torque scaling in turbulent Taylor–Couette flow between independently rotating cylinders. *J. Fluid Mech.* **581**, 221–250.

ESSER, A. & GROSSMANN, S. 1996 Analytic expression for Taylor–Couette stability boundary. *Phys. Fluids* **8**, 1814–1819.

VAN GILS, D. P. M., HUISMAN, S. G., BRUGGERT, G.-W., SUN, C. & LOHSE, D. 2011 Torque scaling in turbulent Taylor–Couette flow with co- and counterrotating cylinders. *Phys. Rev. Lett.* **106**, 24502.

GOLLUB, J. P. & SWINNEY, H. L. 1975 Onset of turbulence in a rotating fluid. *Phys. Rev. Lett.* **35** (14), 927–930.

HUISMAN, S. G., VAN GILS, D. P. M., GROSSMANN, S., SUN, C. & LOHSE, D. 2012 Ultimate turbulent Taylor–Couette flow. *Phys. Rev. Lett.* **108**, 24501.

KOSCHMIEDER, E. L. 1979 Turbulent Taylor vortex flow. *J. Fluid Mech.* **93**, 515–527.

LATHROP, D. P., FINEBERG, J. & SWINNEY, H. L. 1992 Transition to shear-driven turbulence in Couette–Taylor flow. *Phys. Rev.* A **46**, 6390–6405.

LEWIS, G. S. & SWINNEY, H. L. 1999 Velocity structure functions, scaling and transitions in high-Reynolds-number Couette–Taylor flow. *Phys. Rev.* E **59**, 5457–5467.

LIM, T. T. & TAN, K. S. 2004 A note on power-law scaling in a Taylor–Couette flow. *Phys. Fluids* **16**, 140–144.

MALLOCK, A. 1888 Determination of the viscosity of water. *Proc. R. Soc. Lond.* **45**, 126–132.

MERBOLD, S., BRAUCKMANN, H. J. & EGBERS, C. 2013 Torque measurements and numerical determination in differentially rotating wide gap Taylor–Couette flow. *Phys. Rev.* E **87**, 23014.

MULLIN, T. & BENJAMIN, T. B. 1980 Transition to oscillatory motion in the Taylor experiment. *Nature* **288**, 567–659.

NAKABAYASHI, K., YAMADA, Y. & KISHIMOTO, T. 1982 Viscous frictional torque in the flow between two concentric rough cylinders. *J. Fluid Mech.* **119**, 409–422.

OSTILLA, R., STEVENS, R. J. A. M., GROSSMANN, S., VERZICCO, R. & LOHSE, D. 2013 Optimal Taylor–Couette flow: direct numerical simulation. *J. Fluid Mech.* **719**, 14–46.

OSTILLA-MÓNICO, R., VAN DER POEL, E. P., VERZICCO, R., GROSSMANN, S. & LOHSE, D. 2014 Boundary layer dynamics at the transition between the classical and the ultimate regime of Taylor–Couette flow. *Phys. Fluids* **26**, 015114.

PAOLETTI, M. S. & LATHROP, D. P. 2011 Angular momentum transport in turbulent flow between independently rotating cylinders. *Phys. Rev. Lett.* **106**, 24501.

PIRRÓ, D. & QUADRIO, M. 2008 Direct numerical simulation of turbulent Taylor–Couette flow. *Eur. J. Mech. (*B*/Fluids)* **27**, 552–566.

RACINA, A. & KIND, M. 2006 Specific power input and local micro mixing times in turbulent Taylor–Couette flow. *Exp. Fluids* **41**, 513–522.

RAVELET, F., DELFOS, R. & WESTERWEEL, J. 2010 Influence of global rotation and Reynolds number on the large-scale features of a Taylor–Couette flow. *Phys. Fluids* **22**, 55103.

RIECKE, H. & PAAP, H.-G. 1986 Stability and wavevector restriction of axisymmetric Taylor vortex flow. *Phys. Rev.* A **33** (1), 547.Au: If possible, please provide last page number for Riecke & Paap (1986).

SNYDER, H. A. 1969 Wavenumber selection at finite amplitude in rotating Couette flow. *J. Fluid Mech.* **35** (2), 273–298.

STUART, J. T. 1958 On the nonlinear mechanics of hydrodynamic stability. *J. Fluid Mech.* **4** (1), 1–21.

TAKEDA, Y. 1999 Quasi-periodic state and transition to turbulence in a rotating Couette system. *J. Fluid Mech.* **389**, 81–99.

TAYLOR, G. I. 1923 Stability of a viscous liquid contained between two rotating cylinders. *Phil. Trans. R. Soc. Lond.* A **223**, 289–343.

TAYLOR, G. I. 1936 Fluid fraction between rotating cylinders. I. Torque measurements. *Proc. R. Soc. Lond.* A **157**, 546–564.

TOKGOZ, S., ELSINGA, G. E., DELFOS, R. & WESTERWEEL, J. 2012 Spatial resolution and dissipation rate estimation in Taylor–Couette flow for tomographic PIV. *Exp. Fluids* **53**, 561–583.

WENDT, F. 1933 Turbulente Strömungen zwischen zwei rotierenden konaxialen Zylindern. *Ing.-Arch.* **4**, 577–595.

XIAO, Q., LIM, T. T. & CHEW, Y. T. 2002 Effect of acceleration on the wavy Taylor vortex flow. *Exp. Fluids* **32**, 639–644.

PHYSICAL REVIEW E **84**, 011302 (2011)

Packings of deformable spheres

Shomeek Mukhopadhyay[1,2] and Jorge Peixinho[2,3,*]
[1]*Chemistry Department, Columbia University, New York, New York 10027, USA*
[2]*Benjamin Levich Institute, City College of City University of New York, New York, New York 10031, USA*
[3]*Chemical Engineering Department, City College of City University of New York, New York, New York 10031, USA*
(Received 13 January 2011; revised manuscript received 17 June 2011; published 13 July 2011)

We present an experimental study of disordered packings of deformable spheres. Fluorescent hydrogel spheres immersed in water together with a tomography technique enabled the imaging of the three-dimensional arrangement. The mechanical behavior of single spheres subjected to compression is first examined. Then the properties of packings of a randomized collection of deformable spheres in a box with a moving lid are tested. The transition to a state where the packing withstands finite stresses before yielding is observed. Starting from random packed states, the power law dependence of the normal force versus packing fraction or strain at different velocities is quantified. Furthermore, a compression-decompression sequence at low velocities resulted in rearrangements of the spheres. At larger packing fractions, a saturation of the mean coordination number took place, indicating the deformation and faceting of the spheres.

DOI: 10.1103/PhysRevE.84.011302 PACS number(s): 45.70.−n, 64.60.Cn

I. INTRODUCTION

Granular materials have recently emerged as prototypes of the so called "jammed" state [1–3] of matter. The jammed state for a collection of spherical particles assumes that locally the particles are in mechanical equilibrium. However, global constraints may not be satisfied and small perturbations such as tapping may evolve the system toward a global minimum [4]. For a collection of rigid spheres, such a limit point is generally seen to be around 0.64 packing fraction and is known as the random close packing. The physics of jammed hard spheres is developing and it is the purpose of this article to study experimentally a new system of three-dimensional packings of deformable spheres in this context by measuring quantitatively normal forces and contact number distributions.

In two dimensions, experiments on jamming transition using a collection of photoelastic disks [3] showed power law scalings in pressure and contact number distributions as the density of the system increased. There has been limited experimental studies in three dimensions on the properties and structure of dense granular packings [5–8]. Moreover, all experimental studies on three-dimensional systems have been limited to realizations of hard spheres systems. Three-dimensional systems of deformable particles are ubiquitous in everyday life, ranging from piles of fruits to arrangements of biological cells. Therefore, developing a simple imaging system with the capability of measuring particle positions, contact areas, coordination numbers, and deformations seems an unique tool to test recent theoretical and numerical results on the jamming of deformable particles [9,10]. Although it is possible to perform particle tracking in three dimensions using fluorescent dyes in immersed fluid [7,8,11], severe constraints on optical refractive index matching makes it difficult to resolve particle contacts, and modern investigations resort to x-ray tomography [12] for static studies, magnetic resonance imaging in dense hard-spheres systems [13], and confocal microscopy in colloidal suspensions.

Here we report an analysis of a new three-dimensional imaging technique of disordered packings of deformable particles under normal forces. To achieve this, we used fluorescent particles immersed in an index matched fluid and studied quantitatively the contact number distribution.

II. EXPERIMENTAL METHODS

The details of both the normal force and particle contacts as a function of volume fraction were studied using fluorescent polyacrylamide hydrogel spheres. Packings of about 600 deformable spheres of 16 ± 2 mm in diameter were considered. The polyacrylamide spheres were first grown in water-Rhodamine 6G solution (0.05 mg/ml). The polyacrylamide polymer comprised 10% of the final swelled sphere, so the hydrogel spheres were fluorescent and their refractive index was equal to that of water. Then the spheres were immersed in deionized water within an acrylic square box. The walls were flat and 127 mm on each side. The box was placed on the normal force transducer of a TA Instrument AR2000 rheometer. The lid of the box was connected to the head of the rheometer, which moved vertically at controlled speeds ranging from 0.1 to 1000 μm/s, while the normal force was measured simultaneously. There was a thin gap between the lid and the walls of the box, so that water could escape without disturbing the spheres. The accuracy of the normal force transducer was 0.01 N. For the low packing fractions ∼0.60–0.64, no force transmission was detected by the transducer, although the lid of box was observed to touch one or several spheres. In addition, a vertical green laser sheet was translated through the box in order to image slices through the packing. Photographs of 300 slices (3000 by 2000 pixels) through the packing were taken using a digital camera. (The imaging of the arrangement for $\phi = 0.64$ is available in the Supplemental Material [14].) Mean coordination numbers and centers of spheres were extracted from the photographs using an image analysis software.

*Present Address: Chimie-ParisTech, and CNRS UMR 7575, 11 rue Pierre et Marie Curie, F-75231 Paris Cedex 05, France.

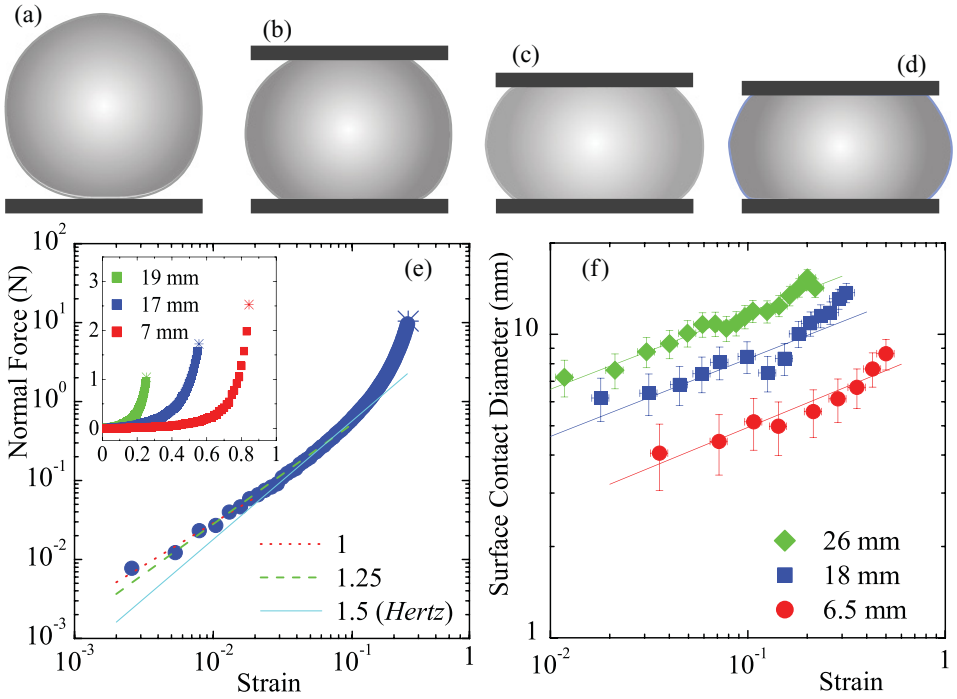

FIG. 1. (Color online) (a)–(d) A sequence of schematics of a 16-mm-diameter sphere compressed at strains of $\varepsilon = 0$, 0.2, 0.35, and 0.4. (e) Normal force, F_N, versus strain, ε, for a sphere of 17 mm diameter. The lines represent fits of $F_N \propto \varepsilon^{\alpha}$, where α is the exponent indicated in the legend. Inset: the normal force versus strain with a linear scale for three spheres of different diameters. The stars indicate the fracture of the sphere. (f) Surface contact diameter, a, as a function of strain, ε, for three spheres of different diameters. The lines also represent power law fits with exponents of 1/4.

At the scale of a single sphere, normal compression tests were performed using the rheometer and the results are shown on Fig. 1. The individual hydrogel spheres, which can range in diameter from 5 to 30 mm, are highly deformable [see Figs. 1(a)–1(e)]. Elastic spheres are usually dealt with using the approximation of linear equations of continuum elastic theory (Hooke's law) and small contact radius. The Young's Modulus of the hydrogel spheres is $O(10^4)$ Pa in agreement with previous studies [15]. The Hertz model predicts that the normal force and the strain of the sphere scale as $F_N \propto \varepsilon^{3/2}$; here $\varepsilon = (d_0 - d)/d_0$, where d_0 is the sphere diameter and d is the imposed height. Additionally, the contact region diameter, a, scales as $\varepsilon^{1/4}$. The properties of the deformable spheres were tested for a range of sphere diameters using different types of surfaces, under dry and immersed conditions, and at different compression velocities. The results are compared to models in Fig. 1(e). For ε from 0.002 to 0.02, F_N is proportional to ε. In a larger range of strains, from 0.002 to 0.2, $F_N \propto \varepsilon^{1.25}$. At large ε, such scaling deviates because of nonlinearities and extensions to the Hertz model need to be used in describing the materials [16]. The surface contact measurement, presented in Fig. 1(f), were obtained by shining a horizontal laser sheet on the horizontal plane between the top of the compressed sphere and the quartz plate. Digital photographs were taken through the plate and analyzed. The contact surface diameter evolved as $a \propto \varepsilon^{1/4}$.

In the present investigation, the packings was prepared as follows: the spheres were counted, measured, and gently poured into the water-filled box in order to avoid any trapped air bubble. Before each experimental run, the mixture was stirred with a rod for few seconds. After the decay of any motion, the top lid moved downward for the compression test. The packing fraction was controlled by the position of the lid with a maximum error of 0.02. Alternatively, an estimate of the packing strain is given by: $\varepsilon_p \simeq 1.18\phi - 0.75$. The polydispersity of the system prevented any large-scale crystallization in the system except near the walls of the box. At compression velocities of 100 μm/s or higher, large-scale rearrangements were seen as the packing fraction of the system increased. These correlated motions were reminiscent of slip-plane motion seen in granular materials [17]. However, at lower velocities, such large-scale rearrangements were not observed. The immersed hydrogel spheres form a system that has a small effective coefficient of friction. Measurements of the coefficient of friction for hydrogels on polystyrene surfaces gave values of $O(10^{-4})$ [18].

III. RESULTS AND DISCUSSION

The normal force was monitored as the packing fraction changed. Examples of regions from photographs halfway inside the packing are shown in Figs. 2(a)–2(c). For $\phi = 0.82$, significant deformation and large contact regions between spheres were observed. A three-dimensional reconstruction of a packing at $\phi = 0.62$ is also presented in Fig. 2(d). In Fig. 3, typical results for the normal force versus packing fraction

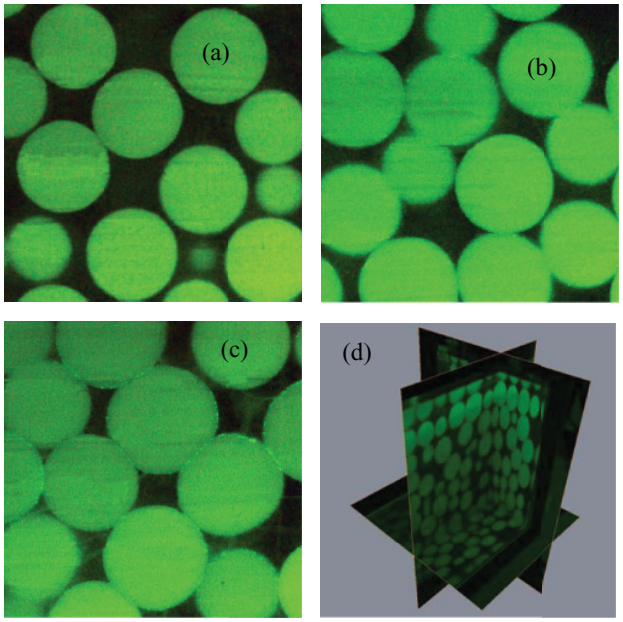

FIG. 2. (Color online) (a), (b), and (c) Region of interest of photographs of compressed packings of deformable spheres $\phi =$ 0.62, 0.72, and 0.82. (d) Three-dimensional reconstruction of a packing $\phi = 0.62$.

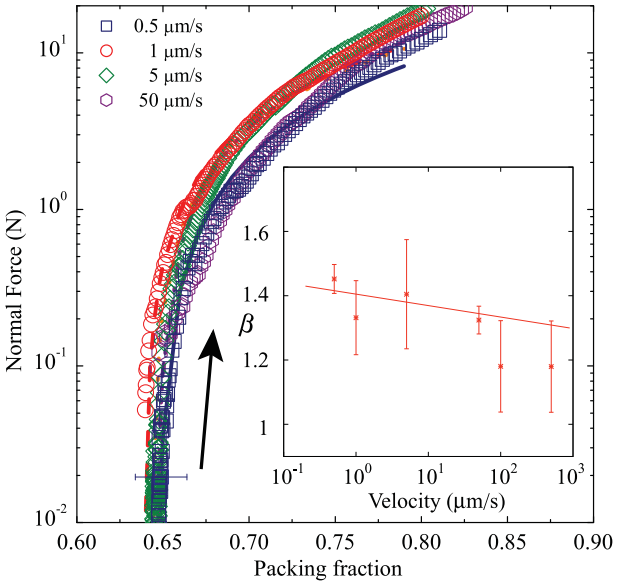

FIG. 3. (Color online) Compression of a packing of deformable spheres. Evolution of the normal force, F_N, versus the volume fraction, ϕ. Tests for different compression velocities. The lines represent fits of $F_N \propto (\phi - \phi_c)^\beta$. Inset: β versus compression velocity.

are shown for four different compression velocities, which were below the velocities at which large-scale rearrangements occurred. The lines behind the symbols represent power law fits: $F_N \propto (\phi - \phi_c)^\beta$. The exponent β decreases slightly with compression velocity. The inset of Fig. 3 presents the evolution of β for a range of compression velocities and the error bars describe the scatter of five to ten runs of the experiments. The scaling exponent, β, is larger than that observed in two dimensions [3]. The properties of our system are consistent with smaller packings used previously in swollen hydrogel systems [19]. Moreover, the exponent is in between that of hard sphere systems in three dimensions, which have finite friction $\beta \simeq 1.5$ [20,21] and that of emulsions $\beta \simeq 1.25$, which are usually modeled as frictionless spheres [22]. Since our spheres were Hertzian at relatively low strains, the power law exponent of ∼1.4 is expected if the system responds affinely to compression [9]. The normal force of the packing is determined by the deformability of the spheres rather than the mechanical contacts.

The scanning arrangement allowed the three-dimensional imaging of the packing; the analysis consisted of contact or coordination number as a function of packing fraction and is shown in Fig. 4(a). The error bars represent the measurement

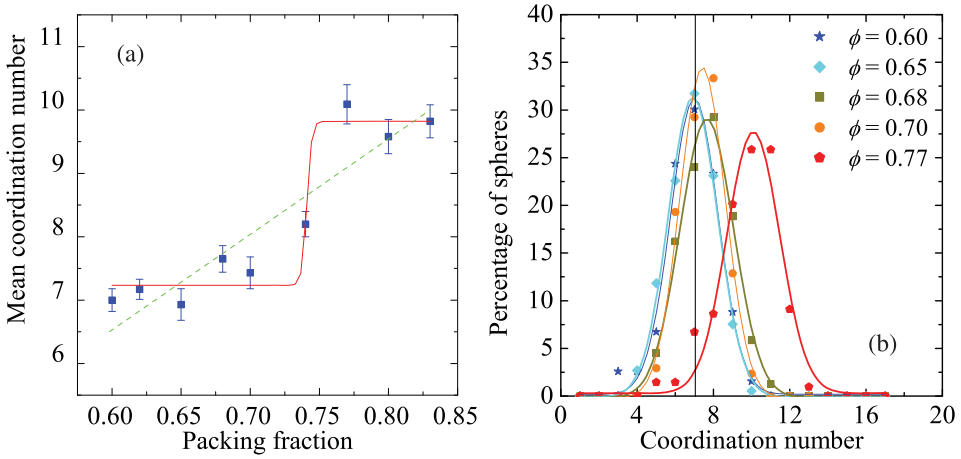

FIG. 4. (Color online) (a) Mean coordination number versus the packing fraction after compression. The dashed line represents the best linear fit. The continuous line represents a sigmoidal fit. (b) Probability distribution of the coordination number for packing fractions from $\phi = 0.60$ to 0.77. The vertical line represents a coordination number of seven.

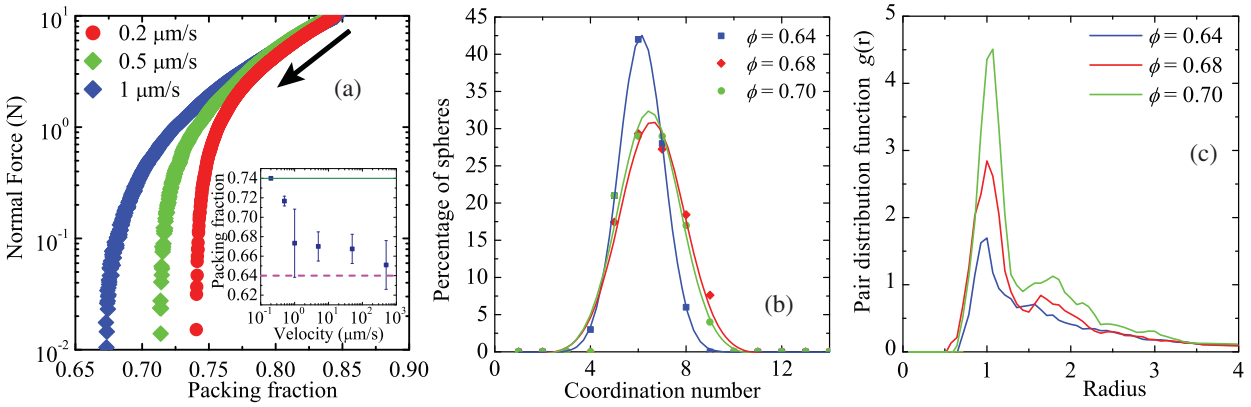

FIG. 5. (Color online) (a) Normal force in packings of deformable spheres at low velocities. Evolution of the normal, F_N, force versus the volume fraction, ϕ. Inset: the final packing fraction as a function of the compression-decompression velocity. (b) Probability distribution of the number of contacts for different packing fractions after decompression. (c) Pair distribution function $g(r)$.

error in coordination number. There is contact if the brightness remains constant as one moves radially from one sphere to the adjoining one. The analysis was carried out in the center of the packing without taking into account the three first layers near the walls. The influence of the boundary of the container has been studied by Lachhab and Weill [19] where they tested (i) the height of the packing and (ii) the effect of wall roughness by placing rigid spheres glued on the bottom of the box. They found that the fluctuations upon β are 4–7%, which is similar to the errors reported in the present experiments. At the lowest packing fraction ~0.60 that could be prepared the mean coordination number is slightly above seven and there is a slight increase as the packing fraction increases. The evolution of the coordination number seems linear although a significant jump in coordination number is seen around $\phi = 0.74$ and above $\phi = 0.80$, where it saturates to almost ten. The jump scenario is supported by a significant faceting of the spheres at packing fractions of 0.77 and higher. Local ordered structures are observed above $\phi = 0.74$, but there was no system spanning ordering of the spheres.

The distribution of coordination number can be well described by Gaussian fits as indicated in Fig. 4(b). There is a slight increase of the most probable coordination number as ϕ increases. The Gaussian distributions of the coordination number is consistent with numerical simulations of Hertz sphere systems [20,23] for ϕ below 0.74. Then the evolution of the mean coordination number can be described with a sigmoidal evolution [the continuous line in Fig. 4(a)]. This is a strong evidence that deformable spheres packings can differ significantly from the hard sphere results. Such type of behavior was observed in soft particle molecular dynamics simulations independently of the particle number [24]. It suggests that the deformation of the spheres causes the coordination number to saturate at high packing fractions. In the later stage of compression, sphere faceting is important to understand the force network through the packing.

IV. COMPRESSION-DECOMPRESSION EXPERIMENTS

All our experimental results on the compression of a disordered packings of deformable spheres led to measurable force transmission through the packing from around 0.64 packing fraction independently of the compression velocity. Until now, all the results were restricted to compression of random packings. Now, random packings experienced a compression followed by a decompression for a range of velocities. Surprisingly, the final packing fraction, after decompression from 0.85 packing fraction, reached 0.74 for the lowest velocity ($0.2\,\mu m/s$). Interestingly, slow decompression led to denser final packing as shown in Fig. 5(a). This is consistent with a recent numerical study of the jamming transition of frictionless spheres [25].

Starting with a packing around 0.64 and performing a compression-decompression test at low velocity, the final mean packing fraction decreased with the decompression velocity as indicated in the inset of Fig. 5(a). It appears that the slower the velocity was, the larger the final packing fraction. Similar packing rearrangements at low velocities after compression-decompression tests have been observed in other systems with ceramic material in a very viscous resin under cyclic heavy loading [26]. There are two velocity scales in the system: the settling velocity and the elastic velocity. The settling velocity of a sphere sets an upper velocity scale: $V_s \sim (\rho_s - \rho_f) g d_0^2/\mu$, where g is the gravity, ρ_s is the sphere density, ρ_f is the fluid density, and μ is the dynamic viscosity of water. The settling velocity was of the order of $10^4\,\mu m/s$ and corresponds to the velocity to form a loose packing of spheres under gravity. High-velocity compression-decompression tests experienced an asymptotic packing fraction of 0.64. The other velocity scale is based on the elasticity of the spheres. It is defined by $V_e^2 \sim G/\rho_s$, where G is the elastic modulus of the system in pascals. V_e was of the order of $10^{-5}\mu m/s$, so it is much smaller that any test experimentally achievable. However, at the smallest possible velocities the experimental packing fraction reached the value of $\phi = 0.74$, which indicates that slow velocities are necessary to reach a minimum energy state.

A natural question is whether a mean coordination number of six is observed in the packing of deformable spheres. Starting with a random packing and performing a compression-decompression test at low velocity, the final mean coordination number was six with a narrow width. The distribution remained Gaussian as presented in Fig. 5(b). The structures were more

ordered, but given the polydispersity, no complete crystallization of the system was observed. This strongly suggests that the mean coordination number is not a unique function of the packing fraction. Therefore, using the mean coordination number as a potential state variable in constructing theories should be treated with caution.

An indication of ordering of the deformable packing after a slow compression-decompression is given by the evolution of the pair distribution function $g(r)$, which describes how the sphere centers are distributed radially at the end of the experiments at slow velocity. In Fig. 5(c), the pair distribution function, $g(r)$, extracted from our image analysis has a single prominent peak. The peak with larger final packing fraction corresponds to the highest peak. Also, the second peak is higher for larger packing fraction in agreement with previous studies [20,27].

V. CONCLUSIONS

We have presented an experimental study of amorphous packings of deformable spheres. The mechanical behavior of deformable hydrogel spheres is quantified. At relatively high compression velocities, the system conserves many features of hard sphere packing. A typical power law behavior of the normal force evolution versus packing fraction is found in agreement with previous studies. However, the contact number has a different behavior than the hard sphere system. The novelty of the present system is that a three-dimensional imaging is possible: the mean coordination number and the pair distribution function evolution are quantified. Our system also opens a new way to look at internal dynamics of packings in which the interaction potential and packing fraction can be tuned separately by changing the "stiffness" of the hydrogel. At large packing fractions, the mean coordination number saturates, indicating the deformation and faceting of the spheres.

ACKNOWLEDGMENTS

The authors are grateful to Bulbul Chakraborty, Mark Shattuck, Jeff Morris, and Iker Zuriguel for discussions. S.M. thanks Matthias Sperl for hospitality at DLR, Cologne.

[1] C. S. O'Hern, L. E. Silbert, A. J. Liu, and S. R. Nagel, Phys. Rev. E **68**, 011306 (2003).
[2] A. J. Liu and S. R. Nagel, Nature (London) **396**, 21 (1998).
[3] T. S. Majmudar, M. Sperl, S. Luding, and R. P. Behringer, Phys. Rev. Lett. **98**, 058001 (2007).
[4] B. Chakraborty and R. P. Behringer, *Encyclopedia of Complexity and System Science*, edited by Robert A. Meyers (Springer-Verlag, New York, 2009).
[5] C. Song, P. Wang, and H. A. Makse, Proc. Natl. Acad. Sci. USA **102**, 2299 (2005); Nature (London) **453**, 629 (2008).
[6] T. Aste, Phys. Rev. Lett. **96**, 018002 (2006).
[7] S. Slotterback, M. Toiya, L. Goff, J. F. Douglas, and W. Losert, Phys. Rev. Lett. **101**, 258001 (2008).
[8] K. A. Lorincz and P. Schall, Soft Matter **6**, 3044 (2010).
[9] C. S. O'Hern, S. A. Langer, A. J. Liu, and S. R. Nagel, Phys. Rev. Lett. **88**, 075507 (2002).
[10] M. van Hecke, J. Phys. Condens. Matter **22**, 033101 (2010).
[11] A. V. Orpe and A. Kudrolli, Phys. Rev. Lett. **98**, 238001 (2007).
[12] M. Tsukahara, S. Mitrovic, V. Gajdosik, G. Margaritondo, L. Pournin, M. Ramaioli, D. Sage, Y. Hwu, M. Unser, and T. M. Liebling, Phys. Rev. E **77**, 061306 (2008).
[13] E. Fukushima, Annu. Rev. Fluid Mech. **31**, 95 (1999).
[14] See Supplemental Material at http://link.aps.org/supplemental/10.1103/PhysRevE.84.011302 for an imaging through the packing.
[15] K. N. Nordstrom, E. Vermeuil, W. G. Ellenbroek, T. C. Lubensky, J. P. Gollub, and D. J. Durian, Phys. Rev. E **82**, 041403 (2010).
[16] Y. Tatara, S. Shima, and J. C. Lucero, J. Eng. Mater. Tech.**113**, 287 (1991); K. K. Liu, D. R. Willimas, and B. J. Briscoe, J. Phys. D **31**, 294 (1998); E. C. Muniz and G. Geuskens, Macromolecules **34**, 4480 (2001); Y.-L. Lin, D.-M. Wang, W.-M. Lu, Y.-S. Lin, and K.-L. Tung, Chem. Eng. Sci. **63**, 195 (2008).
[17] P. Yu and R. P. Behringer, Chaos **15**, 041102 (2005).
[18] J. P. Gong, T. Kurokawa, T. Narita, G. Kagata, Y. Osada, G. Nishimura, and M. Kinjo, J. Am. Chem. Soc. **123**, 5582 (2001).
[19] T. Lachhab and C. Weill, Eur. Phys. J. B **9**, 59 (1999).
[20] H. P. Zhang and H. A. Makse, Phys. Rev. E **72**, 011301 (2005).
[21] H. A. Makse, D. L. Johnson, and L. M. Schwartz, Phys. Rev. Lett. **84**, 4160 (2000).
[22] M.-D. Lacasse, G. S. Grest, and D. Levine, Phys. Rev. E **54**, 5436 (1996).
[23] Y. Jin and H. A. Makse, Physica A **389**, 5362 (2010).
[24] R. Arevalo, I. Zuriguel, and D. Maza, Int. J. Bif. Chaos **19**, 695 (2009); Phys. Rev. E **81**, 041302 (2010).
[25] P. Chaudhuri, L. Berthier, and S. Sastry, Phys. Rev. Lett. **104**, 165701 (2010).
[26] X. Ye, T. Ganley, J. F. Morris, N. Tonmukayakul, and M. A. Parker, J. Petrol. Sci. Eng. **65**, 193 (2009).
[27] A. Donev, S. Torquato, and F. H. Stillinger, Phys. Rev. E **71**, 011105 (2005).

Résumé Les travaux de recherche présentés ici portent sur (i) la transition à la turbulence dans des conduites circulaires, (ii) des écoulements tournants turbulents et (iii) les fluides complexes. Les résultats sont principalement expérimentaux et parfois numériques. Le premier axe de recherche concerne la transition à la turbulence et les propriétés des écoulements faiblement turbulents dans des tubes droits ou avec élargissement. On s'intéresse, en particulier, aux propriétés des taches de turbulence localisées qui apparaissent lors de la transition. Le second axe de recherche concerne le couple exercé par les tourbillons dans des écoulements de Taylor-Couette turbulents, c'est à dire dans l'espace annulaire entre deux cylindres concentriques, avec le cylindre intérieur en rotation rapide. En particulier, est mis en évidence l'effet du contrôle de la longueur d'onde des tourbillons de Taylor sur les lois d'échelles prédisant la variation du couple en fonction de la vitesse. L'effet de l'ajout de polymères dans le liquide sur la mesure de couple est également quantifié. Ces études avec des solutions de polymères sont l'occasion d'étudier d'autres systèmes complexes comme des gels de polymères hydrophiles et super-absorbants. Une instabilité de type élastique qui apparaît lors du gonflement de ces matériaux est décrite et analysée. Enfin, des perspectives des différents axes sont présentées et discutées.

Mots clés Transition laminaire-turbulent, écoulement de Poiseuille, écoulement de Taylor-Couette, couple, liquides viscoélastiques, gels, instabilité élastique

Abstract The research presented here deals with (i) the transition to turbulence in circular pipes, (ii) turbulent rotating flows and (iii) complex fluids. The results are mainly experimental and sometimes numerical. The first line of research concerns the transition to turbulence and the properties of weakly turbulent flows in straight pipes or pipes with an expansion. Specifically, we investigate the properties of localised turbulent patches. The second line of research concerns the torque exerted by vortices in turbulent Taylor-Couette flow, which is the flow in the annular space between two concentric cylinders, when the inner cylinder is rotating. Interestingly, the effect of controlling the axial wavelength of turbulent Taylor vortices has an influence on the scaling laws for torque as a function of velocity. The effect of addition of polymer to the liquid on the torque measurements is also quantified. These studies with polymer solutions gave us the opportunity to study other complex fluids such as hydrophilic and super-absorbent polymer gels. An elastic instability that appears during the swelling of these materials is also described. Finally, prospects on the different lines of research are presented and discussed.

Key words Laminar-turbulent transition, pipe flow, Poiseuille flow, Taylor-Couette flow, viscoelastic liquids, gels, elastic instabilities